UNIVERSIDADE
BEIRA INTERIOR

Combustion Characteristics of Oxygen-Hydrogen Mixtures

(Versão corrigida após-defesa)

Diogo Soares Domingos

Dissertação para obtenção do Grau de Mestre em
Engenharia Aeronáutica
(mestrado integrado)

Orientadores: Professor Doutor André Resende Rodrigues da Silva
Professor Doutor Leandro Barbosa Magalhães

janeiro de 2026

Declaração de Integridade

Eu, Diogo Soares Domingos, que abaixo assino, estudante com o número de inscrição a41843 de/o Mestrado Integrado em Engenharia Aeronáutica da Faculdade de Engenharia, declaro ter desenvolvido o presente trabalho e elaborado o presente texto em total consonância com o **Código de Integridades da Universidade da Beira Interior**.

Mais concretamente afirmo não ter incorrido em qualquer das variedades de Fraude Académica, e que aqui declaro conhecer, que em particular atendi à exigida referenciação de frases, extratos, imagens e outras formas de trabalho intelectual, e assumindo assim na íntegra as responsabilidades da autoria.

Universidade da Beira Interior, Covilhã 07/01/2026

Assinado por: **Diogo Soares Domingos**
Num. de Identificação: 14239339
Data: 2026.01.06 19:27:29+00'00'

(assinatura conforme Cartão de Cidadão)

Dedication

A ti Pai.

One of my biggest supporters and closest friends, your strength and love have helped shape who I am today. I'll always be grateful for the care and warmth you gave me.

Even though you're no longer here to see this work come to life, I know you never doubted I'd get here. Wherever you are, I hope I've made you proud. I will always love you and carry with me the joy you brought into my life.

Acknowledgements

First and foremost, I would like to thank my advisors, Professor André Silva and Professor Leandro Barbosa, for their guidance and coordination of my work. I appreciate all the patience and guidance throughout the work.

I would like to extend my heartfelt thanks to all my friends from Desertuna, AEROUBI and AS Covilhã. From the very beginning of this journey, you welcomed me with warmth and enthusiasm. It's often said that university life is about more than just academics — and that could not be truer. You have transformed my experience, filling it with unforgettable moments and lifelong friendships. You have each played a part in shaping the person I am today, and for that, I will always be deeply grateful.

To my friends, thank you for accompanying me on this journey.

Lastly, and more importantly, a profound thanks to all my family, especially my parents, for all the sacrifices they have made over the years so that I could pursue my studies. Their wisdom and encouragement have been the greatest source of motivation I could have asked for. A special thanks to my sister, one of my best friends, and someone I will always cherish.

Resumo

A procura de sistemas de propulsão mais eficientes tem levado o setor aeroespacial a desenvolver câmaras de combustão capazes de operar sob condições extremas de pressão e temperatura (até 20 MPa e 3300 K). No entanto, a otimização destes sistemas através de abordagens experimentais baseadas em métodos iterativos é morosa e dispendiosa. Em resposta a este desafio, e apoiada pela crescente disponibilidade de recursos computacionais, tem-se verificado uma aposta significativa no desenvolvimento de ferramentas numéricas que permitam simular e analisar os processos de combustão em motores foguete de propelente líquido.

Esta dissertação contribui para esse esforço através do desenvolvimento de um modelo numérico de combustão robusto e fléxivel, capaz de analisar diferentes mecanismos cinéticos. O modelo utiliza formulações baseadas na equação de Arrhenius para o cálculo das constantes de reação e recorre às abordagens de Lindemann ou Troe para modelar reações dependentes da pressão, captando com precisão o comportamento na zona de transição (*fall-off*). Importa salientar que o modelo foi concebido para operar exclusivamente com combustão em fase gasosa, assumindo que todos os reagentes e produtos se encontram completamente vaporizados antes de participarem na reação. O método numérico baseia-se na biblioteca SUNDIALS, utilizando o integrador CVODE com o método *Backward Differentiation Formula*, adequado para sistemas rígidos. Esta abordagem exige a aplicação de métodos numéricos não lineares, neste caso o método de Newton, combinados com técnicas lineares, como o GMRES escalado e precondicionado. O modelo desenvolvido permite simulações em reatores de escoamento isobáricos e adiabáticos, possibilitando uma análise adimensional do comportamento da combustão. Dada a importância do hidrogénio no funcionamento de motores-foguete líquidos, este combustível é adoptado como foco principal ao longo da dissertação.

Devido à importância do hidrogénio na operação de foguetes de propelente líquido, este combustível é considerado ao longo de toda a dissertação. Para garantir a fiabilidade do modelo, este foi validado para um conjunto abrangente de dados experimentais, com especial atenção aos perfis de concentração de espécies, referente a misturas de hidrogénio e oxigénio. O conjunto de dados abrange uma ampla gama de condições, incluindo pressões entre 0.3 e 15.7 atm, temperaturas iniciais entre 880 e 943 K, e razões de equivalência iniciais entre 0.27 e 1.0.

Os resultados mostram que o modelo desenvolvido é capaz de descrever corretamente a evolução da concentração das espécies presentes no sistema, em conformidade com os dados experimentais utilizados para validação. Desta forma, o modelo estabelece uma base sólida para futuras extensões incluindo ambientes reativos que envolvam espécies mais complexas, como hidrocarbonetos. Ademais, o modelo pode ser melhorado com a inclusão de outros tipos de ambientes reativos, como o *jet stirred reactor*, chamas lam-

inares, regimes de combustão turbulenta e escoamentos reativos em alta pressão, típicos das câmaras de combustão de motores foguete de propelente líquido.

Palavras-chave

Modelação do processo de combustão, oxidação de hidrogénio, propulsão foguete, química cinética, simulação numérica

Abstract

The search for more efficient rocket propulsion systems has driven the aerospace engineering industry to innovate combustion chambers to withstand extreme conditions, including high pressure and temperature (up to 20 MPa and 3300 K). However, testing and optimising these systems through trial-and-error techniques is inefficient and costly. In response, and with the increased availability of computational resources, there has been a massive shift towards the development of numerical codes that facilitate the simulation and investigation of combustion events in liquid rocket engines.

This dissertation aims to contribute to that effort by developing a robust and flexible numerical combustion model that can analyse different kinetic mechanisms. The model employs an Arrhenius parametrisation to estimate reaction rates and Lindemann or Troe methods to represent fall-off behaviour in pressure-dependent reactions. Importantly, the model is formulated to operate exclusively with gaseous-phase combustion, assuming that all reactants and products are fully vaporised before participating in the reaction. The numerical solver draws upon the SUNDIALS suite in the form of the CVODE solver using the Backward Differentiation Formula method suitable for stiff problems. The use of this method requires a non-linear (Newton method) and a linear (scaled, preconditioned GMRES) methods to efficiently deal with the initial value problem. The model possesses the ability to simulate isobaric and adiabatic flow reactor configurations, which offer flexibility in dimensionless analysis of combustion performance. Given the central role of hydrogen in the operation of liquid rocket engines, this fuel is adopted as the primary focus throughout the dissertation.

Due to the importance of hydrogen in the operation of liquid rocket engines, this fuel is considered through the dissertation. To confirm its reliability, the model was compared with an extensive experimentally available dataset of species concentration profiles and ignition delay times, specially concerning hydrogen-oxygen mixtures. The validation set has a wide range of conditions with pressure ranging from 0.3 to 15.7 atm, initial temperature ranging from 880 to 935 K, and initial equivalence ratio ranging from 0.27 to 1.0.

The results show that the model can accurately predict the evolution of species concentrations over time, in agreement with the experimental data used for validation. Therefore, the model establishes a solid foundation for future developments, including reactive environments involving more complex species such as hydrocarbons. Additionally, the model can be further enhanced by incorporating turbulent combustion and high-pressure reactive flows, which are typical of combustion chambers in liquid rocket engines.

Keywords

Combustion modelling, hydrogen oxidation, rocket propulsion, chemical kinetics, numerical simulation

Contents

Dedication v

Acknowledgements vii

Resumo ix

Abstract xi

Contents xiii

List of Figures xvii

List of Tables xix

Acronyms and Abbreviations xxi

1 Introduction 1

1.1 Motivation 1

1.2 Objectives 3

1.3 Evaluating Propellants for Rocket Engines 4

1.4 Supercritical and Transcritical Regimes 8

1.5 Outline 11

2 Theoretical Review 13

2.1 Notations 13

2.2 Thermochemistry Fundaments 13

2.2.1 Thermodynamic Properties 13

2.2.2 Chemical Equilibrium 17

2.2.3 Equilibrium Reaction Rate 19

2.3 Modelling Strategies for Combustion Chemistry 21

2.4 Chemical Kinetics Parametrisation 22

2.4.1 Global and Elementary Reactions 22
2.4.2 Collision Theory 25
2.4.3 Rate Constants for Generic Kinetic Mechanisms 27
2.4.4 Pressure Dependence 29

3 State of the Art **35**

3.1 H_2-O_2 as a Reference Reaction 35
3.2 Detailed H_2-O_2 Kinetic Mechanism 35
3.2.1 Explosion limits in H_2-O_2 combustion 38
3.2.2 Reactions in H_2-O_2 Mechanisms 40
3.2.3 Consumption Path 44
3.2.4 Kinetic Models with Transport 45
3.3 Available Kinetic Mechanisms 46
3.3.1 Jachimowski Kinetic Mechanism 49
3.3.2 Yetter Kinetic Mechanism 49
3.3.3 Li Kinetic Mechanism 50
3.3.4 Ó Conaire Kinetic Mechanism 50
3.3.5 Davis Kinetic Mechanism 51
3.3.6 Konnov Kinetic Mechanism 51
3.3.7 Hong Kinetic Mechanism 52
3.3.8 Shimizu Kinetic Mechanism 53
3.3.9 Burke Kinetic Mechanism 54
3.3.10 Kéromnès Kinetic Mechanism 55
3.3.11 Varga Kinetic Mechanism 56
3.3.12 Hashemi Kinetic Mechanism 56
3.3.13 Alekseev Kinetic Mechanism 57
3.3.14 Z22 Kinetic Mechanism 57
3.3.15 Higher Hydrocarbon dedicated mechanisms 58
3.3.16 Model comparison 59

4 The numerical model **63**

4.1 Simulation Environment and Assumptions 63

4.2 Governing Equations 63

4.2.1 Species Mass Conservation 64

4.2.2 Energy Conservation 65

4.3 Problem Formulation 66

4.4 Ordinary Differential Equation Solver 68

4.4.1 Multi-step implicit methods 68

4.4.2 Available Solvers 70

4.4.3 Solvers Comparison 72

4.5 Model Implementation 73

4.5.1 Kinetic Pre-Processor 74

4.5.2 Solver 75

4.5.3 Graphical Post-Processor 76

4.6 Solver Settings 77

5 Results and Discussion **79**

5.1 Overview of simulation cases 79

5.2 Time shift 80

5.3 Influence of key initial conditions on system evolution 81

5.3.1 Explosion limits 82

5.3.2 Influence of pressure on the system evolution 84

5.3.3 Influence of initial equivalence ratio on the system evolution 86

5.3.4 Influence of initial temperature on the system evolution 89

6 Conclusions and Future Work **93**

6.1 Conclusions 93

6.2 Future work 94

A Chemical Kinetic Mechanisms **115**

A.1 Modified Jachimowski Hydrogen-Oxygen Kinetic Mechanism 115

A.2 Yetter Hydrogen-Oxygen Kinetic Mechanism 116
A.3 Li Hydrogen-Oxygen Kinetic Mechanism 117
A.4 Ó Conaire Hydrogen-Oxygen Kinetic Mechanism 118
A.5 Konnov Hydrogen-Oxygen Kinetic Mechanism 119
A.6 Hong Hydrogen-Oxygen Kinetic Mechanism 120
A.7 Shimizu Hydrogen-Oxygen Kinetic Mechanism 121
A.8 Burke Hydrogen-Oxygen Kinetic Mechanism 122
A.9 Kéromnès Hydrogen-Oxygen Kinetic Mechanism 123
A.10 Varga Hydrogen-Oxygen Kinetic Mechanism 124
A.11 Zettervall Hydrogen-Oxygen Kinetic Mechanism 125

List of Figures

1.1 Objects launched into space per year. 2

1.2 Ideal specific impulse of various propellants combinations. 9

1.3 Phase diagram of a single substance. 10

1.4 Critical point near region on a phase diagram. 11

3.1 Explosion limits of a stoichiometric H_2-O_2 mixture. 39

3.2 Main reactions as functions of the temperature regime for a mixture of $H_2/O_2/Ar$ = 0.7/1/3.76 tested with the Kéromnès et al. mechanism at 8 bar, 16 bar and 32 bar. 41

3.3 Sensitivity analysis of ignition time delays as a function of pressure at 1000 K for the Kéromnès et al. mechanism (mixture: $H_2/O_2/N_2/Ar$ = 1/1/1.88/1.88). 43

4.1 Program's Flowchart. 74

5.1 Reaction profiles for the H_2/O_2 reaction at 3.02 atm, T_{intial} = 934 K, and ϕ = 0.97. 82

5.2 Reaction profiles of the H_2/O_2 reaction at 0.3 atm, T_{intial} = 880 K and ϕ = 0.5. 83

5.3 Reaction profiles of the H_2/O_2 reaction at 1.0 atm, T_{intial} = 910 K and ϕ = 0.28. 83

5.4 Reaction profiles of the H_2/O_2 reaction at 2.55 atm, T_{intial} = 935 K and ϕ = 0.97. 85

5.5 Reaction profiles of the H_2/O_2 reaction at 3.44 atm, T_{intial} = 933 K and ϕ = 0.97. 85

5.6 Reaction profiles of the H_2/O_2 reaction at 6.0 atm, T_{intial} = 934 K and ϕ = 0.97. 86

5.7 Reaction profiles of the H_2/O_2 reaction at 0.6 atm and T_{intial} = 897 K for ϕ = 0.75 and ϕ = 0.55. 87

5.8 Reaction profiles of the H_2/O_2 reaction at 2.55 and 2.50 atm and T_{intial} = 940 K for ϕ = 1.0 and ϕ = 0.33. 87

5.9 Reaction profiles of the H_2/O_2 reaction at 15.70 atm and T_{intial} = 914 K for ϕ = 1.0 and ϕ = 0.27. 88

5.10 Reaction profiles of $H_2/O_2/N_2$ mixture at 6.5 atm, T_{intial} = 884 K and ϕ = 0.29. 90

5.11 Reaction profiles of $H_2/O_2/N_2$ mixture at 6.5 atm, T_{intial} = 889 K and ϕ = 0.29. 90

5.12 Reaction profiles of $H_2/O_2/N_2$ mixture at 6.5 atm, T_{intial} = 906 K and ϕ = 0.30. 91

5.13 Reaction profiles of $H_2/O_2/N_2$ mixture at 6.5 atm, T_{intial} = 914 K and ϕ = 0.30. 91

5.14 Reaction profiles of $H_2/O_2/N_2$ mixture at 6.5 atm, T_{intial} = 934 K and ϕ = 0.30. 92

List of Tables

1.1 Theoretical evaluation of liquid propellant performance in rocket combustion chambers. . . . 7

1.2 Theoretical evaluation of solid propellant performance in rocket combustion chambers. . . . 8

1.3 Critical properties of selected fluids. . . . 10

3.1 Hydrogen-Oxygen Kinetic Mechanisms. . . . 48

4.1 Absolute tolerance during simulations. . . . 77

5.1 Initial conditions for the experimental analysed data (x_{N_2}, from balance). . . 80

5.2 Maximum mole fraction of radicals in different conditions. . . . 88

5.3 Maximum mole fraction of radicals in different conditions using Mueller et al. mechanism. . . . 88

A.1 Modified Jachimowski Hydrogen-Oxygen Kinetic Mechanism. . . . 115

A.2 Yetter Hydrogen-Oxygen Kinetic Mechanism. . . . 116

A.3 Li Hydrogen-Oxygen Kinetic Mechanism. . . . 117

A.4 Ó Conaire Hydrogen-Oxygen Kinetic Mechanism. . . . 118

A.5 Konnov Hydrogen-Oxygen Kinetic Mechanism. . . . 119

A.6 Hong Hydrogen-Oxygen Kinetic Mechanism. . . . 120

A.7 Shimizu Hydrogen-Oxygen Kinetic Mechanism. . . . 121

A.8 Burke Hydrogen-Oxygen Kinetic Mechanism. . . . 122

A.9 Kéromnès Hydrogen-Oxygen Kinetic Mechanism. . . . 123

A.10 Varga Hydrogen-Oxygen Kinetic Mechanism. . . . 124

A.11 Zettervall Hydrogen-Oxygen Kinetic Mechanism. . . . 125

List of Symbols

Roman Symbols

A	-	Pre-exponential factor
	m^2	Control surface
c	$\mathrm{J\ kg^{-1}\ K^{-1}}$	Specific heat capacity
	$\mathrm{mol\ m^{-3}}$	Molar concentration
E_a	J	Activation energy
F	J	Helmholtz free energy
F_c	-	Centre-broadening parameter
G	J	Gibbs free energy
g	$\mathrm{J\ kg^{-1}}$	Specific Gibbs free energy
	$\mathrm{m\ s^{-2}}$	Gravitational acceleration
H	J	Enthalpy
h	$\mathrm{J\ kg^{-1}}$	Specific enthalpy
I	s	Impulse
J	-	Jacobian matrix
k	$(\mathrm{mol\ m^{-3}})^{1-(a+b+\ldots)}\ \mathrm{s^{-1}}$	Reaction rate constant
k_b	-	Reverse reaction rate constant
k_c	-	Equilibrium constant considering the species' molar concentrations
k_f	-	Forward reaction rate constant
k_p	-	Equilibrium constant
M	-	Third-body specie
m	kg	Mass
$\dot{m}$	$\mathrm{kg\ s^{-1}}$	Mass flow rate
N	-	Number of atoms
N_A	-	Avogadro number
n	mol	Amount of substance
p	Pa	Pressure
Q	J	Heat
q	-	Rate-of-progress variable
R	-	Reaction
$\mathcal{R}$	$\mathrm{J\ mol^{-1}\ K^{-1}}$	Universal gas constant
S	$\mathrm{J\ K^{-1}}$	Entropy
s	$\mathrm{J\ kg^{-1}\ K^{-1}}$	Specific entropy
T	K	Temperature
$\mathcal{T}$	N	Thrust
t	s	Time

U	J	Internal energy
u	J kg^{-1}	Specific internal energy
V	m^3	Volume
v	m^3 kg^{-1}	Specific volume
W	kg mol^{-1}	Molar mass
w	N	Weight
$\dot{w}$	N/s	Weight flow rate
X_s	-	Generic specie
x	-	Molar fraction
y	-	Mass fraction
Z	-	Collision frequency

Greek Symbols

β	-	Exponential factor
γ	-	Adiabatic index
Δ	-	Variation
ε	-	Catalytic efficiency
κ	J kg^{-1}	Boltzmann constant
λ	W m^{-1} K^{-1}	Thermal conductivity
ν	-	Stoichiometric coefficients
ρ	kg m^{-3}	Density
σ	m	Mean diameter
υ	m s^{-1}	Velocity
ϕ	-	Equivalence ratio
$\dot{\omega}$	mol m^{-3} s^{-1}	Production rate

Subscripts

cr	Critical point conditions
e	Nozzle exit conditions
f	Formation
mix	Mixture
p	Isobaric
prod	Products
R	Reaction
r	Reduced condition
reac	Reactants
ref	Reference
s	Sensible
sp	Specific

st	Stagnation
v	Isochoric
0	Standard
∞	Combustion chamber conditions

Superscripts

$prod$	Products
$reac$	Reactants
0	Standard-state
$\bar{}$	Molar property

Acronyms

AM	Adams-Moulton
BDF	Backward Differentiation Formula
DAE	Differential Algebraic Equations
GMRES	Generalised Minimal RESidual
IOM	Incomplete Orthogonalised Method
JANAF	Joint Army, Navy, Air Force
LLNL	Lawrence Livermore National Laboratory
LRE	Liquid Rocket Engine
LSODE	Livermore Solver for Ordinary Differential Equations
LU	Lower-Upper
MMH	MonoMethylHydrazine
NASA	National Aeronautics and Space Administration
NTO	Dinitrogen tetroxide
ODE	Ordinary Differential Equation
PDE	Partial Differential Equation
RANS	Reynolds-Averaged Navier-Stokes
RCM	Rapid Compression Machines
RP	Refined Petroleum
SPGMR	Scaled Preconditioned Generalised Minimal Residual
SRI	Stanford Research Institute
SUNDIALS	SUite of Nonlinear and DIfferential/ALgebraic equation Solvers
UDMH	Unsymetrical DiMethil Hidrazine
USC	University of Southern California

Chapter 1

Introduction

This chapter introduces the general direction of the work. Section 1.1 presents the study motivation and Section 1.2 outlining its main objectives. Sections 1.3 and 1.4 provides a brief contextualisation of the research within the broader scientific world. Finally, in Section 1.5 the structure of the dissertation is described to support a better understanding of how the work is organised.

1.1 Motivation

In the modern era, satellites orbiting the Earth provide a wide range of services that have become essential to contemporary life. From global communications and navigation to weather forecasting and environmental monitoring, satellites are now an indispensable component of XXI century society [1].

Historically, the high cost of launching payloads into space has been a significant barrier to broader space exploration and commercial utilisation. However, this trend has shifted significantly over the past decade, driven by major advancements in commercial rocketry. These advancements include both technological improvements and the removal of institutional barriers. On the technological side, there has been a focus on optimising for minimal cost, increasing simplicity, and expanding design margins. Institutionally, the emergence of commercial space companies has intensified market competition, supported by smaller workforces and a greater emphasis on in-house development. These innovations have dramatically reduced launch costs by as much as a factor of 20 in some cases, making space more accessible than ever before [2]. As a result, the number of objects launched into orbit has surged in recent years. According to the United Nations Office for Outer Space Affairs, more than 2800 objects, including satellites, probes, landers, crewed spacecraft, and space station components, were launched into Earth orbit and beyond in 2024 alone [3], as illustrated in Figure 1.1.

Another key factor in reducing the cost of space launches has been the adoption of numerical tools in the development of new rocket technologies. Traditionally, understanding combustion processes in high-performance rocket engines relied on full-scale testing, engineering analysis, fundamental combustion theory, and iterative trial-and-error methods [5]. However, as budgets become tighter and development cycles shorter, these conventional approaches have proven inefficient for meeting the growing demands for performance and reliability in propulsion systems.

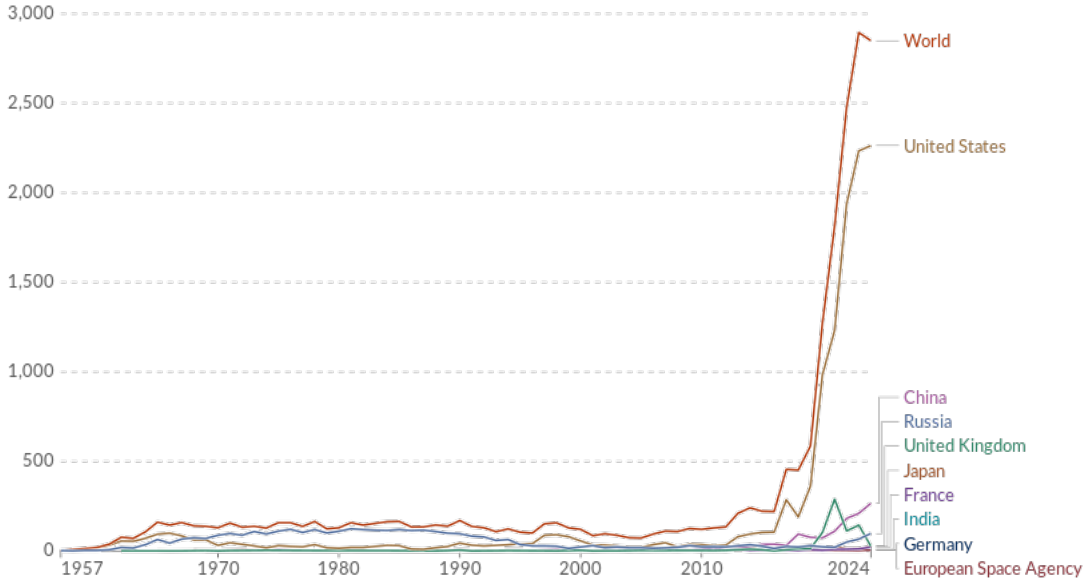

Figure 1.1: Objects launched into space per year [4].

In contrast, numerical simulations offer a faster and more cost-effective alternative by minimizing the need for extensive experimental setups. They also enable the analysis of complex geometries and detailed flowfield phenomena, such as flame-holding mechanisms [6], and allow for the investigation of physical behaviour within combustion chambers, where direct experimental access is often limited [7]. These capabilities have been made possible by advances in computational power, particularly improvements in processor speed and memory capacity, which have significantly expanded the detail of numerical simulations [8].

Nevertheless, complicated chemical and physical processes are involved in rocket engine combustion operating at high pressures [9]. As a result, it is not possible to perform numerical simulations of such flows without thoroughly validating the physical and chemical models. This is accomplished using comprehensive experimental studies of fundamental processes in well-regulated setups indicative of actual rocket engine operating settings [10].

Over the past two decades, the AEROG research team has been dedicated to identifying numerical methods capable of simulating intricate flow fields under the harsh conditions that exist in liquid rocket engine (LRE) operation. This work was initiated by Barata et al. [11], who investigated cryogenic nitrogen jets in subcritical and supercritical conditions and introduced a numerical method for simulating variable-density gaseous flows. From this basis, Antunes et al. [12,13] further advanced the computational approach by modifying the grid and boundary conditions to better simulate experimentally applicable conditions. Antunes et al.'s subsequent work [14, 15] incorporated real-fluid thermodynamics and heat transfer effects, continuing to introduce physical realism into simulations.

Recently, Magalhães et al. [16–18] compared various turbulence models at supercritical

conditions and prescribed suitable boundary conditions for the correct simulation of the injection process. Their recent publications [19, 20] applied RANS equations to examine the jet structure in various injector geometries. These papers also provided better insight into the "thermal breakup mechanism" exploring the feasibility of employing an incompressible, variable-density formulation for simulating supercritical fluid flows, in contrast to the commonly used compressible formulations.

Even with all of these significant advances, all prior developments were under cold-flow conditions. However, because LREs operate in reactive environments, there was a growing necessity to model combustion processes. Pedrosa [21] directly addressed this, implementing a chemical equilibrium model for implementation in the existing numerical approach. While this was a significant development, the model could not simulate detailed chemical kinetics that govern combustion in LRE chambers.

To address this gap, the present work concentrates on the implementation of a numerical framework for analysing chemical kinetic mechanisms, enabling the simulation of combustion processes within LRE combustion chambers. The ultimate aim is to integrate this framework into an existing numerical platform for supercritical flow analysis, thereby allowing the computation of reactive flow fields under realistic LRE operating conditions.

1.2 Objectives

The main objective of this work is to implement a numerical combustion model capable of simulating the chemical interactions between propellants in a LRE combustion chamber. This model is designed for integration into an in-house turbulent flow solver, allowing for the simulation of reactive supercritical fluids flows with enhanced physical fidelity.

The initial step in this work involved identifying the typical propellant combinations used in LREs and examining the fundamental chemical processes that govern their combustion. This included analysing the interactions between molecular species before, during, and after ignition. Such analysis enables the selection of the most appropriate chemical framework to accurately describe combustion phenomena within the LRE combustion chamber. Following this, the chosen chemical mechanism is parametrised, providing a structured approach to model and interpret the combustion behaviour under relevant operating conditions.

With the theoretical foundation established, the next phase focused on formulating the mathematical model and selecting appropriate numerical tools for implementation. Given the stiffness of chemical kinetics equations, the solver needed to ensure both accuracy and computational efficiency. After evaluating several options, the chosen solver was required to be robust, flexible, and well-established within the combustion modelling community.

To evaluate the performance of the developed model, it is necessary to assign appropriate values to its parameters and compare the resulting predictions with experimental data

available in the literature. Ideally, these parameter values should correspond to temperature and pressure conditions representative of those found in LRE combustion chambers, ensuring the model's relevance and accuracy under realistic operating scenarios.

1.3 Evaluating Propellants for Rocket Engines

Rocket propulsion systems can be categorised based on various factors such as energy source, basic function, vehicle type, size, propellant type, construction type, number of rocket propulsion units used in a given vehicle, and/or thrust production method [22]. There are several factors to consider when planning a rocket propulsion project. However, it's crucial to decide early on what kind of propulsion system will work best for the mission profile — chemical (solid or liquid propellants), electrical, or solar-thermal, or a combination of these [22].

The research and development of solar-thermal propulsion systems is ongoing to determine their readiness for use in real-world scenarios. Despite significant progress and successful ground testing, more work is required before transitioning to operational vehicles [23]. On the other hand, electrical propulsion systems are already used in specific space mission tasks, such as station-keeping, orbital adjustments, and even deep space missions. These propulsion systems are highly efficient in terms of specific impulse, allowing spacecraft to perform prolonged missions with less fuel compared to traditional chemical systems [24, 25]. However, chemical propulsion systems remain the superior choice for Earth launch missions due to their high thrust capabilities required for counteract Earth's gravitationally pull, whereas electric propulsion systems, despite high efficiency, lack the necessary thrust for initial launch phases [26].

Within chemical propulsion systems, three main subgroups can be defined: liquid, solid and hybrid propulsion, where the latter is a combination of the first two. Furthermore, liquid propulsion systems can be subdivided into monopropellant or bipropellant systems. A monopropellant propulsion system operates either as a cold gas thruster or through the catalytic decomposition of a single propellant, such as hydrazine (N_2H_4) or nitrous oxide (N_2O). These systems are typically employed in low-thrust satellite applications due to their simplicity and reliability. Differently, bipropellant systems use either Earth storable propellants (propellants that can be passively stored without the need for active cooling [27]), a mixture of storable and cryogenic propellants, or a fully cryogenic [28]. Bipropellants usually give a higher specific impulse than other chemical propulsion systems, namely cryogenic propellants [29].

The earliest known rockets, developed in XIV-century China, utilised solid propellants such as gunpowder [30]. Solid-fuel propulsion remained the dominant technology for several centuries. However, the advent of the XX century marked a pivotal shift with the development of liquid-fuel rockets, which significantly influenced the direction of propul-

sion research and technological advancement.

In solid propellant rockets, the fuel and the oxidiser are mixed in powder form and pressed into a solid grain. When fired, the combustion continues uncontrolled until all the propellant is consumed. Solid rockets are used primarily in military—tactical and ballistic missiles and also in space in the form of launch vehicle boosters and sounding rockets. In contrast to liquid propellants, they are used due to their simplicity, compactness, and ability to be kept for prolonged periods of time without the possibility of leaks or spills [22].

On the other hand, liquid propellant rockets provide independent storage of oxidiser and fuel in pressurised tanks and feed them into a combustion chamber, where they mix and burn. This is more manageable: combustion may be throttled, cut off, or resumed as needed. Additionally, they are capable of providing a higher efficiency, i.e. delivering greater thrust per unit weight of propellant burned (higher specific impulse), when compared to a solid fuel rocket fuel. Subsequently, they are preferred for medium- and large-scale space missions at the expense of other propulsion systems and upper stages [22]. However, this performance comes at the cost of increased system complexity, requiring pumps, valves, and additional structural mass.

As mentioned above, the specific impulse, I_{sp}, can be used to compare fuel performances. This parameter represents the thrust per unit propellant "weight" flow rate and a higher number often indicates better performance. It can be determined by Equation 1.1.

$$I_{sp} = \frac{\int_0^t \mathcal{T} dt}{g_0 \int_0^t \dot{m} dt} \quad (1.1)$$

In the equations, $\mathcal{T}$ represents the thrust force produced, t the time the propulsive system operates, g_0 the standard acceleration of gravity, and $\dot{m}$ the total propellant mass flow rate. For constant propellant mass flow $\dot{m}$, constant thrust $\mathcal{T}$, and negligible start or stop transients, it is possible to simplify Equation 1.1,

$$I_{sp} = \frac{\mathcal{T}}{\dot{m} g_0} = \frac{\mathcal{T}}{\dot{w}} \quad (1.2)$$

On the other hand, the thrust force can be described as a change in momentum. Considering the exit gas velocity, v_e is constant, uniform, and purely axial. When the mass flow rate is constant, thrust is itself constant, as shown in Equation 1.3.

$$\mathcal{T} = \frac{d(m v_e)}{dt} = \dot{m} v_e \text{ at sea level} = \frac{\dot{w}}{g_0} v_e \quad (1.3)$$

Replacing $\mathcal{T}$ in Equation 1.2 is possible to obtain Equation 1.4.

$$I_{sp} = \frac{v_e}{g_0} \quad (1.4)$$

Defining the stagnation enthalpy h_{st}, or total enthalpy, in a nozzle as

$$h_{st} = h + \frac{v^2}{2} = constant \quad (1.5)$$

For ideal gases, the enthalpy can be expressed as the product of the isobaric specific heat coefficient, c_p, and the absolute temperature T_0. Therefore Equation 1.5 can be redefined as,

$$h_{st} = c_p T_0 + \frac{v^2}{2} = constant \quad (1.6)$$

It is now possible to relate the flow in the combustion chamber to the flow at the exit of the nozzle. In the below equation, the subscript ∞ defines the flow in the combustion chamber, and the subscript e the flow at the nozzle exist.

$$c_{p,e} T_e + \frac{v_e^2}{2} = c_{p,\infty} T_\infty + \frac{v_\infty^2}{2} \quad (1.7)$$

Considering some important relations like the adiabatic index γ and Mayer's relation $c_p - c_v = \mathcal{R}$, it is possible to define the isobaric specific heat as $c_p = \frac{\mathcal{R}\gamma}{\gamma - 1}$. Rearranging Equation 1.7, considering isentropic (the isobaric specific heat remains unchanged) and steady flow is possible it is define I_{sp} as,

$$I_{sp} = \frac{1}{g_0} \sqrt{\frac{2\gamma \mathcal{R} T_\infty}{\gamma - 1} \left(1 - \left(\frac{p_e}{p_\infty} \right)^{\frac{\gamma - 1}{\gamma}} \right) + v_\infty^2} \quad (1.8)$$

Rearranging Equation 1.8 to include the molar mass of the exhaust gas W_e it is possible to write:

$$I_{sp} = \frac{1}{g_0} \sqrt{\frac{2\gamma T_\infty N_A \kappa}{(\gamma - 1) W_e} \left(1 - \left(\frac{p_e}{p_\infty} \right)^{\frac{\gamma - 1}{\gamma}} \right) + v_\infty^2} \quad (1.9)$$

Where κ is the Boltzmann constant and N_A is the Avogadro constant.

From Equation 1.9, a higher specific impulse is derived for higher combustion temperatures and exhaust particles with lower molar mass. Solid propellants tend to expel heavier combustion products, resulting in less specific impulse than liquid propellants. Liquid fuels produce lighter exhaust particles at usually higher combustion temperatures and, therefore, a higher specific impulse.

Sutton and Biblarz's thermochemical calculations complement this theoretical foundation [22], presented in Tables 1.1 and 1.2. These tables compare various propellant pairs. For liquid propellants, two assumptions about expansion are made: frozen, in which chemical

composition remains unchanged during nozzle expansion, and shifting, in which chemical processes still take place during expansion. These approximations introduce errors in performance estimation of about 1–4%.

Table 1.1: Theoretical evaluation of liquid propellant performance in rocket combustion chambers [a] [22].

Oxidiser	Fuel	Mixture Ratio		T_∞ [K]	I_{sp} [s]	
		By Mass	By Volume		Shifting	Frozen
Oxygen	Methane	3.20	1.19	3526		296
		3.00	1.11		311	
	Hydrazine	0.74	0.66	3285		301
		0.90	0.80	3404	313	
	Hydrogen	3.40	0.21	2959		386
		4.02	0.25	2999	389.5	
	RP - 1	2.24	1.59	3571	300	285.4
Fluorine	UDMH	1.39	0.96	3542		295
		1.65	1.14	3594	310	
	Hydrazine	1.83	1.22	4553	334	
		2.30	1.54	4713		365
	Hydrogen	4.54	0.21	3080		389
		7.60	0.35	3900	410	
Nitrogen tetroxide	Hydrazine	1.08	0.75	3258		283
		1.34	0.93	3152	292	
	50% UDMH 50% hydrazine	1.62	1.01	322		278
		2.00	1.24	3372	289	
	RP - 1	3.40	1.05	3290		297
Red fuming nitric acid	MMH	2.15	1.30	3396	289	
		1.65	1.00	3200		278
	RP - 1	4.10	2.12	3175		258
		4.80	2.48	3230	269	
	50% UDMH 50% hydrazine	1.73	1.00	2997		272
		2.20	1.26	3172	279	
Hydrogen Peroxide (90%)	RP - 1	7.0	4.01	2760		297

[a] The calculations considering a combustion chamber pressure of 6.895 MPa and a nozzle exit pressure of 0.101 MPa, adiabatic combustion and isentropic expansion of ideal gases. The mixture ratios are optimum and their performance is maximum.

When selecting liquid propellants, several key factors must be considered, including cost, environmental impact, and the need to protect personnel from the hazards associated with highly toxic substances such as hydrazine (N_2H_4), monomethylhydrazine (MMH), unsymmetrical dimethylhydrazine (UDMH), and nitrogen tetroxide (N_2O_4) [31]. At the same time, achieving a high specific impulse remains a central goal in propellant selection.

By around 2005, high-performance storable bipropellants commonly included combinations of nitrogen tetroxide (NTO) with various hydrazines (N_2H_4, MMH, and UDMH). As shown in Table 1.1, these combinations do indeed deliver high specific impulse values. However, their extreme toxicity, carcinogenicity, and explosive nature result in significant health and safety costs, make them inappropriate for low- and medium-thrust applications. To address these limitations, the search for non-toxic or "gree" propellants increased to lower operational risks and costs for smaller space vehicles. One such alternative was hydrogen peroxide (H_2O_2), which saw widespread use in the 1950s and 60s

Table 1.2: Theoretical evaluation of solid propellant performance in rocket combustion chambers [a] [22].

Oxidiser	Fuel	T_∞ [K]	I_{sp} [s]
Ammonium nitrate	11% binder and 7% additives	1282	192
Ammonium perchlorate 78 - 66%	18% organic polymer binder and 4 - 20% aluminum	2816	262
Ammonium perchlorate 84 - 68%	12% polymer binder and 4 - 20% aluminum	3371	266

[a] The calculations considering a combustion chamber pressure of 6.895 MPa and a nozzle exit pressure of 0.101 MPa, adiabatic combustion and isentropic expansion of ideal gases. The mixture ratios are optimum and their performance is maximum.

as a monopropellant in thrusters and gas generators. Despite its relative safety, its lower specific impulse compared to NTO-hydrazine combinations led to its eventual decline in favour of higher-performing alternatives [31].

To further assess potential propellant combinations, Haidn [28] presents a comparative analysis of specific impulse values as a function of oxidiser-to-fuel mixture ratios (see Figure 1.2). The results demonstrate that the O_2/H_2 combination offers the highest performance. Hydrocarbon fuels, such as kerosene, follow closely, although specific impulse tends to decrease with increasing carbon content when oxygen is used as the oxidiser. Fuels containing oxygen atoms, such as methanol and ethanol, show comparable performance to hydrocarbons. For completeness, combinations involving hydrogen peroxide as the oxidiser are also included in the analysis.

Indeed, since the introduction of the RL-10, the first hydrogen-fueled engine developed by Pratt & Whitney Rocketdyne, the use of liquid hydrogen has gained popularity due to several key advantages. Most notably, when combined with liquid oxygen, it offers a high energy density and specific impulse, as confirmed by the trends shown in Figure 1.2. Additionally, hydrogen is abundant in nature and environmentally friendly, producing only water as a byproduct of combustion. These qualities make it an increasingly attractive option in modern propulsion systems.

Based on the analysis of various propellant combinations, it is evident that the hydrogen-oxygen pair stands out as one of the best-performing alternatives. This explains its widespread use in propulsion systems across different rocket engines, particularly in core, main, and upper stages. For this reason, and as further detailed in Section 3.1, the hydrogen-oxygen reaction has been selected for deeper investigation in this work.

1.4 Supercritical and Transcritical Regimes

As demonstrated above, cryogenic propellants are widely used in modern high-performance rocket engines, where they are typically injected at high pressures to enhance specific performance, which is one of the most critical design parameters. Under these extreme condi-

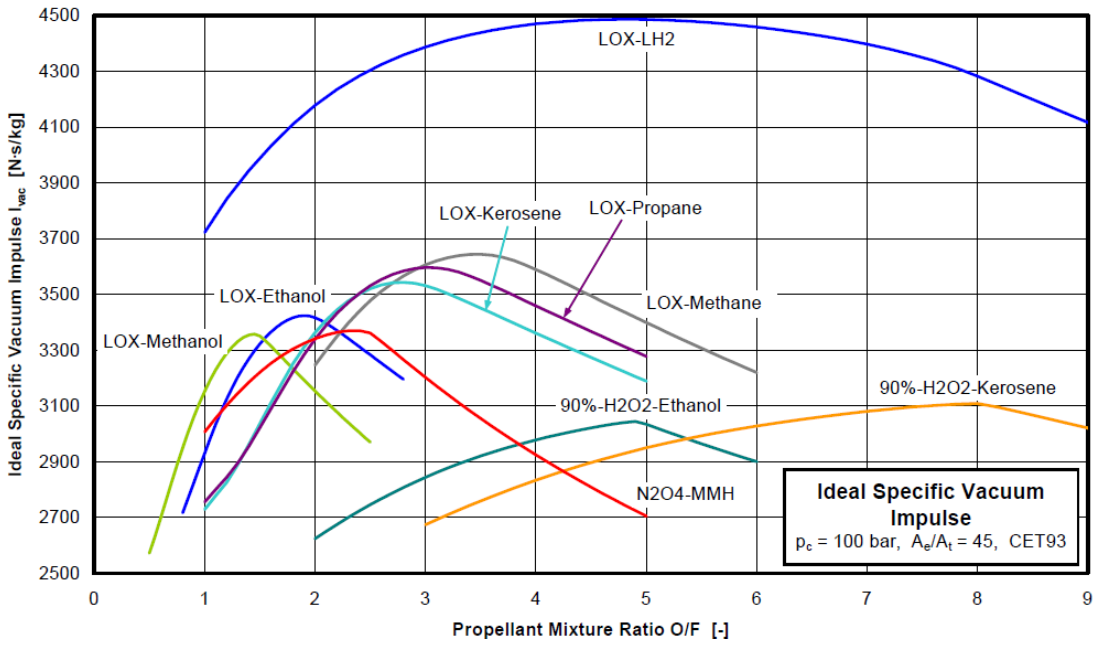

Figure 1.2: Ideal specific impulse of various propellants combinations [28].

tions, often transcritical or supercritical, the thermophysical properties of the propellants deviate significantly from those observed at atmospheric conditions. These changes affect not only the equation of state but also the transport properties and the flow behaviour within the combustion chamber [32].

Although the present work does not directly simulate transcritical or supercritical flows, it is important to contextualize the environment in which the developed combustion model will eventually be applied. The hydrogen-oxygen kinetic mechanisms studied here are intended for integration into a broader numerical framework capable of simulating reactive flow fields in liquid rocket engine (LRE) combustion chambers. Since these chambers often operate near or above the critical conditions of the propellants, a basic understanding of the associated thermodynamic regimes helps frame the relevance and applicability of the combustion modelling approach developed in this study.

The critical temperature can be easily identified in a phase diagram of a single substance, as shown in Figure 1.3.

In this schematic digram is possible to identify where the substance is in a single phase (areas with the phase name), the coexistence phase (solid-liquid and liquid-gas), defined by the lines that separate each phase, and the coexistence point, where the three phases coexist (triple point). Pressure will rise in tandem with temperature along the liquid-gas coexistence curve. Due to thermal expansion, the liquid gets less dense along this curve, and as pressure increases, the gas gets more dense. The curve ends at the critical point when the densities of the two phases eventually equalise and the difference between the gas and liquid vanishes [33]. As of right now, the substance is classified as a fluid, and its specific properties have a particular value for particular substances. As an example,

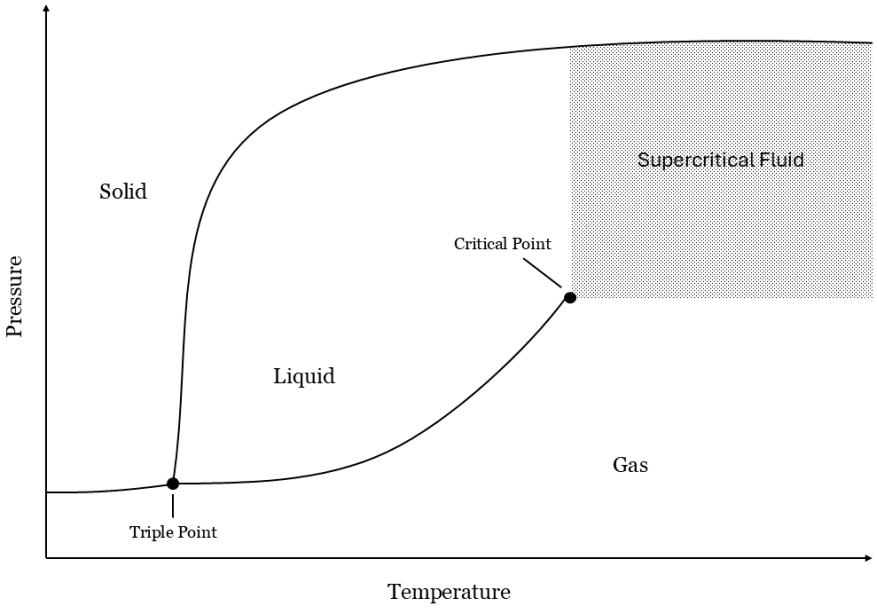

Figure 1.3: Phase diagram of a single substance.

the critical temperature, T_{cr}, and critical pressure, p_{cr}, for several substances are shown in Table 1.3.

Table 1.3: Critical properties of selected fluids [34].

Name	T_{cr} [K]	p_{cr} [MPa]	ρ_{cr} [kg/m^3]
Hydrogen, H_2	33.145	1.315	30.1205
Oxygen, O_2	154.60	5.043	436.1099
Methane, CH_4	190.56	4.5922	162.6545
Water, H_2O	647.10	22.064	312.9575
Carbon Dioxide, CO_2	304.13	7.3773	467.5082
Nitrogen, N_2	126.19	3.396	313.2832

It is possible to define the reduced temperature, T_r, and the reduced pressure, p_r, as the coefficient of the given temperature and pressure and the critical temperature and critical pressure, respectively, as defined in Equations 1.10 and 1.11. As a result, for any given temperature that is equal to the critical temperature, the reduced temperature is equal to 1, and the same holds true for pressure. A more thorough view of the area surrounding the critical point is shown in Figure 1.4.

$$T_r = \frac{T}{T_{cr}} \quad (1.10)$$

$$p_r = \frac{p}{p_{cr}} \quad (1.11)$$

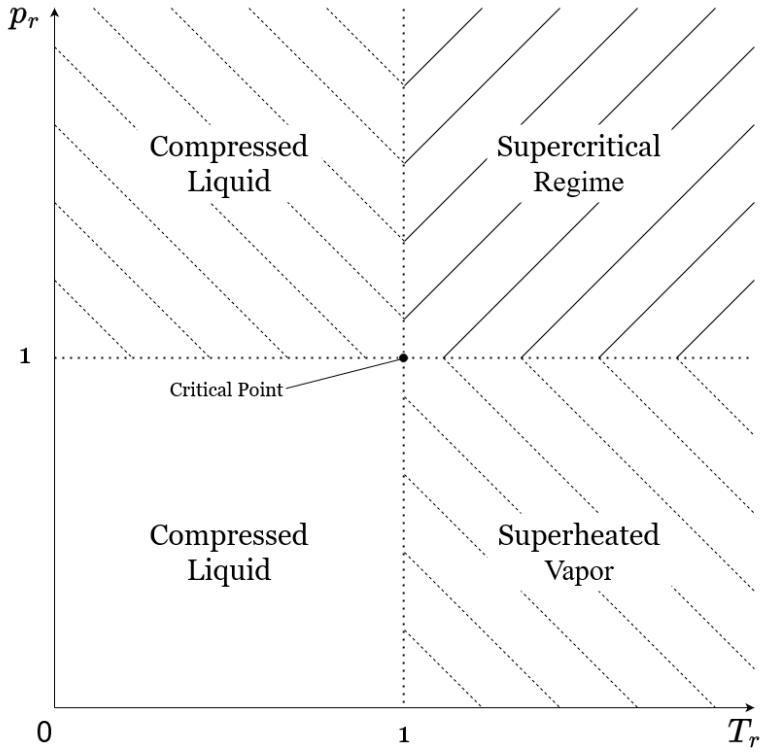

Figure 1.4: Critical point near region on a phase diagram [35].

With the observation of Figure 1.4 is clearly possible to identify four different regions:

1. **Subcritical Regime**: where the reduced temperature and reduced pressure are inferior to 1 ($T_r < 1, p_r < 1$);
2. **Superheated Vapor**: where the reduced temperature is greater than 1 ($T_r > 1$) and the reduced pressure inferior to 1 ($p_r < 1$);
3. **Compressed Liquid**: where the reduced temperature is inferior to 1 ($T_r < 1$) and the reduced pressure is greater than 1 ($p_r > 1$);
4. **Supercritical Regime**: where the reduced temperature and the reduced pressure are greater than 1 ($T_r > 1, p_r > 1$).

1.5 Outline

The remaining document is organised into five chapters. Chapter 2 reviews key thermochemical concepts essential to the development of the study, and evaluates different chemical modelling approaches, leading to the selection and parametrisation of the adopted method. Chapter 3 introduces and compares various kinetic mechanisms to jus-

tify the selection of the one used for model validation. Chapter 4 describes the construction of the numerical model and discusses the available numerical solvers, providing justification for the chosen solver. Chapter 5 presents the main validation results of the model, including a detailed comparison with experimental data. Finally, Chapter 6 summarises the main conclusions and offered reflections on the work developed, as well as suggestions for future research directions.

Chapter 2

Theoretical Review

This chapter introduces the thermochemical and kinetic foundations necessary for the development of the combustion model. Section 2.1 defines the notation adopted throughout this work. Section 2.2 presents the fundamental thermochemical principles relevant to combustion, starting with the thermodynamic properties required to describe the system's physical behaviour and concluding with the simplified case of chemical equilibrium. Section 2.3 reviews the most common chemical modelling approaches and provides a comparative analysis to justify the selection of the most suitable method for this study. Finally, Section 2.4 details the parametrisation of a generic kinetic mechanism and outlines its implementation within a numerical framework.

2.1 Notations

Throughout this chapter and the remainder of the document, specific notation is used to represent thermodynamic properties and kinetic variables. A key distinction is made between extensive and intensive properties. Extensive properties, which depend on the amount of substance, are denoted by capital letters—for example, volume (V). In contrast, intensive properties are independent of the substance quantity and are expressed per unit mass, using lowercase letters, such as specific enthalpy (h). An exception to this rule is temperature, an intensive property represented by a capital T.

Additionally, molar-based properties are indicated with an overbar (e.g., molar specific internal energy, $\bar{u}$), while a superscript zero denotes values at the standard reference state. Unless stated otherwise, this reference state corresponds to a temperature of 25 °C (298.15 K) and a pressure of 1 atm (101325 Pa).

2.2 Thermochemistry Fundaments

2.2.1 Thermodynamic Properties

The absorption or release of energy occurs in every chemical reaction and can be quantified through the variation in internal energy or enthalpy of the species involved. This energy change is determined by applying the principle of energy conservation, as stated in the First Law of Thermodynamics [36]. The expressions relating internal energy or

enthalpy with pressure and temperature are called caloric equations of state [9]:

$$u = u(T, v) \quad (2.1)$$

$$h = h(T, p) \quad (2.2)$$

A differential variation in internal energy or enthalpy can be obtained by differentiating Equations 2.1 and 2.2, respectively:

$$du = \left(\frac{\partial u}{\partial T}\right)_v dT + \left(\frac{\partial u}{\partial v}\right)_T dv \quad (2.3)$$

$$dh = \left(\frac{\partial h}{\partial T}\right)_p dT + \left(\frac{\partial h}{\partial p}\right)_T dp \quad (2.4)$$

In these expressions, the terms corresponding to the specific heats at constant volume (c_v) and constant pressure (c_p) appear. They are defined as:

$$c_v \equiv \left(\frac{\partial u}{\partial T}\right)_v \quad (2.5)$$

$$c_p \equiv \left(\frac{\partial h}{\partial T}\right)_p \quad (2.6)$$

For ideal gases, the partial derivatives concerning the specific volume and pressure are considered zero, and Equations 2.3 and 2.4 can be rewritten as:

$$u(T) - u(T_{ref}) = \int_{T_{ref}}^{T} c_v(T) dT \quad (2.7)$$

$$h(T) - h(T_{ref}) = \int_{T_{ref}}^{T} c_p(T) dT \quad (2.8)$$

Rearranging the above equations:

$$u(T) = u(T_{ref}) + \int_{T_{ref}}^{T} c_v(T) dT \quad (2.9)$$

$$h(T) = h(T_{ref}) + \int_{T_{ref}}^{T} c_p(T) dT \quad (2.10)$$

The above equations define the absolute specific internal energy and absolute specific enthalpy at a given temperature T. These quantities can be expressed as the sum of the specific internal energy of formation (u_f) or specific enthalpy of formation (h_f) at a reference state and the specific sensible internal energy (Δu_s) or specific sensible enthalpy (Δh_s) variation between the reference state and the given temperature. When the specific internal energy of formation or the specific enthalpy of formation is evaluated at the standard reference state, the equations can be rewritten as follows:

$$u(T) = u_f^0(T_{ref}) + \Delta u_s(T) \quad (2.11)$$

$$h(T) = h_f^0(T_{ref}) + \Delta h_s(T) \quad (2.12)$$

In a reactive mixture within an open system, assuming negligible changes in kinetic and potential energy as well as work being done only by pressure forces, the First Law of Thermodynamics states that the energy exchanged during a reaction corresponds to the change in the mixture's enthalpy. When both reactants and products are referenced to the same standard state, this energy change is referred to as the enthalpy of reaction. In combustion processes, it is specifically called the enthalpy of combustion, and it is defined as the difference between the absolute enthalpy of the products and that of the reactants:

$$\Delta H_R(T) = H_{prod}(T) - H_{reac}(T) \quad (2.13)$$

For a generic reaction where the reactants and products are at temperatures T_1 and T_2, respectively, the enthalpy variation can be determined using the following equation:

$$\begin{aligned} &H_{prod}\,(T_2) - H_{reac}\,(T_1) = \\ &= \sum_j^{(prod)} n_j \left(\bar{h}_{f,j}^0(T_{ref}) + \int_{T_{ref}}^{T_2} \bar{c}_{p,j}(T)dT \right) - \sum_i^{(reac)} n_i \left(\bar{h}_{f,i}^0(T_{ref}) + \int_{T_{ref}}^{T_1} \bar{c}_{p,i}(T)dT \right) \\ &= \Delta H_R^0(T_{ref}) + \sum_j^{(prod)} \int_{T_{ref}}^{T_2} c_{p,j}(T)dT + \sum_i^{(reac)} \int_{T_{ref}}^{T_1} c_{p,i}(T)dT \end{aligned} \quad (2.14)$$

Where:

$$\Delta H_R^0 = \sum_j^{(prod)} n_j \bar{h}_{f,j}^0(T_{ref}) - \sum_i^{(reac)} n_i \bar{h}_{f,i}^0(T_{ref}) \quad (2.15)$$

As seen before, the specific heat capacities are temperature-dependent. If considered exclusively temperature-dependent, the gas phase is called thermally "perfect", and the specific heat capacity can be calculated through a polynomial function that fits this behaviour. For example, the molar heat capacity at constant pressure can be expressed using a poly-

nomial of arbitrary order:

$$\frac{\bar{c}_p^0}{\mathcal{R}} = \sum_{n=1}^{N} a_n T^{(n-1)} \quad (2.16)$$

Where $\mathcal{R}$ is the universal gas constant, a are the coefficients of the polynomial that fit the specific heat capacity, and N is the total number of coefficients of the polynomial. The superscript ^{0} refers to the standard-state. For perfect gases, the heat capacity is independent of pressure, and the standard values become the actual value.

Considering Equations 2.12 and 2.16, it is now possible to define the specific enthalpy in polynomial form:

$$\frac{\bar{h}^0}{\mathcal{R}T} = \sum_{n=1}^{N} \frac{a_n T^{(n-1)}}{n} + \frac{a_{N+1}}{T} \quad (2.17)$$

Where $a_{N+1}\mathcal{R}$ is the standard heat of formation at standard reference temperature. Additionally, entropy can be calculated by the following equation:

$$\bar{s}^0 = \int_{T_{ref}}^{T} \frac{c_p^0}{T} dT + s^0(0) \quad (2.18)$$

In polynomial form:

$$\frac{\bar{s}^0}{\mathcal{R}} = a_1 \ln T + \sum_{n=2}^{N} \frac{a_n T^{(n-1)}}{(n-1)} + a_{N+2} \quad (2.19)$$

Where the integration constant $a_{N+2}\mathcal{R}$ is evaluated from knowledge of the standard-state entropy.

The previous equations describe a general form for an arbitrary-order polynomial. However, to apply these functions in practice, a specific polynomial order must be selected. In this work, the widely adopted 7-term NASA polynomials [37] are used, corresponding to a fifth-order polynomial (i.e., $N = 5$). Based on this formulation, the molar specific heat capacity at constant pressure, molar enthalpy, and molar entropy can be calculated using the following expressions:

$$\frac{\bar{c}_p^0}{\mathcal{R}} = a_1 + a_2 T + a_3 T^2 + a_4 T^3 + a_5 T^4 \quad (2.20)$$

$$\frac{\bar{h}^0}{\mathcal{R}T} = a_1 + \frac{a_2}{2} T + \frac{a_3}{3} T^2 + \frac{a_4}{4} T^3 + \frac{a_5}{5} T^4 + \frac{a_6}{T} \quad (2.21)$$

$$\frac{\bar{s}^0}{\mathcal{R}} = a_1 \ln T + a_2 T + \frac{a_3}{2} T^2 + \frac{a_4}{3} T^3 + \frac{a_5}{4} T^4 + a_7 \quad (2.22)$$

As it will be seen later in the chapter, it is useful to define the Gibbs free energy as a polynomial function. By definition, the Gibbs free energy is defined by:

$$G = H - TS \Leftrightarrow \frac{\bar{g}^0}{\mathcal{R}T} = \frac{\bar{h}^0}{\mathcal{R}T} - \frac{\bar{s}^0}{\mathcal{R}} \quad (2.23)$$

Replacing with Equations 2.21 and 2.22:

$$\frac{\bar{g}^0}{\mathcal{R}T} = a_1(1 - \ln T) - \sum_{n=2}^{N} \frac{a_n T^{(n-1)}}{n(n-1)} + \frac{a_{N+1}}{T} - a_{N+2} \quad (2.24)$$

The 7-term NASA polynomial is defined as:

$$\frac{\bar{g}^0}{\mathcal{R}T} = a_1(1 - \ln T) - \frac{a_2}{2} T - \frac{a_3}{6} T^2 - \frac{a_4}{12} T^3 - \frac{a_5}{20} T^4 + \frac{a_6}{T} - a_7 \quad (2.25)$$

Note that the thermodynamic properties calculated using the 7-term NASA polynomials are dimensionless. To convert them into dimensional form, the results must be multiplied by $\mathcal{R}$ for specific heat capacity and entropy and by $\mathcal{R}T$ for enthalpy and Gibbs free energy.

2.2.2 Chemical Equilibrium

Usually, the combustion process happens at temperatures where the formation of unstable products exists, occurring dissociation and the formation of even more chemical species (CO, OH, H_2, H, and O) through a chemical reaction, for example:

$$CO_2 \rightleftharpoons CO + \frac{1}{2} O_2 \quad (R1)$$

$$O_2 \rightleftharpoons 2\,O \quad (R2)$$

$$H_2O \rightleftharpoons H_2 + 0.5\,O_2 \quad (R3)$$

$$H_2O \rightleftharpoons H + OH \quad (R4)$$

The symbol $\rightleftharpoons$ indicates that the two reactions occur simultaneously in the forward and reverse path. The forward reactions (from left to right) are endothermic, and the reverse reactions are exothermic. Taking as an example R1, the dissociation of CO_2 is endothermic, and the formation of CO_2 is exothermic. For each value of pressure and temperature, these two equations happen at different rates. However, the tendency is to reach a chemical balance, where the rate of dissociation and formation of CO_2 is equal.

The equilibrium conditions are given by combining the First and Second Laws of thermodynamics. Considering the First Law of Thermodynamics applied to a closed system and neglecting the kinetic and potential energy, the internal energy variation is given by the sum of the system's heat exchange and the work applied or done by the system. Considering that only pressure forces are applied to the system, it is possible to write:

$$dU = dQ - pdV \quad (2.26)$$

As for the second law, considering a closed system and a reversible process, the heat exchanged by the system can be related to the entropy variation in the following way:

$$dS = d_eS = \frac{dQ}{T} \Leftrightarrow dQ = Td_eS \quad (2.27)$$

Where d_eS expresses the entropy variation due to the heat exchange between the system and the exterior. On the other hand, if the process is irreversible, it is necessary to consider the entropy variation due to the system's irreversibility:

$$dS = d_eS + d_iS = \frac{dQ}{T} + d_iS \quad (2.28)$$

Where d_iS represents the entropy variation due to the irreversibility. Combining the two laws for a reversible process:

$$dU = Td_eS - pdV \Leftrightarrow dU = TdS - pdV \quad (2.29)$$

Or, for an irreversible process:

$$dU = TdS - pdV - Td_iS \quad (2.30)$$

Taking a reactive system where the internal energy and volume are constant, the equilibrium conditions can be described using Equations 2.29 and 2.30:

$$(dS)_{U,V} \geq 0 \quad (2.31)$$

A similar relation could be reached in a reactive system with constant entropy and volume. However, processes at constant internal energy and volume, or at constant entropy and

volume, are not commonly found in combustion. In these cases, the Gibbs free energy or Helmholtz free energy (F) are more suitable. Considering an infinitesimal variation of Gibbs free energy and expressing enthalpy in terms of internal energy, it is possible to write:

$$dG = dH - TdS - SdT = (dU + pdV + Vdp) - TdS - SdT \quad (2.32)$$

Rewriting the above equation using Equation 2.30:

$$dG = Vdp - Td_iS - SdT \quad (2.33)$$

Therefore, in a combustion process with constant pressure and temperature, the equilibrium condition is given by:

$$(dG)_{p,T} \leq 0 \quad (2.34)$$

2.2.3 Equilibrium Reaction Rate

For a system at constant pressure and temperature, the equilibrium composition can be calculated by minimising the Gibbs free energy. This requires computing Gibbs free energy using an equation of state. In this case, the ideal gas law was applied to Equation 2.33 for an isothermal system in chemical equilibrium:

$$dG = \frac{n\mathcal{R}T}{p}dp = n\mathcal{R}Td(\ln p) \quad (2.35)$$

For an ideal mixture of ideal gases:

$$G(T,p) = \sum_{i=1}^{N} n_i \bar{g}_i(T,p) = \sum_{i=1}^{N} n_i \left[\bar{g}_i^0(T) + \mathcal{R}T \ln\left(p_i/p^0\right)\right] \quad (2.36)$$

Where p_i is the partial pressure of specie i and $\bar{g}_i^0(T)$ is the molar Gibbs free energy of specie i at temperature T and at standard pressure p^0. Similarly to enthalpy, Gibbs free energy can be written as the sum of the Gibbs free energy of formation ($\bar{g}_{f,i}^0$) and the sensible Gibbs free energy ($\bar{g}_{s,i}^0$):

$$\bar{g}_i^0(T) = \bar{g}_{f,i}^0(T_{ref}) + \Delta\bar{g}_{s,i}^0(T) \quad (2.37)$$

Where $\Delta\bar{g}_{s,i}^0$ is defined by:

$$\Delta\bar{g}_{s,i}^0(T) = \int_{Tref}^{T} d\bar{g}_i^0 \quad (2.38)$$

Differentiating Equation 2.36:

$$dG(T,p) = \sum_{i=1}^{N} dn_i \left[\bar{g}_i^0(T) + \mathcal{R}T \ln\left(p_i/p^0\right)\right] + \sum_{i=1}^{N} n_i d\left[\bar{g}_i^0(T) + \mathcal{R}T \ln\left(p_i/p^0\right)\right] \quad (2.39)$$

The last term in the equation is null because $d\bar{g}_i^0$ is equal to 0 for constant temperature. Since pressure is also constant, the equation can be reformulated as:

$$dG(T,p) = \sum_{i=1}^{N} dn_i \left[\bar{g}_i^0(T) + \mathcal{R}T \ln\left(p_i/p^0\right)\right] = 0 \quad (2.40)$$

Considering a generic reaction in equilibrium:

$$a\,\mathrm{A} + b\,\mathrm{B} + ... \rightleftharpoons e\,\mathrm{E} + f\,\mathrm{F} + ... \quad (R5)$$

Where A, B, ..., E, F, ... represent the chemical species present in combustion, and a, b, ..., e, f, ... are the stoichiometric coefficients for each species. Taking into consideration that the variation in the number of moles for each species is directly proportional to the respective stoichiometric coefficient:

$$-\frac{dn_A}{a} = \frac{dn_B}{b} = ... = \frac{dn_E}{e} = \frac{dn_F}{f} = ... \quad (2.41)$$

Equation 2.40 can be modified:

$$\begin{aligned} &a\left[\bar{g}_A^0(T) + \mathcal{R}T \ln\left(p_A/p^0\right)\right] + b\left[\bar{g}_B^0(T) + \mathcal{R}T \ln\left(p_B/p^0\right)\right] + ... \\ &- e\left[\bar{g}_E^0(T) + \mathcal{R}T \ln\left(p_E/p^0\right)\right] - f\left[\bar{g}_F^0(T) + \mathcal{R}T \ln\left(p_F/p^0\right)\right] - ... = 0 \end{aligned} \quad (2.42)$$

Rearranging the above equation:

$$\begin{aligned} &a\bar{g}_A^0(T) + b\bar{g}_B^0(T) + ... - e\bar{g}_E^0(T) - f\bar{g}_F^0(T) - ... = \\ &= \mathcal{R}T \ln\left[\frac{\left(p_e/p^0\right)^e \left(p_f/p^0\right)^f ...}{\left(p_a/p^0\right)^a \left(p_b/p^0\right)^b ...}\right] \end{aligned} \quad (2.43)$$

On the left side of the equation is the Gibbs free energy variation at standard pressure ($\Delta G^0(T)$). As for the right-hand side of the equation, the logarithm argument is designated as the equilibrium constant (k_p). Therefore, the above equation can be simplified into:

$$-\Delta G^0(T) = \mathcal{R}T \ln(k_p) \quad (2.44)$$

Which can be easily rearranged into:

$$k_p = e^{-\frac{\Delta G^0}{\mathcal{R}T}} \quad (2.45)$$

On the other hand, the equilibrium constant can also be written concerning the species' molar concentrations (k_c):

$$k_c = \frac{[E]^e [F]^f \dots}{[A]^a [B]^b \dots} \quad (2.46)$$

Contrary to k_p, this equilibrium constant depends not only on temperature but also on the mixture mole number. They can be related using the following expression:

$$k_p = k_c \left(\frac{\mathcal{R}T}{p^0}\right)^{e+f+\dots-a-b-\dots} \quad (2.47)$$

2.3 Modelling Strategies for Combustion Chemistry

A careful analysis of combustion models reveals that different chemical descriptions can be selected based on the desired level of accuracy and computational efficiency. Common approaches include detailed and reduced kinetic mechanisms, global reaction models or chemical equilibrium models.

Chemical equilibrium models assume infinite reaction rates and rely solely on thermodynamic states using Gibbs free energy minimisation to predict combustion product concentrations. This assumption is valid for fast-reacting systems, such as hydrogen combustion, and represents a sound implementation strategy because it requires minimal computational effort. However, it is unsuitable for hydrocarbons, which require more detailed chemical models [38].

Global reaction models simplify combustion by using a single global reaction. The approach is only valid for a limited range of pressure and temperature because the equation's exponentials are adjusted by curve-fitting experimental data. Due to this, the mechanism's ability to predict the reaction rate is highly depends on the precision of the experimental apparatus [9]. However, this sacrifice reduces the computational effort compared to the detailed and reduced kinetic mechanisms.

Detailed kinetic mechanisms account for all major combustion species and incorporate pressure and temperature dependencies, providing highly accurate predictions and capturing subtle combustion effects, such as ignition, flame propagation, and quenching. However, simulating detailed chemical kinetics in complex combustion systems often demands significant computational resources due to the intricate and tightly coupled reaction pathways. To reduce this computational effort, simplified or reduced kinetic mech-

anisms can be employed, providing a more efficient alternative while preserving the essential chemical behaviour. This approach cuts the numerical workload by reducing the number of elementary reactions in a mechanism. The aim is to keep critical species and pathways to maintain a good solution. It can be used when a detailed mechanism is too expensive and a global mechanism, or chemical equilibrium model is too naive.

Considering that the current work is being developed for later implementation in a more complex model, it would be naive to adopt a global reaction approach. The dependence on the accuracy and limitations of the experimental apparatus, combined with the limitations of the pressure and temperature ranges, makes the global mechanism less attractive to implement. On the other hand, an approach using a detailed or reduced kinetic mechanism could provide a trustworthy prediction and a more flexible temperature and pressure range, which is extremely important in high-pressure combustion where temperature and pressure gradients are enormous.

2.4 Chemical Kinetics Parametrisation

To distinguish between the two directions of a given reaction, a clear notation system is used. For example, R2 represents the reaction proceeding in the forward direction, while R2b refers to the reverse of the same reaction. The suffix "b" indicates the backward path, allowing for consistent identification of reversible reactions. Correspondingly, the rate constants for these reactions are denoted as k_f for the forward rate constant and k_b for the reverse (or backward) rate constant.

2.4.1 Global and Elementary Reactions

The reaction between a moles of fuel (A) and b moles of oxidiser (B) to form e and f moles of combustion products (E and F) can be represented by a global reaction mechanism:

$$a\,\mathrm{A} + b\,\mathrm{B} \rightleftharpoons e\,\mathrm{E} + f\,\mathrm{F} \quad \text{(R6)}$$

Taking the generic global reaction R6 and considering the reaction irreversible, the global reaction rate of species A can be described by the following equation:

$$\frac{d[A]}{dt} = \dot{\omega}_A = -k[A]^a[B]^b \quad (2.48)$$

Where $[X_i]$ represents the molar concentration of species X_i, and k is the proportionality constant designated by reaction rate constant, or rate coefficient. The exponents a and b specify the order for A and B, respectively, and the sum of all the exponents gives the reaction order. Therefore, it is clear that the reaction rate constant unit will depend on

the individual species orders. It can generically be defined as $(\text{mol m}^{-3})^{1-(a+b)}\ \text{s}^{-1}$ [36].

However, this equation does not represent what happens at the molecular scale; it merely represents the initial and final states of the reaction. In reality, between the initial and final states, numberless elementary chemical equations take place, where several intermediate species can be taken into consideration, whether molecules, atomic elements or radicals. An elementary reaction happens at a molecular scale, like, for example:

$$H_2 + OH \rightleftharpoons H_2O + H \quad \text{(R7)}$$

A kinetic mechanism, or reaction mechanism, comprises a set of elementary reactions necessary to describe a chemical reaction. Depending on the fuel, oxidiser, and the number of species involved, the mechanism may require numerous elementary reactions, sometimes numbering in the hundreds. These mechanisms are developed through a combination of theoretical and experimental studies. They can differ between authors based on the number of species and reactions considered, the reaction rates values, and the temperature and pressure ranges for which they are validated [36].

At first glance, the number of possible reactions in a combustion mechanism can appear overwhelming. For a system with N species, there are N^2 potential reactant pairs, each capable of forming multiple products. However, many of these mathematically possible reactions are chemically infeasible or occur at negligible rates. Therefore, constructing a realistic mechanism involves selecting only those reactions that proceed rapidly enough to influence the overall combustion process significantly [39].

Elementary reactions are classified based on their molecularity, which refers to the number of reactant species involved in a single reaction step. If only one reactant is involved, the reaction is unimolecular. When two reactants participate, it is classified as a bimolecular reaction. Finally, if three reactants are involved simultaneously, the reaction is considered termolecular. Each type can be represented as follows:

$$A \longrightarrow \text{products} \quad \text{(R8)}$$

$$A + B \longrightarrow \text{products} \quad \text{(R9)}$$

$$A + B + M \longrightarrow C + M \quad \text{(R10)}$$

Where A, B, and C are random chemical species, and M is a catalytic species.

Similarly to the global reaction, the reaction rate for a given intermediate species in an elementary reaction can be written as follows for unimolecular, bimolecular, and termolecular, respectively:

$$\frac{d[A]}{dt} = -k[A] \quad (2.49)$$

$$\frac{d[A]}{dt} = -k[A][B] \quad (2.50)$$

$$\frac{d[A]}{dt} = -k[A][B][M] \quad (2.51)$$

If an elementary reaction is reversible, the formation of reactants from the products should be considered in the calculation of the reaction rate of a given intermediate species. Taking R5 as an example:

$$\frac{d[A]}{dt} = -k_f[A][B]... + k_b[E][F]... \quad (2.52)$$

Where k_f is the forward reaction rate constant and k_b is the reverse reaction rate constant.

2.4.1.1 Three-body Reactions

In radical–radical reactions, a third-body species, often referred to as a catalytic partner or chaperone, is required to absorb the excess energy released during the formation of a stable molecule. During the collision, the excess internal energy of the newly formed molecule is transferred to the third body, M, which carries it away in the form of increased kinetic energy. Without this energy transfer, the product molecule would not remain stable and would instead dissociate back into its original radicals [9]. The third body, M, can be any species present in the system that allows the conservation of both momentum and energy during the reaction [39]. This includes inert gases such as helium or argon, which are often added to stabilise the fuel–oxidiser mixture [36].

The third-body partner will take up the most importance in pressure-dependent reaction [40], as will be seen in Subsection 2.4.4. Generally, when known, the third-body efficiencies are specified for a handful of common species in relation to nitrogen, argon, or helium. When not specified, the third-body efficiency is implicitly assumed to be unity for a given species [40]. Taking that into consideration that $[M]$ can be calculated through

the sum of all chemical species concentration weighted by their catalytic efficiencies (ε_i):

$$[M] = \sum_{i=1}^{N} \varepsilon_i \, [X_i] \quad (2.53)$$

If a specific species is designated as the collision partner, the effective third-body concentration is equal to the concentration of that species. In this case, the third-body efficiency of the selected species is considered to be unity, while the efficiencies of all other species are assumed to be zero.

Water molecules are excellent third-body partners, with efficiencies that can be 10-50 times larger than those of argon or helium. Indeed, chaperone efficiencies increase with the number of degrees of freedom available to share collisional energy. Atomic species, such as argon or helium, are comparatively inefficient, followed by diatomic species, like N_2 and O_2, and lastly by polyatomic species.

2.4.2 Collision Theory

The rate constant can be theoretically estimated using collision theory. For a reaction involving two moving species, A and B, as represented in reaction 9, the collision frequency within a given volume can be calculated using the hard-sphere model. This model assumes that molecules behave as rigid spheres, and the following expression gives the frequency of collisions between A and B:

$$\frac{Z_{AB}}{V} = \left(\frac{n_A N_A}{V}\right)\left(\frac{n_B N_A}{V}\right)\sqrt{\frac{8\kappa T}{\pi \mu_{AB}}}\left(\pi \sigma_{AB}^2\right) \quad (2.54)$$

Where Z_{AB} is the collision frequency between molecules A and B, V is the mixture volume, n_{X_i} is the number of moles of specie X_i, N_A is the Avogrado number, κ is the Boltzmann constant, T is the mixture temperature, σ_{AV} is the mean diameter of species A and B ($\sigma_{AB} = 0.5(\sigma_A + \sigma_B)$) and, μ_{AB},

$$\mu_{AB} = \frac{m_A m_B}{m_A + m_B} \quad (2.55)$$

Where m_{X_i} the mass of specie X_i. The reaction rate of species A can be related to the collision frequency by the following equation:

$$\frac{d[A]}{dt} = -\left(\frac{Z_{AB}}{dV}\right)\left[S\, e^{\left(-\frac{E_a}{\mathcal{R}T}\right)}\right]\frac{1}{N_A} \quad (2.56)$$

Where S is the probability of a molecule's orientation allowing the occurrence of a chemical reaction, E_a is the activation energy, and $\mathcal{R}$ is the universal gas constant. Combining

Equations 2.48 and 2.56 is possible to calculate the rate constant through the following equation:

$$k = N_A \sigma_{AB}^2 \sqrt{\frac{8\pi\kappa T}{\mu_{AB}}} \left[S\, e^{\left(-\frac{E_a}{\mathcal{R}T}\right)} \right] \quad (2.57)$$

Equation 2.57, derived from collision theory, provides only a rough estimate of the rate constant and often lacks accuracy. This is because it does not account for molecular structure or the complexities of bond formation and dissociation. To achieve more precise predictions, more advanced approaches such as transition-state theory are required [36, 39]. However, when the temperature range is relatively narrow, the rate constant can be approximated using a simplified expression known as the Arrhenius equation:

$$k = A\, e^{\left(-\frac{E_a}{\mathcal{R}T}\right)} \quad (2.58)$$

Where A is a pre-exponential factor that includes the effects multiplied by the Boltzmann constant in Equation 2.57.

In this formulation, the rate constant is independent of concentration, and the variation of ln(k) is linear with the inverse of temperature [36]. However, over the broader temperature ranges typically encountered in combustion processes, significant non-Arrhenius behaviour is often observed, and Equation 2.58 fails to capture it accurately. This discrepancy arises because the Arrhenius equation assumes a constant pre-exponential factor, neglecting its inherent temperature dependence. To improve predictive accuracy, temperature dependence must be taken into account. A common approach is to introduce a temperature exponential factor, n, resulting in the modified Arrhenius equation [39]:

$$k = AT^{\beta}\, e^{\left(-\frac{E_a}{\mathcal{R}T}\right)} \quad (2.59)$$

The use of T^{β} improves the accuracy of temperature dependence predictions in terms involving the Boltzmann constant. The Arrhenius parameters (A, β, and E_a) are widely available in the literature and are tabulated for different elementary reactions, typically derived from experimental studies. However, these experimentally determined values often come with significant uncertainties, which can affect the accuracy of mechanism predictions under certain conditions.

Pressure dependence in some elementary reactions is even more challenging to define precisely. In such cases, the dependence is often modelled using two or more modified Arrhenius equations. Occasionally, computed results may fail to match experimental observations unless one or more rate expressions are assigned values that deviate significantly from known experimental data. This typically signals that the assumed reaction mechanism is incomplete or that other aspects of the mechanism or physical model re-

quire revision [39].

2.4.3 Rate Constants for Generic Kinetic Mechanisms

Considering a mechanism composed by reaction R29, R20, R22 and R28 it is possible to write the variation of a specie concentration in time, from Equation 2.48. Taking oxygen as an example:

$$\begin{aligned}\frac{d\left[O_2\right]}{dt} = &- k_{b29}\left[H_2\right]\left[O_2\right] - k_{f20}\left[H\right]\left[O_2\right] - k_{f28}\left[H\right]\left[O_2\right]\left[M\right] \\ &+ k_{f29}\left[HO_2\right]\left[H\right] + k_{b20}\left[O\right]\left[OH\right] + k_{b28}\left[HO_2\right]\left[M\right]\end{aligned} \tag{2.60}$$

This description enables an explicit formulation, facilitating easy interpretation. However, it cannot apply to every reaction mechanism because it lacks generalisation. Therefore, to implement it in a numerical code, a more abstract description should be considered. First, it is necessary to describe a generic reaction in a mechanism:

$$\sum_{s=1}^{S} \nu_{rs}^{'} X_s \rightleftharpoons \sum_{s=1}^{S} \nu_{rs}^{''} X_s, \quad r = 1, 2, ..., R \quad \text{(R11)}$$

The above reaction describes a generalised reaction in a mechanism considering S species and R reactions, where $\nu_{rs}^{'}$ and $\nu_{rs}^{''}$ are the stoichiometric coefficients of each species (X_s) in the reactants and products, respectively. The production rate of species X_s ($\dot{\omega}_s$) can now be defined in a kinetic mechanism with R reactions [9] as:

$$\dot{\omega}_s = \sum_{r=1}^{R} \nu_{rs} q_r \tag{2.61}$$

Where ν_{rs} is defined by:

$$\nu_{rs} = \nu_{rs}^{''} - \nu_{rs}^{'} \tag{2.62}$$

And q_r represents the rate-of-progress variable [9] of reaction r defined by:

$$q_r = k_{f,r} \prod_{s=1}^{S} [X_s]^{\nu_{rs}^{'}} - k_{b,r} \prod_{s=1}^{S} [X_s]^{\nu_{rs}^{''}} \tag{2.63}$$

For a reaction where a third-body collision exists, the concentration of the effective third-body must appear in the expression for the rate-of-progress variable. Equation 2.63 is then modified considering the effective third-body concentration definition in Equation

2.53:

$$q_r = \left(\sum_{s=1}^{S} \varepsilon_{rs} \left[X_s \right] \right) \left(k_{f,r} \prod_{s=1}^{S} [X_s]^{\nu'_{rs}} - k_{b,r} \prod_{s=1}^{S} [X_s]^{\nu''_{rs}} \right) \quad (2.64)$$

Considering all species for the consumption and formation of a given species in the production rate evaluation:

$$\dot{\omega}_s = \frac{d\left[X_s\right]}{dt} = \sum_{r=1}^{R} \nu_{rs} \left(\sum_{s=1}^{S} \varepsilon_{rs} \left[X_s \right] \right) \left(k_{f,r} \prod_{s=1}^{S} [X_s]^{\nu'_{rs}} - k_{b,r} \prod_{s=1}^{S} [X_s]^{\nu''_{rs}} \right) \quad (2.65)$$

2.4.3.1 Reverse Reaction Rate Constant

As mentioned above, the experimentally determined rate constants can sometimes have a significant uncertainty. On the other hand, equilibrium reaction rates, calculated through experimental thermodynamic data, as seen in Section 2.2.3, are well known with good precision. Therefore, it is common practice to calculate the reverse rate constant through the equilibrium rate constant and the forward rate constant or vice-versa, depending on the better-known rate constant (forward or reverse). To do so, it is necessary to consider that the forward and reverse reaction rates are equal in equilibrium. Considering the generic reaction R6 in an equilibrium state (production rate is null):

$$k_f \left[A\right]^a \left[B\right]^b = k_b \left[E\right]^e \left[F\right]^f \quad (2.66)$$

Using Equation 2.46, it is possible to write:

$$\frac{k_f}{k_b} = \frac{\left[E\right]^e \left[F\right]^f}{\left[A\right]^a \left[B\right]^b} = k_c \quad (2.67)$$

Finally, using Equation 2.47, it is possible to relate the equilibrium constant to the forward and reverse rate constants:

$$k_p = \frac{k_f}{k_b} \left(\frac{\mathcal{R}T}{p^0} \right)^{e+f-a-b} \quad (2.68)$$

Rearranging to calculate the reverse reaction rate constant:

$$k_b = \frac{k_f}{k_p} \left(\frac{\mathcal{R}T}{p^0} \right)^{e+f-a-b} \quad (2.69)$$

Where k_p is the reaction rate constant in equilibrium, and k_f is the forward reaction rate constant.

For a generic reaction in a kinetic mechanism:

$$k_{b,r} = \frac{k_{f,r}}{k_{p,r}} \left(\frac{\mathcal{R}T}{p^0} \right)^{\sum_{r=1}^{R} \nu_{rs}} \quad (2.70)$$

2.4.4 Pressure Dependence

In some cases, bimolecular reactions are considered first-order reactions due to the fast consumption of the species and, therefore, will be present at a lower concentration. Taking R9 as an example, the reaction rate is given by Equation 2.50, but if the concentration of B is much larger than the concentration of A, then the concentration of B is approximately constant and a modified reaction rate can be written:

$$\frac{d[A]}{dt} = -k^{'}[A] \quad (2.71)$$

In this case, the bimolecular reaction is of first order. However, $k^{'}$ depends on the concentration of B, and therefore, it will be pressure-dependent. Lindemann [41] showed this behaviour through a sequence reaction of three elementary reactions, describing the global reaction:

$$\mathrm{A} + \mathrm{M} \longrightarrow \text{products} \quad (R12)$$

They are:

$$\mathrm{A} + \mathrm{M} \longrightarrow \mathrm{A^*} + \mathrm{M} \quad (R13)$$

$$\mathrm{A^*} + \mathrm{M} \longrightarrow \mathrm{A} + \mathrm{M} \quad (R14)$$

$$\mathrm{A^*} \longrightarrow \text{products} \quad (R15)$$

Considering k_f, k_b, and k_p the rate constant for the three reactions, respectively, and A* as the radical of species A, the rate law for these two species can be then be written as in it follows:

$$\frac{d[A]}{dt} = -k_f[A][M] + k_b\left[A^*\right][M] \quad (2.72)$$

$$\frac{d[A^*]}{dt} = k_f[A][M] - k_b\left[A^*\right][M] - k_p\left[A^*\right] \quad (2.73)$$

Considering a quasi-stationary state, where the reaction rate for the excited species is considered approximately zero because it disappears very quickly after it formation (it is a very reactive species):

$$\left[A^*\right] = \frac{k_f\left[A\right]\left[M\right]}{k_b\left[M\right] + k_p} \quad (2.74)$$

Replacing in the rate law equation for A:

$$\frac{d\left[A\right]}{dt} = -\frac{k_f k_p}{k_b\left[M\right] + k_p}\left[A\right]\left[M\right] = -k_{diss}\left[A\right] \quad (2.75)$$

Where k_{diss} is the rate constant associated with the dissociation of A*. Considering the concentrations as pressure-dependent and the rate constants as pressure independent, it is possible to evaluate the behaviour of the rate law in the low and high-pressure limits, respectively:

$$\lim_{p\to 0}\frac{d\left[A\right]}{dt} = -\lim_{p\to 0}\frac{k_f k_p}{k_b\left[M\right] + k_p}\left[A\right]\left[M\right] = -k_f\left[A\right]\left[M\right] = -k_{diss,0}\left[A\right] \quad (2.76)$$

$$\lim_{p\to \infty}\frac{d\left[A\right]}{dt} = -\lim_{p\to \infty}\frac{k_f k_p}{k_b + \frac{k_p}{[M]}}\left[A\right] = \frac{k_f k_p}{k_b}\left[A\right] = -k_{diss,\infty}\left[A\right] \quad (2.77)$$

As previously mentioned, the bimolecular reaction will be of the first order at high pressures and a second-order response at the low-pressure limit. A similar consideration can be made for termolecular reactions, where the reaction order is second order at high pressures and third order at low pressures. As Lindemann showed, the reaction will have two different behaviours depending on the pressure regime. Taking into consideration the methyl recombination, in the high-pressure limit, the reaction occurs like:

$$CH_3 + CH_3 \rightleftharpoons C_2H_6 \quad (R16)$$

However, in the low-pressure limit, the reaction needs a third-body collision partner to provide the necessary energy for the reaction to occur. In this case, the reaction can be written as follows:

$$CH_3 + CH_3 + M \rightleftharpoons C_2H_6 + M \quad (R17)$$

When the system pressure is within either limit, the rate constant can be obtained through Equation 2.59 with the proper Arrhenius values for each pressure limit, where the reaction will only exhibit normal temperature-dependent behaviour. However, at intermediate pressures ("fall-off" region), the rate constant can be more challenging to calculate, and various methods can be considered [42]. In this case, the proper way to represent the

reaction is:

$$CH_3 + CH_3\,(+M) \rightleftharpoons C_2H_6\,(+M) \quad \text{(R18)}$$

Where M represents the third body partner. Different approaches can be considered to model the fall-off region. One of the simplest approaches was provided by Lindemann, which considers a rate constant for the low- and high-pressure limits, k_0 and k_∞, respectively. Each rate constant has its proper Arrhenius values, as described above:

$$k_0 = A_0 T^{\beta_0}\, e^{\left(-\frac{E_{a,0}}{\mathcal{R}T}\right)} \quad (2.78)$$

$$k_\infty = A_\infty T^{\beta_\infty}\, e^{\left(-\frac{E_{a,\infty}}{\mathcal{R}T}\right)} \quad (2.79)$$

The rate constant at any pressure is calculated by:

$$k = k_\infty \left(\frac{p_r}{1+p_r}\right) F \quad (2.80)$$

Here, the reduced pressure is given by:

$$p_r = \frac{k_0\,[M]}{k_\infty} \quad (2.81)$$

For the Lindemann approach in Equation 2.80, F is unity [42]. On the other hand, Troe [43] proposed a dimensionless pressure scale defined by the two rate constants for the pressure limits ($p \to 0$ and $p \to \infty$):

$$\frac{k_{diss,0}}{k_{diss\infty}} = \frac{k_b}{k_p}\,[M] \quad (2.82)$$

Considering the definition of k_{diss} and $k_{diss,\infty}$:

$$\frac{k_{diss}}{k_{diss,\infty}} = \frac{\frac{k_{diss,0}}{k_{diss,\infty}}}{\frac{k_{diss,0}}{k_{diss,\infty}} + 1} \quad (2.83)$$

For high pressures, $k_{diss}/k_{diss,\infty}$ will go to 1, whereas for low pressures $k_{diss}/k_{diss,\infty}$ is linearly proportional to pressure [36]. The Troe approach can then be implemented by modifying Equation 2.80, through function F. In this approach, function F is defined by:

$$\log F = \left[1 + \left[\frac{\log p_r + c}{n - d(\log p_r + c)}\right]^2\right]^{-1} \log F_{cent} \quad (2.84)$$

Where:

$$c = -0.4 - 0.67 \log F_{cent} \quad (2.85)$$

$$n = 0.75 - 1.27 \log F_{cent} \quad (2.86)$$

$$d = 0.14 \quad (2.87)$$

$$F_{cent} = (1 - \alpha) e^{-T/T^{***}} + \alpha e^{-t/T^{*}} + e^{T^{**}/T} \quad (2.88)$$

When building a kinetic mechanism, authors can either present the values for the four parameters in the "centre-broadening parameter" (F_{cent}) or give a direct value for it.

The last approach presented herein is by Stewart et al. [44], which is similar to Troe's and is implemented by modifying the F function to the following format:

$$F = d \left[a e^{-b/T} + e^{-T/c} \right]^{X} T^{e} \quad (2.89)$$

Where:

$$X = \frac{1}{1 + \left(\log p_r\right)} \quad (2.90)$$

In the original formulation, the parameters a, b, and c are used to fit the experimental data. Additionally, although not mandatory, the parameters d and e can be included to simulate stronger or weaker molecular collisions, enhancing model flexibility [42].

Reaction 18 is an unimolecular/recombination fall-off reaction. However, other reactions can exhibit a behaviour characterised by pressure dependence, as seen in chemically activated bimolecular reactions. For example:

$$CH_3 + CH_3 \,(+\,M) \rightleftharpoons C_2H_5 + H \,(+\,M) \quad (R19)$$

The rate constant for these reactions can be calculated by:

$$k = k_0 \left(\frac{1}{1 + p_r} \right) F \quad (2.91)$$

The equation is analogous to Equation 2.80, and the parameters can be calculated similarly. Other approaches can be found in the literature, but they transcend the scope of the present work.

As will be discussed later in chapter 4.1, the present model employs only the Lindemann and Troe formulations, since the majority of the kinetic mechanisms analysed adopt exclusively these two approaches.

Chapter 3

State of the Art

The following chapter is organised into three sections. Section 3.1 discusses the reasoning behind selecting the hydrogen-oxygen reaction as the focus of this study, based on its relevance and performance in modern rocket propulsion. Section 3.2 presents the common reactions within the H_2-O_2 kinetic mechanism, the reaction path under different circumstances, and it briefly introduces the explosion limits of H_2-O_2 combustion. Finally, Section 3.3 examines different kinetic mechanisms in the literature and compares them to select the mechanism to be implemented.

Due to the current work's scope, the literature review does not focus on the influence of other modelling features, such as mixing, thermodynamic, and transport models, on simulation results. Instead, the aim is to lay the foundations for the analysis of kinetic mechanism behaviour under different operating conditions.

3.1 H_2-O_2 as a Reference Reaction

As discussed in Section 1.3, the hydrogen and oxygen propellant pair is among the most widely used in rocket engines, primarily due to its high specific impulse. This makes it a highly relevant reaction to study in the context of propulsion research. Additionally, as will be shown in Section 3.2, kinetic mechanisms are typically developed in a hierarchical structure. The hydrogen and oxygen reaction serves as the foundational basis for more complex models involving hydrocarbons and their derivatives, such as methane, kerosene, or RP-1, which are also widely used and recognised for their high performance. Therefore, a detailed study of the hydrogen and oxygen reaction is essential for both its direct relevance and its role in supporting the development of broader kinetic models.

3.2 Detailed H_2-O_2 Kinetic Mechanism

A kinetic mechanism is developed systematically and hierarchically, beginning with simpler species and reactions and gradually adding new and more complex ones. Each stage must be tested and validated by comparing numerical results with experimental data. However, the validation could be challenging because different experimental conditions could shift the dominant reaction pathway. For example, hydrogen atoms may dominate in fuel-rich hydrocarbon systems, while at fuel-lean conditions, atomic oxygen and

hydroxyl radicals become more significant. Thermochemical data, including heats of formation, specific heat, entropy, and enthalpy, are also crucial and must complement reaction rate information [39]. Consequently, a kinetic mechanism is a flexible model that evolves in response to new experimental insights.

For the construction of a kinetic mechanism, it is crucial to select the necessary species and reactions that happen rapidly enough and impact the overall combustion process. For any combustion, a primarily sequential fragmentation of the initial fuel molecule into smaller intermediate species takes place. Ultimately, these intermediate species are converted to final products like H_2O_2 for the hydrogen/oxygen combustion, with the addition of CO_2 for the hydrocarbon/oxygen combustion.

The base of the hydrogen-oxygen (H_2-O_2) system is composed of simpler elements like H, O, OH, and H_2O in eight reactions, divided into two groups of four reactions each: "H_2-O_2 Chain Reactions" and "H_2-O_2 Dissociation/Recombination Reactions". Some earlier mechanisms used only these eight reactions to describe the hydrogen-oxygen combustion, like the Pergament mechanism [45], which was later used by Spiegler [46]. The "Chain Reactions" group is composed of the following reactions:

$$H + O_2 \rightleftharpoons O + OH \quad \text{(R20)}$$

$$O + H_2 \rightleftharpoons H + OH \quad \text{(R21)}$$

$$H_2 + OH \rightleftharpoons H_2O + H \quad \text{(R22)}$$

$$O + H_2O \rightleftharpoons OH + OH \quad \text{(R23)}$$

And, the "Recombination/Dissociation Reactions" group include:

$$H + H + M \rightleftharpoons H_2 + M \quad \text{(R24)}$$

$$O + O + M \rightleftharpoons O_2 + M \quad \text{(R25)}$$

$$O + H + M \rightleftharpoons OH + M \quad \text{(R26)}$$

$$H + OH + M \rightleftharpoons H_2O + M \quad \text{(R27)}$$

Later, more complex species were added to the kinetic mechanism to improve model predictions of hydroperoxyl and hydrogen peroxide. The hydroperoxyl radical (HO_2) was

initially proposed to explain the explosion limit behaviour of the H_2-O_2 mixture [39]. Its consumption and creation mechanism is crucial for the good prediction of the flame behaviour [47]. The compound is formed primarily by:

$$H + O_2 + M \rightleftharpoons HO_2 + M \quad (R28)$$

And consumed by reaction with various radicals, including:

$$HO_2 + H \rightleftharpoons H_2 + O_2 \quad (R29)$$

$$HO_2 + H \rightleftharpoons OH + OH \quad (R30)$$

$$HO_2 + H \rightleftharpoons H_2O + O \quad (R31)$$

$$HO_2 + OH \rightleftharpoons H_2O + O_2 \quad (R32)$$

$$HO_2 + O \rightleftharpoons O_2 + OH \quad (R33)$$

An additional reaction involving HO_2 is:

$$O + OH + M \rightleftharpoons HO_2 + M \quad (R34)$$

The reaction of two HO_2 molecules produces hydrogen peroxide (H_2O_2), which is the last species in a hydrogen-oxygen kinetic mechanism:

$$HO_2 + HO_2 \rightleftharpoons H_2O_2 + O_2 \quad (R35)$$

Which is consumed by reactions with radicals and by thermal decomposition:

$$H_2O_2 + OH \rightleftharpoons H_2O + HO_2 \quad (R36)$$

$$H_2O_2 + H \rightleftharpoons H_2O + OH \quad (R37)$$

$$H_2O_2 + H \rightleftharpoons HO_2 + H_2 \quad (R38)$$

$$H_2O_2 + M \rightleftharpoons OH + OH + M \quad (R39)$$

Other not so common reactions in a H_2-O_2 mechanism are:

$$H_2 + O_2 \rightleftharpoons OH + OH \quad \text{(R40)}$$

$$HO_2 + H + M \rightleftharpoons H_2O_2 + M \quad \text{(R41)}$$

$$H_2O + O \rightleftharpoons H_2 + O_2 \quad \text{(R42)}$$

$$H_2O_2 + O \rightleftharpoons H_2O + O_2 \quad \text{(R43)}$$

$$HO_2 + HO_2 + M \rightleftharpoons H_2O_2 + O_2 + M \quad \text{(R44)}$$

3.2.1 Explosion limits in H_2-O_2 combustion

In H_2-O_2 combustion, it is possible to define three different regions according to the pressure and temperature regime, as it can be seen in Figure 3.1.

High temperatures and low pressures define the first explosion limit. Here, O, H, and OH will dominate the radical pool, and reactions involving the formation and decomposition of these radicals control the combustion chain [49]. This region is characterised by rapid ignition (small ignition delay times) and is controlled by chain-branching reactions. In this environment the chain-branching explosion can be described by R29b, R20, R20b, R22, and R23 [50].

A decrease in temperature will also decrease the production of fast radicals (H, O and OH) and promote chain-propagating reactions, increasing the HO_2 concentration (heavy radicals) in the radical pool. Now, a competition between R28 and R20 for the H radical pool governs the overall branching ratio in combustion and determines the second explosion limit in a homogeneous hydrogen-oxygen system. Additionally, reactions R21, and R22 could also influence this "crossover" region [51].

The chain-branching reaction R20 is responsible for the creation of a radical pool, which decreases the ignition delay time and increases fuel consumption. On the contrary, the chain-propagating reaction R28 consumes the radical pool created by the previous reaction, increasing the ignition delay time and resulting in a lower hydrogen conversion

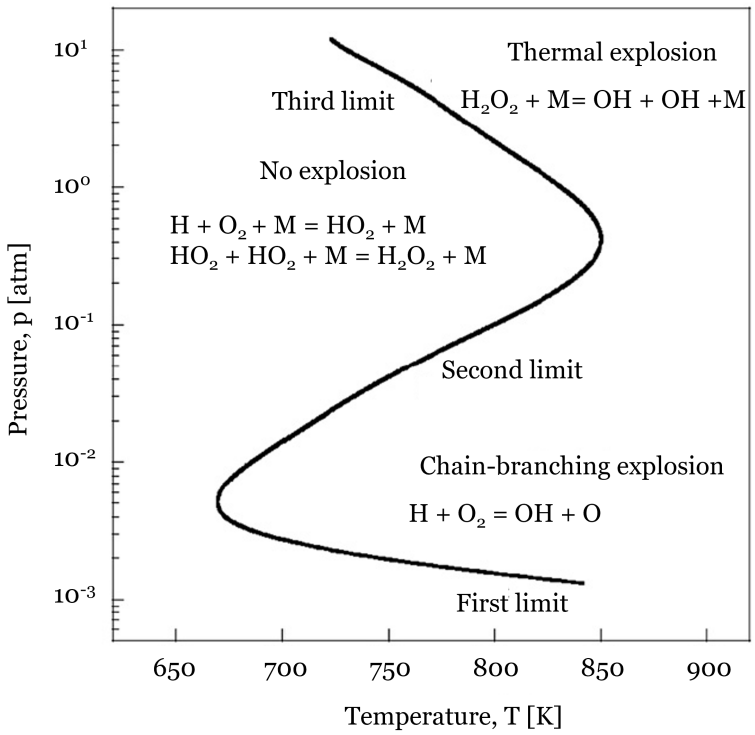

Figure 3.1: Explosion limits of a stoichiometric H_2-O_2 mixture [48].

[50, 52]. At this point, the concentration of H, O, OH, HO_2, and H_2O_2 will become in the same order of magnitude [49]. As temperature and pressure increase, and before the third explosion limit, Mueller et al. [53] observed an "extended" second explosion limit, influenced by experimental timescales and mixture dilution effects.

At higher pressure and lower temperatures lies the third explosion limit. Contrary to the first explosion limit, this region is mainly controlled by chain-propagating and chain-termination reactions, involving species such as HO_2 and H_2O_2. Here, slower and thermal combustion takes place. At pressures exceeding the third explosion limit and at lower temperatures, H_2O_2 formation from HO_2, followed by its subsequent decomposition, enables a chain-carrying reaction sequence that becomes thermally self-accelerative. This process contrasts with the faster chain-explosive kinetics observed at higher temperatures, thus leading to an extended second explosion limit due to the difference in characteristic reaction times [51].

It could be interesting to analyse the numerical results of Evans and Schexnayder [54] to see the influence of the inclusion of thermal combustion reactions in a kinetic mechanism. The authors used two different mechanisms to analyse hydrogen-air mixtures. The first one is an 8-reaction mechanism made of seven species, and the second is a 25-reaction mechanism composed of 14 species. It is important to note that the 8-reaction mechanism does not include HO_2 or H_2O_2. Through the comparison of the two mecha-

nisms, the results show that the 25-reaction mechanism is superior in predicting ignition; however, after ignition, the two models have little to no difference in their predictions. This could be due to the lack of reactions involving HO_2 and H_2O_2 at pre-ignition lower temperatures. Once ignition starts, temperatures increase, and H, O, and OH dominate the radical pool. As seen previously, reactions involving heavy radicals will become less significant, and chain-branching reactions will govern combustion, resulting in slight differences in the model results. The authors assure that the inclusion of HO_2 is essential in low-temperature ignition studies.

3.2.2 Reactions in H_2-O_2 Mechanisms

Several studies [55–59] show that the competition between reactions R20 and R28 controls the combustion mechanism of H_2/O_2, and to a certain extent the combustion of all fuels [55].

In high-temperature combustion ($T \geq 1000$ K), the chain-branching R20 dominates the oxidation process. Any kinetic perturbation that increases the production of hydrogen atoms will accelerate the overall combustion rate by increasing the net amount of chain branching from this reaction. Conversely, processes which reduce the hydrogen atom population and reactions which compete with R20 for hydrogen atoms will tend to inhibit combustion. In these conditions, the effect of R28 is low due to the negative activation energy, meaning that k_{28} will decrease with the increase of temperature [39]. Conversely, with the decrease of temperature, R28 will have a more dominant role, competing with R20 for the hydrogen atom radical pool, hence inhibiting combustion as R28 produces one slow radical (HO_2), contrary to R20 which produces two faster radicals (OH and O) [55]. To sum up, R20 is dominant in high-temperature and low-pressure environments, and R28 in low-temperature and high-pressure conditions [39].

Shimizu et al. [60] also reported this behaviour. A sensitivity analysis of ignition delay times revealed that above 1300 K, reaction R20 is the most influential. Below this temperature, both R20 and R28 exhibit the highest sensitivity. This trend is expected, as discussed in Section 3.2.1, where the competition of these two reactions defines the second explosion limit. At higher pressures, these reactions, along with R29 and R30, contribute to the definition of the extended explosion limit [51, 60].

Figure 3.2 shows the main reactions as functions of temperature for a mixture of 0.7 H_2 + O_2 + 3.76 Ar at 8, 16 and 32 bar calculated using Kéromnès et al. mechanism [55]. It is possible to see that for high temperatures, R20 is dominant, and that with decreasing temperatures, R28 will take over as the controlling reaction. For lower temperatures ($T < 1050$ K), R38 will dominate the reaction with R28.

Despite the importance of R20, agreement between research teams on the reaction rate constant is not consensual, especially at temperatures around 1100 K. The discrepancy

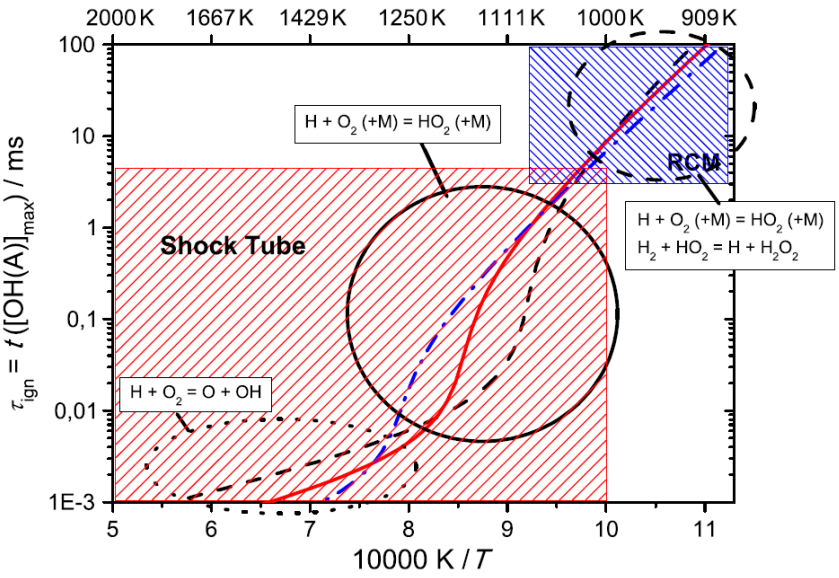

Figure 3.2: Main reactions as functions of the temperature regime for a mixture of $H_2/O_2/Ar = 0.7/1/3.76$ tested with the Kéromnès et al. mechanism at 8 bar (black dashed line), 16 bar (red solid line) and 32 bar (blue dash dotted line) [55].

between high and low temperatures could also imply a disparity in the reaction activation energy [59].

Similarly, the reaction rate constant for R28 also shows some divergences. The comparison of different studies suggests that the fall-out behaviour and the high-pressure limit yield similar results and are even insignificant at pressures below 100 atm (at 1100 K). Therefore, the discrepancies encountered in this reaction are more likely due to the low-pressure limit [59]. R28 is most sensitive to ignition delay times near the second explosion limit. The low-pressure limiting rate constant when H_2O, H_2, and O_2 are used as third-body collision partners is of prior importance under LRE operative conditions. Contrary to H_2 and O_2, a variety of experimental data exists for water as a third-body collision partner [60].

Similarly to R28, R39 is a pressure-dependent reaction and the H_2-O_2 combustion shows to be highly reactive to these two reactions in the low and intermediate temperature regime. In the low and intermediate pressure range ($p \leq 10$ atm), R28 will control reactivity, whereas, in high-pressure regimes (in the third explosion regime), R39 will dominate along with R38, becoming an essential reaction for the study of LRE combustion [55, 60]. The rate constant for the high-pressure limit in R39 presents larger uncertainties due to the lack of experimental data to validate it [59]. In high-pressure conditions, this could be the source of discrepancies between predictions and experimental data [60]. Similarly to R28, the deviation from the low-pressure limit can be insignificant considering the typical combustion conditions. [59].

The majority of research teams point to the chain-termination R32 as the reaction with

the most significant uncertainty. The rate constant presents an unusual temperature dependence at intermediate temperatures, leading to a non-Arrhenius behaviour [55]. Hippler et al. [61] discovered the rate constant minimum around 1250 K, and later Kappel et al. [62] confirmed this minimum but for a temperature of 1000 K, implying a strong temperature dependence. In both cases, after the minimum, the rate constant steeply increased with temperature. A more recent study [63] showed that for a temperature range of 1600 to 2200 K, this tendency does not occur, which agrees to a reasonable extent with the experimental study of Srinivasan et al. [64]. However, the use of this rate constant in the temperature range of 400 K to 1200 K should be done with extended caution due to the narrow minimum described by [61, 62]. The majority of the analysed mechanisms [51, 55, 56, 59, 60, 65] do not include this minimum behaviour, describing the rate constant with only one Arrhenius expression. In contrast, mechanisms like Konnov [58] and Alekseev et al. [66] use dual-Arrhenius-expressions (low-temperature and high-temperature limits) to define the reaction rate constant. Additional attention should be given to lean flame conditions where the reaction shows a high sensitivity [55].

For the reactions between HO_2 and H, three different production channels exist: R29, R30, and R31. Their rate constants and product branching ratios are important pathways, particularly at high pressures, where they are susceptible to mass burning rates [60]. R29 and R30 are also important in capturing the time-histories from flow reactors and laminar flame velocities [56, 65]. A discussion exists among authors on the relevance of R31 in the combustion mechanism. Baldwin et al. [67] are not able to decouple this reaction from R30 due to kinetic similarities. Indeed, Day et al. [68] showed that R31 is much slower than R30 ($k_{31}/k_{30} = 0.1$). However, when performing sensitivity analyses in flame burning velocities, Konnov [58] proved that R31 and R30 have different signs, and therefore must be kinetically different. Contrary to Shimizu et al. [60], Konnov [58] and other mechanisms [51, 59, 66] do not include this reaction, due to the reaction's uncertain role as a production path.

Near the third explosion limit, R35 is one of the leading producers of hydrogen peroxide (which is a crucial chain carrier for the degenerate branching mechanism). It participates in a chain-propagating sequence responsible for thermally driven oxidation kinetics at temperatures above the third explosion limit and below the extended second explosion limit [53]. Due to competition with R38b, the reaction could inhibit reactivity [55]. Furthermore, at atmospheric pressure and temperatures below 400 K, H_2O could be an essential catalyst for this reaction, though, above that temperature, the effect vanishes [58]. The reaction exhibits temperature dependence with a minimum of around 500 K, where it also shows pressure dependence, a feature not often included in kinetic models. Shimizu et al. [60] tried to describe this behaviour using a high-temperature limit rate constant, independent of pressures and a low-temperature rate that is coupled with the termolecular reaction R44 (also used by Konnov [58]). However, this approach was later criticised by Alekseev et al. [66] because Shimizu et al. [60] mixed pressure-dependent and independent terms in a Troe-type fall-off rate constant. Unlike Shimizu et al. [60], Konnov [58]

did include the pressure dependence with the inclusion of R44 separately from R35, showing its usefulness when predicting ignition delay times at lower temperatures and higher pressures. Nevertheless, Alekseev et al. [66] chose to remove the reaction when revising the Konnov mechanism [58].

R37 and R38 are possible exit channels for the same reactants. Even though they are less sensitive to the laminar flame speeds at pressures under 100 atm, rate constants were found to be sensitive to the ignition delay times at high-pressure conditions. R38 is highly sensitive at high pressures and low temperatures [55]. As seen before, R20 and R28 have a crucial role in hydrogen oxidation, competing amongst themselves at low and intermediate pressures. However, in high pressure environments ($p \geq 10$ atm) relevant for LRE, R20 loses relevance and reactions involving HO_2 and H_2O_2 gain significance. According to a sensibility analysis by Kéromnès et al. [55] shown in Figure 3.3, R38 and R39 become more sensitive than reactions R20 and R28 at a pressure of around 15 atm.

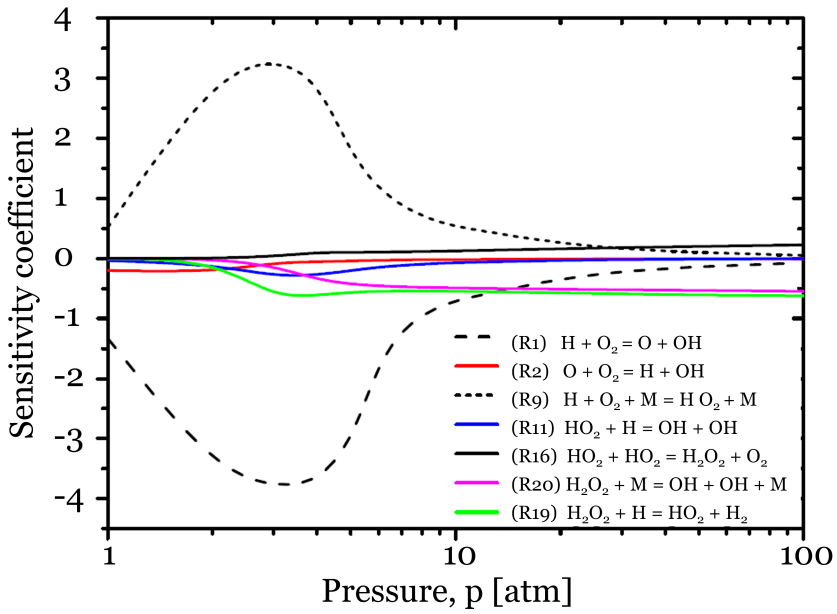

Figure 3.3: Sensitivity analysis of ignition time delays as a function of pressure at 1000 K for the Kéromnès et al. mechanism (mixture: $H_2/O_2/N_2/Ar = 1/1/1.88/1.88$). Only the seven most sensitive reactions are included, for clarity [55].

The constant rate of R36 is challenging to derive due to the difficulty of detecting HO_2 and H_2O_2, therefore, few experimental works exist around this reaction. Older mechanisms utilised the predictions of Hippler et al. [61] and Kappel et al. [62] until Hong et al. [69] introduced a dual-Arrhenius expression to fit the rate constant to their experimental results and predictions. This last expression is currently used in more recent models [59].

The recombination reaction R27 is used in older mechanisms and their revisions [55, 56, 60, 65, 70, 71]. However in more recent mechanisms [51, 58, 59, 66] the water decomposition path is employed, taking into consideration more recent experimental works. This

reaction is essential for flow reactor predictions in Mueller et al. [53] and has a high sensitivity to flame speeds under high-pressure conditions [60]. The increase in the rate constant leads to a decrease in reactivity. Furthermore, a comparison of high-pressure and low-pressure predictions yields negligible differences, and just a low-pressure description could be used [55].

3.2.2.1 Neglectable Reactions

In several updated mechanisms, specific reactions previously considered significant are excluded, as more recent experimental and theoretical investigations suggest they are less likely to occur under the relevant conditions. That is the case with R40. Jachimowski [47] included this reaction in his mechanism. However, Oldenborg [72] later proves that the collision of H_2 and O_2 leading to the formation of two molecules of OH is unlikely to happen, and the reaction can be neglected from the model. This was supported later by the potential energy surface studies of Michael et al. [73]. Wilson and MacComack [74] use this knowledge when building their kinetic mechanism and omit R40 from the list of reactions, like most of the recent kinetic mechanisms. Curiously, Konnov [58] employs this reaction. However, the author justifies this choice by stating that the attempt is to block the inclusion of outdated values for this reaction in the revised version of his model.

On the other hand, some reactions can be neglected due to the very low reactivity they present in the overall mechanism. Burke et al. [51] study the impact of some of these reactions in their model, such as R41, R40, R42, R43 but predictions did not yield significantly different results due to the inclusion of these reactions. Additionally, the authors argue that R34 should not be included in the mechanism list of reactions due to the lack of experimental data that exists to validate the reaction rate constant, though the inclusion produced substantial differences in the predictions of lean high-pressure flame burning speed, when using the highest proposed rate constant, which is supported by Hong et al. [59]. Shimizu et al. [60] included this reaction, using a reaction rate constant independent of pressure for the low-pressure limit, as a result of the very high fall-out pressure (much higher than 101325 MPa at 500 K). Furthermore, R34 competes with the reverse R20. However, the latter dominates the low-pressure regime [60].

3.2.3 Consumption Path

Hashemi et al. [52] analysed the consumption path in flow reactors and shock tubes. For the flow reactor, a broad range of equivalence ratios (0.0009 - 11.9) was studied at a constant pressure of 50 bar and a temperature range of 700-900 K. The authors found that, independently of stoichiometry, the consumption paths are generally similar. Hydrogen is mainly consumed by R22, and the H resulting from the reaction recombines with O_2 through R28. The HO_2 resulting from the self-recombination reaction through R35 to

form H_2O_2, which will thermally dissociate via R39 to form OH radicals required for the initial chain-branching R22. R38b will be important in the initiation process, but only under fuel-rich conditions where it consumes a considerable amount of H. After ignition, its importance vanishes.

For the shock tubes, the pathway analysis was performed at pressures of 2, 5, 10, and 40 atm, with an initial temperature of 1100 K. Additionally, the study was conducted for a time equivalent to 0.01% of hydrogen consumption. The reaction path in this case is different from the previously analysed one. The first step in the hydrogen consumption is identical to the flow reactor, although competition between R22 and R21 is now present. Furthermore, R20 overcomes R28 at low pressures, and the consumption of H is done through this dominant reaction. The HO_2 is then consumed by R30 to form two OH radicals. Conversely, at higher pressures, a more similar path to the flow reactor occurs. R28 will dominate, the H_2 consumption will proceed through this reaction. The HO_2 is then consumed via R30 for lower pressure conditions or through R38 and then R39.

Sensitivity analyses for the flow reactor conditions in [52] (700 - 800 K, 50 bar) showed that the rate-controlling reactions are R38, R39, and R35, respectively. The consumption is promoted by R38 and R39 and inhibited by R35, and therefore, the competition between R38 and R35 is very important. At stoichiometric conditions, R22 also becomes a major reaction. In this case, R38 continues to be the most sensitive since it promotes the initiation, but now R22 is the main responsible for the consumption of H_2. Finally, under oxidising conditions, R39 and R38 continue to be important, but now reactions involving oxygen become vital, and the competition of R20 and R28 is now present.

3.2.4 Kinetic Models with Transport

In kinetic mechanisms, the inclusion of transport effects is essential for simulating spatial phenomena, requiring the incorporation of these effects into the mathematical model. Both temporal and spatial components typically define the governing equations, and their solution involves partial differential equations (PDEs). However, when spatial effects are neglected, the problem simplifies to solving ordinary differential equations (ODEs). Incorporating transport effects into a kinetic model introduces additional complexities. Mathematically, the computational cost increases significantly for two primary reasons. First, a separate kinetic matrix is required for every spatial point, often amounting to dozens or hundreds of points in a given problem. Second, the kinetic equations at each spatial point are coupled through the influence of transport phenomena.

In addition to the computational challenges, transport models necessitate additional physical data, such as thermal and chemical species transport coefficients, which depend on the dominant mode of transport. For example, in laminar flames, transport mechanisms are well-defined but computationally expensive to resolve. Additionally, in turbulent flames, heat and mass transfer are governed by turbulence and cannot be precisely determined

[39].

Furthermore, transport models play a critical role in accurately capturing flame kinetic behaviour. For instance, hydrogen atoms generated in high-temperature regions of a flame diffuse rapidly due to their low molecular weight. A significant fraction of these atoms is not consumed in the high-temperature region but instead diffuses into cooler, unreacted areas, where they react with fuel and oxygen molecules. Consequently, these reactions are more prominent at lower temperatures in laminar flames than in flow reactors or shock tubes. If the transport model fails to accurately predict this diffusion behaviour, the kinetic behaviour of laminar flames may be misrepresented, compromising the overall model's predictions. Westbrook and Dryer [39] highlight general trends that are independent of specific transport modes: (1) molecular diffusion rates are inversely proportional to molecular weight, meaning lighter species (e.g., H, O, H_2, and OH) diffuse more rapidly than heavier ones; (2) transport coefficients increase with temperature and decrease with density.

Kéromnès et al. [55] evaluated various transport models in Chemkin Pro [75], including mixture-averaged, multi-component, and thermal diffusion options. Their results indicated that the multi-component approach is more accurate than the mixture-averaged alternative. Additionally, incorporating thermal diffusion into the multi-component model decreased flame speed predictions, with the effect being more pronounced for stoichiometric flames than for fuel-rich flames.

Similarly, Burke et al. [51] observed that the transport database developed by Wang et al. [76] provided the most accurate transport predictions. Nevertheless, the conventional Lennard-Jones parameters from the Sandia transport database [77] yielded comparable results, demonstrating the robustness of these parameters for kinetic modelling.

3.3 Available Kinetic Mechanisms

In 1937, at the time of the Second International Symposium on Combustion, the first breakthrough in the creation of a kinetic mechanism appeared. Kassel [78] presented a "mechanism for the combustion of hydrogen" composed by reactions R20, R21, R22, R28, and R38b. The author adequately explained the properties of ignition and high-pressure gas-phase reactions using this mechanism. In the subsequent years, several mechanisms were proposed, though it took Baulch et al. [79] another decade to present the first reliable rate constants for elementary reactions.

In 1980, Gardiner and Olson [80] presented a comprehensive review of experimental knowledge of reaction mechanisms up to that date, stating that all of the essential mechanism steps and rate expressions for the H_2/O_2 system were already known. Furthermore, they emphasised the need to determine chaperone efficiencies for various third bodies.

Due to the importance of the hydrogen-oxygen mechanism, several models became available in the '80s and '90s decades for different applications, namely the combustion of hydrocarbons – e.g., the moist carbon monoxide oxidation mechanism of Yetter et al. [49], which went through several revision and resulted in well-known mechanism like Ó Conaire et al. [56] and Li et al. [65]– and hydrogen-air combustion applied to ramjet and scram jet operation, e.g., Jachimowski [47] and Evans and Schexnayder [54] which considered the Spiegler et al. [46] as the base of the mechanism.

In the following subsection, some hydrogen-oxygen kinetic mechanisms will be compared to determine the most suitable one to implement in the combustion model. Due to the high number of available mechanisms, only more recent models (from the 2000s to the present day) were considered in this comparison. Some older models are presented due to the importance of the currently used mechanisms (e.g., Yetter et al. mechanism [49]) or due to this relevance to current applications (e.g., Jachimowski mechanism [47]).

Due to the broad range of pressures and temperatures in a rocket combustion chamber, a careful examination of different mechanisms is necessary to ensure that the selected model can yield accurate predictions within the considered range. Furthermore, a vast number of experimental results is needed to validate the model; therefore, a close review of the experimental data sets used by different authors to validate their models is also performed. In the majority of the revised mechanisms, the reactions are reversible. Therefore, if no information is given about the mechanism's reversibility, the reactions should be considered reversible.

Table 3.1 summarises the kinetic mechanisms that have been analysed. Note that in papers where the mechanism's temperature, pressure, and equivalence ratio range has not been explicitly mentioned, it is considered the experimental data range (temperature, pressure, and equivalence ratio) used to validate a given mechanism. Furthermore, as evident from the discussion below, not all mechanisms are designed exclusively for H_2-O_2 combustion. Instead, it is often a subset of a more comprehensive reaction mechanism. Consequently, in the table below, the numbers in parentheses indicate the number of species or reactions in the overall mechanism, where applicable, and the previous number is the number of species or reactions in the H_2-O_2 submechanism. It is also important to mention that the species in the list do not include the inert gases used as collision patterns in termolecular reactions, e.g., helium and argon. Nitrogen can sometimes be included in the number of species if the mechanism consists of the consumption or formation of thermal nitric oxides.

Table 3.1: Hydrogen-Oxygen Kinetic Mechanisms.

Mechanism	Source	Number of species	Number of reactions	Pressure range [MPa]	Temperature range [K]	Equivalence ratio range	Precedent	Observations
Jachimowski - 1988	[47]	8 (13)	20 (33)	0.05 - 0.7	298 - 1200	0.5 - 6	—	Supersonic combustion; Thermal NO_X subsystem
Modified Jachimowski - 1992	[74]	8 (13)	19 (32)	0.043 - 1.7	298 - 2300	—	[47]	Supersonic combustion; Thermal NO_X subsystem
Yetter - 1991	[49]	8 (11)	19 (28)	0.03 - 0.22	823 - 2870	0.0005 - 6	—	Wet CO oxidation
Kim - 1994	[81]	8 (11)	19 (28)	0.1 - 0.97	960 - 1200	0.33 - 2.1	[49]	CO oxidation
Muller - 1999	[53]	8	19	0.03 - 1.59	850 - 1040	0.33 - 1	[81]	
Li - 2004	[65]	8	19	0.03 - 8.8	298 - 3000	0.25 - 5	[53]	—
Ó Conaire - 2004	[56]	8	19	0.005 - 8.8	298 - 2700	0.2 - 6	[53]	—
Davis - 2005	[71]	8 (11)	20 (30)	0.03 - 8.8	298 - 2900	0.3 - 4.7	[82]	CO oxidation; Optimised mechanism
Konnov - 2008	[58]	8	21	0.03 - 8.8	298 - 2700	0.75 - 3	[83]	—
Hong - 2010	[59]	8	20	0.0048 - 6.5	298 - 2700	0.15 - 5	[82]	—
Shimizu - 2010	[60]	8	21	0.03 - 3.3	298 - 1850	0.3 - 5	[84]	—
Burke - 2011	[51]	8	19	0.0048 - 8.8	298 - 2900	0.15 - 5	[65]	—
Kéromnès - 2013	[55]	8 (11)	19 (31)	0.03 - 7.1	298 - 2900	0.1 - 6	[56]	CO oxidation
Vargas - 2015	[85]	11	31	0.015 - 8.8	296 - 2600	0.1 - 5.56	[55]	Optimised mechanism
Hashemi - 2015	[52]	8	19	0.1 - 8.8	298 - 1950	0.0009 - 12.07	[51]	—
Alekseev - 2015	[66]	8	20	0.00475 - 8.8	298 - 2700	0.1 - 7	[58]	—
Z22 - 2018	[50]	8	22	0.1 - 0.4	700 - 1300	0.2 - 5	—	—

3.3.1 Jachimowski Kinetic Mechanism

Jachimowski [47] created a chemical kinetic mechanism for the combustion of hydrogen and air, with 13 chemical species and 33 reactions. The initial mechanism has been refined using experimental data. In the mechanism, JANAF tables [86] are used for thermodynamic considerations. Jachimowski demonstrated that combustion models utilising nonequilibrium chemistry are preferable to those assuming equilibrium chemistry.

Later, some alterations were made to this model by Wilson and MacCormack [74] to improve the model pressure and temperature range for a ballistic application (over 17 atm and 2300 K). Firstly, reaction $H_2 + O_2 \longrightarrow OH + OH$ was removed due to the low probability of O_2 and H_2 collision for the formation of OH, as Oldenborg et al. [72] had predicted, and reaction $HO_2 + H \longrightarrow H_2 + O_2$ was omitted because it is the reverse of the new reaction RJ(1). Secondly, the reaction rates of RJ(2) and RJ(6) were revised due to the temperature and pressure conditions of the ballistic analysis. However, the results showed that the overall mechanism has a slight sensitivity to the change in the rate constant of RJ(6). Therefore, only the change in the rate constant of RJ(2) was applied in the revised mechanism. Furthermore, Wilson and MacCormack used Gardiner and Burcat [87] database to calculate NASA's polynomials. Gerlinger et al. [88] used this hydrogen/oxygen submechanism, which consists of 8 species (O_2, H_2, H_2O, OH, O, H, HO_2, and H_2O_2) and 19 reaction, excluding the nitrogen reactions. The mechanism can be seen in Table A.1.

3.3.2 Yetter Kinetic Mechanism

Yetter et al. [49] introduced a detailed mechanism for moist carbon monoxide combustion that include 11 species (H_2, O_2, O, H, OH, H_2O, HO_2, H_2O_2, CO, CO_2, and HCO) and comprises 28 reversible elementary reactions. The standard enthalpies of formation were taken from JANAF tables [86, 89], except for HO_2, which follows Hills and Howard [90]. Thermodynamic properties were calculated using NASA polynomial coefficients [37] from Kee et al. [91], except for HO_2 coefficients obtained from the THERM code by Ritter and Bozzelli [92]. To ensure consistency across recombination and dissociation reactions, the mechanism assumes uniform third-body efficiencies, varying only among individual species to account for their specific interactions.

Results from sensitivity and reaction flux analyses show that reactions RY(1), RY(2), RY(3), RY(4), RY(9), and RY(22), and to some extend reactions RY(14), RY(15), RY(20), RY(10), RY(11), RY(21), RY(16), and RY(19) have an preponderant influence in the overall mechanism. Therefore, to improve the model, it is necessary to improve the rate constant, equilibrium constants, and efficiency factor of these reactions. Furthermore, the authors note that further attention needs to be paid to reactions involving HO_2 and H_2O_2, especially in high-pressure and flame environments. Table A.2 shows the hydrogen/oxygen submechanism used.

3.3.3 Li Kinetic Mechanism

Li et al. [65], similarly to Ó Conaire et al. [56], updated the mechanism published by Mueller et al. [53], using recently published thermodynamic parameters and revised reaction rate constants. The mechanism is composed of 8 chemical species (H_2, O_2, O, H, OH, H_2O, HO_2, H_2O_2) and 19 reversible reactions. It can be observed in Table A.3. The mechanism has validated for a broader temperature and pressure range compared to the Ó Conaire et al. mechanism [56]. The authors, similar to Ó Conaire et al., retained the thermodynamic database from Mueller et al., which is based on Kee et al.'s Chemkin thermodynamic database [91]. However, the heat of formation for OH was obtained from Ruscic et al. [93] instead of using the value from Kee et al..

3.3.4 Ó Conaire Kinetic Mechanism

Ó Conaire et al. [56] mechanism updated the mechanism presented by Mueller et al. [53], which is a revised model of Kim et al. [81], which is itself a revision of the comprehensive Yetter et al. mechanism [49]. Motivated by the Smith [94] critique of the lack of precisions in existing mechanisms, the authors modified the mechanism proposed by Mueller et al. [53] to fit a broader range of experimental conditions, such as ignition delay in shock waves, atmospheric flame speeds, high-pressure flame speeds, burner-stabilised flame, and flow reactors. The initial model was only validated with flow reactor data over a temperature range 850 to 1040 K, at equivalence ratios of 0.3 to 1.0, pressures of 0.0304 to 1.59 MPa and residence time of 0.004 to 1.5 s. In contrast, the new mechanism was validated over a temperature range of 298 to 2700 K, a pressure range of 0.05 to 87 atm, and an equivalence ratio range of 0.2 to 6.

The mechanism is composed of 8 species (H_2, O_2, O, H, OH, H_2O, HO_2, H_2O_2) and 19 reversible elementary reactions presented in Table A.4. The reverse rate constants were computed by microscopic reversibility and using thermodynamic properties from Chemkin thermodynamic database [91] with two modifications: reference enthalpy of formation of HO_2, using the recommended value of Hills and Howard [90], and the reference enthalpy of formation of OH, based on the recommendations of Ruscic et al. [93] and Herbon et al. [95]. The transport parameters are from the Chemkin database without modifications. The modifications made to the original mechanism primarily affect reactions RO(8), RO(9), and RO(17).

Compared to the mechanism proposed by Davis et al. [96], the mechanism developed by Ó Conaire et al. [56] shows better agreement with shock tube data from Slack [97], as well as with laminar flame speed measurements of H_2/O_2/He mixtures at high pressure reported by Tse et al. [98], where the Davis mechanism tends to overpredict the results. When compared to the hydrogen and oxygen submechanisms of GRI-Mech 3.0 [82], Konnov [99], and Leeds [100], the Ó Conaire et al. mechanism [56] demonstrates greater consistency,

although its predictive accuracy may vary depending on the specific case. For ignition delay times, the current mechanism shows the best overall performance, as well as for laminar flame speeds at atmospheric pressure. Furthermore, the Ó Conaire et al. [56] and Mueller et al. [53] mechanisms are the only ones capable of accurately describing flow reactor data.

3.3.5 Davis Kinetic Mechanism

Davis et al. [71] developed an optimised kinetic mechanism for H_2-CO combustion. The initial, unoptimised mechanism consisted of 11 species (H_2, O_2, O, H, OH, H_2O, HO_2, H_2O_2, CO, CO_2, and HCO) and 30 reactions, with most rate constants derived from the GRI-Mech 3.0 [82] mechanism. The authors selected 36 experimental datasets as optimisation targets, categorising them into four groups: (1) flame speeds [98, 101–106]; (2) peak mole fractions of H and O in low-pressure burner-stabilised flames [107]; (3) consumption rates of H_2 and CO in turbulent flow reactors [53, 81]; and (4) ignition delay times [108–111].

Through sensitivity analysis of ignition delay times and fuel consumption rates in flow reactors, 24 pre-exponential factors and 7 third-body collision efficiencies were identified as the optimisation parameters. The optimisation algorithm used in the study is described in detail in [71]. Comparisons between the trial mechanism and experimental data demonstrated good agreement, with notable exceptions in some instances, including H_2/O_2/He flame speeds at elevated pressures, H and O mole fractions in burner-stabilised flames, and H_2 consumption in the 1.0% H_2/1.5% O_2/N_2 flow reactor mixture at 943 K and 2.5 atm—the optimisation process aimed to refine these predictions.

For validation, the optimised mechanism was tested against several of the target experimental datasets, along with additional studies. Of the 28 active parameters (some incorporating two pre-exponential factors), 12 reached their respective uncertainty boundaries (significantly fewer than what is typically encountered in kinetic mechanism optimisation). Parameters that did not reach their targets may have been inadequately constrained due to a lack of relevant experimental data or their limited influence on H_2/CO combustion, such as the third-body efficiencies for O_2 and H_2 in reaction H + O_2 + M $\longrightarrow$ HO_2 + M. Overall, the optimised mechanism exhibited excellent agreement with experimental data, demonstrating its improved predictive capability.

3.3.6 Konnov Kinetic Mechanism

Konnov mechanism [58] is composed of 8 species and 21 reversible reactions, illustrated in Table A.5. The reverse rate constant is calculated from the forward rate constant using Chemkin [112] chemical interpreter code and the thermodynamic data from the Burcat and Ruscic thermodynamic database [113]. Additionally, it used the transport properties

from Sandia National Laboratories [112]. The developed mechanism is based on previous works of Konnov [83, 99]

The author selected the mechanisms developed by Ó Conaire et al. [56] and Li et al. [65] to compare to the designed mechanism. Overall, the present model yields similar predictions to the selected mechanisms at high temperatures and within the studied pressure range (0.0304 - 8.815 MPa). However, at higher pressures, the case is not the same.

For ignition delay times, both the Konnov and Ó Conaire et al. [56] mechanisms provide accurate predictions for the ignition delay times reported in [97, 114]. In contrast, the Li et al. [65] mechanism overpredicts the data below 1000 K. Overall, the three mechanisms demonstrate good agreement with experimental data, with some deviations observed at high pressures and low temperatures. The author highlights the need for new experimental data further to validate the mechanism in the intermediate temperature range.

In the flow reactor data, the Konnov mechanism showed a significant underprediction compared to the experimental data. In contrast, the mechanisms of Ó Conaire et al. [56] and Li et al. [65] accurately captured the H_2 oxidation rate with excellent agreement. The observed discrepancies were attributed to reaction RK(14), which plays a dual role—acting as an initiation process at high temperatures and a termination process at intermediate and low temperatures. A lower rate constant for this reaction could improve agreement, but it would also lead to shorter ignition delay times.

Overall, the mechanism showed a strong agreement with experimental data for laminar flame velocity, except for some data ([115, 116]), which the author attributes to the lower experimental values, particularly for fuel-rich flames at low pressures, rather than an inaccuracy in the mechanism itself. Compared with Ó Conaire et al. [56] and Li et al. [65] mechanisms, Konnov's mechanism yields the most accurate predictions for high flame speeds.

The mechanism was further evaluated against the flame structure data from [117], showing good overall agreement. However, the computed profiles were steeper than those obtained experimentally. This discrepancy may be due to spatial averaging in the experimental measurements or the use of ideal gas calculations instead of real gas considerations.

3.3.7 Hong Kinetic Mechanism

The Hong et al. [59] mechanism consists of 8 species and 20 reactions, identical to the H_2-O_2 subsystem in GRI-Mech 3.0 [82]. However, it retains only five reaction rate constants (RH(6), RH(8), RH(10), RH(15), and RH(16)) from GRI-Mech 3.0, and adopting the rate constants recommended by Baulch et al. [118] for reactions RH(9), RH(10), RH(12), RH(14), RH(16), and RH(17). Additionally, it employs the thermodynamic database from Burcat and Ruscic [113]. The whole mechanism is presented in Table A.6.

The proposed mechanism was compared against four other mechanisms (O'Conaire et al. [56], Li et al. [65], Konnov [58], and GRI-Mech 3.0 [82]) using an extensive set of experimental data.

Since ignition delay times in shock tube experiments can be influenced by impurities, as demonstrated in [119], the authors focused on H_2O and OH profiles from Hong et al. [63, 69, 119, 120] for model validation. At 1472 K, the H_2O profile from [119] showed excellent agreement with all mechanisms except for the Ó Conaire et al. model. However, at 1100 K, only the Hong et al. mechanism and GRI-Mech 3.0 [82] accurately matched the experimental data. Using OH profiles from Masten et al. [120] at high temperatures (1980 K), only the Hong et al. and Konnov [58] mechanisms aligned well with experimental results. For H_2O and OH time-histories at 1192 K and 1398 K from Hong et al. [69], the Hong et al. mechanism demonstrated the best performance among all models. Finally, for the experimental data from Hong et al. [63], the mechanisms by Li et al. [65], Ó Conaire et al. [56], and Hong et al. showed similar predictions, all in good agreement with experimental results. The observed disparities in model predictions for [69] were attributed to the use of a higher rate constant for reaction RH(4).

For the experimental shock tube delay times and flow reactor species histories, the mechanism showed good agreement. As for the laminar flame speed experimental data, the Hong mechanism should be in overall good agreement except in some cases ([102, 121, 122]). Compared to the data from Burke et al. [123], the model exhibited better agreement than previously referenced mechanisms. However, refining the rate constants for reactions involving HO_2 could further improve the fit.

For the burned-stabilised flame structure experimental data, the model shows excellent agreement with the data from [124], but some discrepancies when compared to [107] and [117], due to the radical quenching effects near the burner face. In agreement with Konnov et al. [58], the authors attribute the discrepancies to the spatial resolution limitations of the experimental probe.

3.3.8 Shimizu Kinetic Mechanism

Shimizu et al. [60] developed a detailed kinetic model for H_2-O_2 combustion, specifically tailored for liquid rocket engine (LRE) conditions (high pressure). This mechanism updates the earlier work of Kitano et al. [84] and consists of 8 species (H_2, O_2, H_2O, H, O, OH, HO_2, and H_2O_2) along with 21 elementary reactions and represented in Table A.7.

The authors were motivated by the scarcity of kinetic mechanisms dedicated to high-pressure applications, such as LRE propulsion systems, where combustion chamber pressures can reach up to 200 atm—significantly higher than those found in internal combustion engines or gas turbines. Additionally, existing models often emphasise the role of bath gases, whereas LREs typically operate without diluents, making it challenging to de-

velop a kinetic mechanism applicable to these systems. Burke et al. [123] even suggested that several rate constants in current hydrogen combustion models may need modification to predict high-pressure flame properties accurately. Furthermore, they highlighted the possibility that key elementary reactions may still be missing from existing hydrogen combustion mechanisms.

Considering the ignition delay times, the mechanism aligns well with other established models (Li et al. [65], O'Conaire et al. [56], and Konnov [58]), especially for temperatures above the second explosion limit (approximately 1150 K).

For the experimental data of Burke et al. [123] at ϕ = 2.5 for laminar flame speeds, the mechanisms by Konnov [58], Davis et al. [71], and the present model provide the best agreement for pressures between 1 and 17.5 atm. However, beyond this pressure, none of the models accurately predict the mass burning rate. Sensitivity analysis under these conditions highlights the critical role of reactions RS(5) and RS(6) in determining mass burning rates between 10 and 50 atm. At the same time, RS(11), RS(12), and RS(20) become more influential at higher pressures.

3.3.9 Burke Kinetic Mechanism

Burke et al. [51] refined the model developed by Li et al. [65] by integrating updated rate constant data and kinetic models for diluted, high-pressure flames while retaining the thermodynamic database from the original model. Their results demonstrated that, at high pressures and low temperatures, uncertainties in the temperature- and pressure-dependent reactions governing HO_2 formation and consumption can significantly impact a mechanism's predictive accuracy. Additionally, the study re-evaluated several assumptions that had been previously overlooked, such as the pressure dependence of RB(1), the temperature dependence of the H + HO_2 reaction channels, the significance of the O + OH + M $\longrightarrow$ HO_2 + M reaction, and the application of non-linear bath-gas mixture rules for RB(9) in multicomponent bath gases. The mechanism consists of 8 species and 19 reversible reactions, as detailed in Table A.8. The authors also provide a list of excluded reactions, offering additional insights into the hydrogen oxidation mechanism.

The authors point to considerable uncertainties in flame speed and burning rate measurements. In some cases, discrepancies spanning several orders of magnitude were found even within datasets from the same research groups using similar methods and equipment. To account for these inconsistencies, a 20% margin was adopted when validating numerical predictions against experimental data. Burke et al., supported by later studies [125], also underscored the difficulty of obtaining reliable shock tube data due to contamination from trace impurities. Despite thorough cleaning and vacuuming to 10^{-7} Torr between tests, as noted by Hong et al. [63], contamination remains a persistent challenge affecting measurement accuracy.

The results show that the current model generally aligns with the findings of Li et al. [65], often offering improved predictive accuracy. Notably, it enhances ignition delay and species concentration predictions for $H_2O_2/H_2O/O_2$ mixtures. In terms of flame velocities, the model not only replicates Li et al.'s data but also significantly improves high-pressure burning rate predictions. When compared with the Hong et al. mechanism [59], both models yield similarly strong agreement with experimental data. However, the Burke et al. model stands out at elevated pressures and in highly diluted mixtures, where it better captures flame speed behaviour.

3.3.10 Kéromnès Kinetic Mechanism

The mechanism proposed by Kéromnès et al. [55] is suitably conceived for investigating the oxidation of a syngas mixture consisting of $H_2/CO/O_2/N_2/Ar$ at pressures from 1 to 70 atm, over a temperature range from 900 to 2550 K and equivalence ratios from 0.1 to 4. The kinetic mechanism involves 11 chemical species (H_2, O_2, H_2O, H, O, OH, HO_2, H_2O_2, CO, CO_2 and HCO) interacting among them through 31 reversible reactions, presented in Table A.9. The hydrogen-oxygen submechanism is an updated version of the Ó Conaire et al. mechanism [56], refined using experimental data from Mittal et al. [126] to evaluate the effects of modifications to the rate constants of reactions RK(1), RK(17), RK(9), RK(15), and other enhancements to the overall model. To accurately predict the ignition delay times measured in the shock tubes, an OH^* submechanism has been added. As for the thermodynamic properties, authors use Chemkin thermodynamic database [75] with two modifications: reference enthalpy of formation of HO_2, using the recommended value of Burcat and Ruscic [113], and the reference enthalpy of formation of OH, based on the recommendations of Ruscic et al. [93] and Herbon et al. [95]. The transport parameters are from the Chemkin database [75] without modifications.

Comparing the mechanism with other models for $H_2/CO/O_2$ combustion (Li et al. [57], Davis et al. [71], and USC Mech II [76]) and H_2/O_2 combustion (Burke et al. [51] and Hong et al. [59]) the present model offered improved predictions in some cases. This happens especially in low to intermediate temperatures where the mechanism captures the oxidation pathway through heavier elements (HO_2 and H_2O_2).

The inclusion of gas-dynamic effects in the Kéromnès mechanism influenced its accuracy in predicting ignition delay times [55], particularly when compared to models without this feature. A notable disparity between the mechanisms emerged when analysing jet-stirred reactor data from [127], specifically under two distinct mixture conditions: (1) a dilute mixture in N_2 at 1 atm with $\phi = 2.0$ and H_2 concentration of approximately 1%, and (2) a similar mixture with the addition of 10% H_2O.

3.3.11 Varga Kinetic Mechanism

Varga et al. [85] updated the mechanism developed by Kéromnès et al. [55] by employing an optimisation algorithm through experimental data. This process involved 1149 indirect measurements and 1749 direct measurements. The indirect measurements included a broad set of experimental data, such as ignition delay times (measured in shock tubes and rapid compression machines) and flame velocities, collected over a temperature range of 800 to 2300 K, a pressure range of 0.1 to 65 bar, and equivalence ratio between 0.2 and 5.0. In contrast, the direct measurements consisted of rate coefficients for key reaction steps.

In total, 33 rate parameters were optimised, including 30 Arrhenius parameters and 3 third-body efficiencies for 11 reactions — RK(1), RK(2), RK(3), RK(8), RK(9), RK(10)b, RK(11), RK(13), RK(14), RK(15)b, and RK(17). New uncertainty limits were also established for the Arrhenius values, leading to more precise uncertainty bands. These reactions and third-body efficiencies were selected based on sensitivity analyses. Furthermore, reactions RK(4), RK(5), RK(10), and RK(15) were used in the reverse path in the optimised mechanism, differing from the approach in Kéromnès et al. [55]. The third-body collision efficiencies for RK(9) involving Ar, H_2, and H_2O were also adjusted. The optimised values and reverse reactions for the Varga et al. mechanism are presented in Table A.10), with the remaining Arrhenius parameters following the values from Kéromnès et al. mechanism (see Table A.9). Notably, the rate constants that underwent the most significant changes were for reactions RK(15), RK(13), and RK(18), all of which involve HO_2, highlighting the increased focus on determining accurate Arrhenius values for these reactions.

When compared to other recent hydrogen-oxygen mechanisms ([51, 55–59, 70, 71, 128]), the current mechanism provides the best overall results across all experimental data. However, when considering specific datasets, certain mechanisms perform better in individual cases. For flame velocity predictions, Burke et al. [51] offers a better fit to experimental results, while for flow reactor measurements, the GRI-Mech 3.0 [82] model demonstrates superior accuracy.

3.3.12 Hashemi Kinetic Mechanism

Hashemi et al. [52] updated the mechanism proposed by Burke et al. [51], revising the rate constants for reactions RHA(4), RHA(13), and RHA(14). The revised mechanism retains the same structure as the original, with 8 species and 19 reactions.

The mechanism was compared to the Burke et al. [51] model under four equivalence ratio conditions, all at 50 bar: (1) 11.9, (2) 1.03, (3) 0.05, and (4) 0.0009. Both mechanisms showed good agreement with experimental data for the first two conditions, though the Hashemi model exhibited slightly faster fuel consumption in the stoichiometric case, re-

maining within experimental uncertainty. For the latter two cases, the Hashemi model demonstrated improved predictions, particularly for condition (3), where it closely matched experimental data. However, both models struggled to accurately predict combustion rates above 800 K in the oxygen-rich atmosphere (condition 4).

For RCM experiments [129], the Hashemi mechanism performed well, showing excellent agreement for lean mixtures ($\phi = 0.5$) and excellent agreement for stoichiometric mixtures ($\phi = 1.0$) under varying pressures. When the pressure was held constant and temperature varied, the mechanism's predictions closely aligned with experimental data.

Shock tube data revealed that the Hashemi model overestimates ignition delay times at low temperatures and high pressures for Herzler and Naumann's experiments [130], likely due to the use of a constant-u-and-v model used in the experimental dataset. However, as temperature increases, the model's accuracy improves.

Comparison with Kéromnès et al. [55] data show better agreement, particularly at higher temperatures, likely due to the change in bath gas from argon to nitrogen, which resulted in longer ignition delay times.

3.3.13 Alekseev Kinetic Mechanism

Alekseev et al. [66] updated the kinetic mechanism proposed by Konnov [58] by comparing its rate constants with those from more recent mechanisms, including Kéromnès et al. [55], Hong et al. [59], Burke et al. [51], and Shimizu et al. [60]. These models share a similar list of reactions, ensuring consistency in their evaluation. Thermodynamic data were sourced from Goos et al. [131], and transport parameters were taken from Ivanov et al. [132]. The authors maintain reactions RA(1), RA(2), RA(3), RA(4), RA(7), RA(9), RA(16), and RA(19) form the original mechanism.

The revised mechanism was benchmarked against the original Konnov model and the Kéromnès et al. [55] model, the latter recognised as one of the most reliable kinetic mechanisms available [133]. The Alekseev et al. mechanism demonstrated improved predictions compared to the original mechanism and yielded results comparable to the Kéromnès et al. [55] mechanism. In many cases, the predictions from the Alekseev and Kéromnès models were indistinguishable.

3.3.14 Z22 Kinetic Mechanism

Z22 [50] is a detailed H_2-O_2 kinetic mechanism comprising 8 species and 22 irreversible elementary reactions depicted in Table A.11. It incorporates the H_2-O_2 submechanism from Larsson et al. [134], along with three fuel-consuming reactions previously introduced in [56, 66, 71]. Similar to other mechanisms designed for ramjet and scramjet operating conditions, Z22 is intended for use in the "crossover" region between the first and third

explosion limits of hydrogen-oxygen combustion.

The mechanism performance was compared with other mechanisms, including those by Alekseev et al. [66], Jachimowski [47], Davidenko et al. [135], and Marinov et al. [136].

In laminar flame velocity predictions, all models, except for Davidenko et al. [135], showed similar accuracy compared to each other and to the experimental data. However, the mechanism by Alekseev et al. [66] provided the best agreement with experimental results. For ignition delay times at 1 atm, all models performed similarly above 1000 K, but significant discrepancies emerged at lower temperatures. The mechanisms by Davidenko et al. [135] and Marinov et al. [136] failed to capture the increase in ignition delay time with decreasing temperature due to the absence of HO_2 and H_2O_2 chemistry. Conversely, the models by Jachimowski [47] and Alekseev et al. [66] overpredicted ignition delay times. At higher pressures (4 atm), discrepancies between models became even more pronounced. Notably, the Z22 mechanism was the only one to successfully predict ignition delay times at low temperatures, highlighting its improved applicability under these conditions. Additionally, adiabatic flame temperature calculations showed close agreement among all models across the entire stoichiometric range ($0.35 < \phi < 5$), with the most significant deviations occurring near the stoichiometric region.

3.3.15 Higher Hydrocarbon dedicated mechanisms

Several mechanisms have been built to model the combustion of higher hydrocarbons, as such [82, 128]. Although the analysis of these mechanisms is outside the scope of the present work, it is important to mention them because they highly depend on the accuracy of the H_2-O_2 subsystems to yield trustworthy results. Additionally, several of the analysed mechanisms utilise the submechanism of H_2-O_2 as a starting point for formulating their mechanisms.

The CRECK H_2-O_2 submechanism [137] was developed by the CREK Modelling Group of Politecnico di Milano for the inclusion in a broader kinetic mechanism for heavy fuels. The research group has published several papers on a revised version of the initial model, as well as other publications that expand the model [128, 138, 139]. All these publications are self-consistent, meaning they incorporate the previous submechanisms. The H_2-CO and C_1 - C_3 subsystems submechanism is presented in [128, 138, 140, 141] and for heavy fuels the works of Pelucchi et al. [142–144] were used. The complete model for hydrocarbons is the CRECK_2003_TOT_HT_LT_SOOT_NOX [145] which uses 621 species and 27829 reactions and is a mechanism for C_1-C_{16} at high and low temperature (HT+LT) and presence of soot and NO_x. More information is also available in [146].

AramcoMech 2.0 [55, 147–152] is a kinetic mechanism developed for the oxidation of C_0 - C_4 at the National University of Ireland - Galway. It uses the [55] H_2-O_2 submechanism and a vast collection of works (cite before) for the construction of the entire mechanism.

More information can be found in [153].

GRI-Mech 3.0 [82] was developed through contributions from the University of California at Berkeley, Stanford University, the University of Texas at Austin, and SRI International to construct a with 53 species and 325 for the reaction of C_1 - C_3. The H_2-O_2 submechanism is used to create several kinetic mechanisms through the update of rate constants or the inclusion of different reactions, as [59, 71].

Other mechanisms used to simulate the combustion of hydrocarbons can be mentioned like Leeds Mech [100], San Diego Mech [154], and USC Mech II [76].

3.3.16 Model comparison

Saccone et al. [155] compared seven kinetic mechanisms (Kéromnès et al. [55], GRI-Mech 3.0 [82], Z22 [50], CRECK [138], AramcoMech 2.0 [153], Jachimowski [47]) and one reduced mechanism derived from Jachimowski [47], which was no relevance for the present work. The authors used experimental results for ignition delay times from Craig [156] (1.02 atm and 2.04 atm and ϕ = 1.0), Wang et al. [157] (4.44 atm and ϕ = 0.42), Beer and McDonell [158] (5.8 atm and ϕ = 0.2), and Hu et al. [125] (4 atm and ϕ = 0.5) to compare the mechanisms. They found that for the revised experimental data, except Hu et al. work, the Z22 mechanism [50] had the best agreement. Whereas Kéromnès et al. [55] and CRECK [139], mechanisms showed satisfactory agreement only for high temperatures and low pressures. On the other hand, when using the data provided by Hu et al. [125], where argon was the bath and thermal diluent gas, CRECK [139], Kéromnès et al. [55] and AramcoMech 2.0 [153] schemes had a better agreement than Z22 [50] which exhibits a significant mismatch compared to the test measurements at the simulated low-temperature conditions. The ignition delay times calculated using GRI-Mech 3.0 [82] are always far from the experimental data.

Simultaneously, Saccone and Marini [159] analysed six kinetic mechanisms (O'Conaire et al. [56], Z22 [50], CRECK [139], GRI-Mech 3.0 [82], USC Mech II [76], AramcoMech 2.0 [153]) and compared them to three experimental databases: Herzler and Naumann [130] (4 bar and 16 bar at ϕ = 0.5), Petersen et al. [160] (13.3 atm and 32.9 atm at ϕ = 0.5), and Hu et al. [125] (4 atm, 10 atm and 16 atm at ϕ = 0.5). The authors found that the CRECK [139] mechanism exhibits the best agreement with experimental data in all operative envelopes. Furthermore, results show that the Z22 [50] mechanism can satisfactorily capture the non-linear ignition behaviour of hydrogen oxidation, especially at high pressure and low-to-intermediate temperatures below 1100 K. Additionally, except AramcoMech 2.0, all other mechanisms fail to predict the induction times with a bigger disagreement among computational calculations and experimental data.

At the same time, Saccone et al. [161] analysed three mechanisms (Kéromnès et al. [55], Z22 [50], and Jachimowski [47]) against the experimental data of Snyder et al. [114] (1 -

4.2 atm and $0.5 \leq \phi \geq 1$) and Z22 [50] was the most promising mechanism for the prediction of experimental data. The other two models yield good results only for the low-pressure and high-temperature regimes but cannot predict the crossover region, as well as the Z22 [50] mechanism.

Later, Saccone et al. [162] revisited the experimental results of Herzler and Naumann [130], Petersen et al. [160], and Hu et al. [125] to compared a set of kinetic mechanism namely Mueller et al. [53], Li et al. [65], O'Conaire et al. [56], CRECK [139], Kéromnès et al. [55], Z22 [50], GRI-Mech 3.0 [82], USC Mech II [76], and AramcoMech 2.0 [153]. Ignition delay times were calculated for a pressure range between 4 and 16 atm for three equivalence ratios: 0.5, 1, and 2 in strong argon-diluted environments. The evaluation showed that the CRECK [139] and Kéromnès et al. [55] are the most accurate models in predicting the experimental results. The Z22 [50] can make good predictions in some low-temperature conditions, confirming its ability to capture the crossover region reasonably. Laminar flame speeds from the experimental works of Tse et al. [98] (5 - 20 atm), Krejci et al. [163] (1 - 3 atm) and Aung et al. [116] (1 atm) were also compared to the numerical models at a constant temperature of 298 K. For atmospheric pressures all models can yield good agreement, with Z24 presenting the best agreement. Between 2 and 3 atm, all mechanisms yield similar results. For the 5 atm data, the Z24 mechanism was in excellent agreement with experimental results and almost superimposed on the data. Kéromnès et al. [55], CRECK [139], and Ó Conaire et al. [56] also yield a satisfactory agreement. Curiously, at higher pressures, Mueller et al. [53] mechanism is the only model capable of predicting the results, with significant disagreement for the rest of the mechanism. This large discrepancy in the Mueller et al. [53] predictions could be due to the high importance given to the HO_2 and H_2O_2 pathways in the model, which are crucial in high-pressure environments, like the ones in the Tse et al. [98] experimental results.

The discrepancies in the selection of the most suitable mechanism, as observed in the analyses by Saccone and colleagues [155, 159, 161, 162], may be attributed to the consideration or neglect of diluted environments. The mechanism proposed by Zettervall and Fureby [50] does not account for diluted conditions, particularly when argon is used as the bath gas. In contrast, the mechanisms developed by Kéromnès et al. [55] and CRECK [139] demonstrate superior performance under diluted environments.

The Kéromnès et al. [55] kinetic model was selected to be used in this work due to its scientific merit and operational advantages. The mechanism has been widely applied in the literature to describe hydrogen combustion and has emerged as a benchmark against which other models are compared and tested. Its broad use among other researchers contributes to its validity and enables a relevant comparison of the results obtained in this study with prior studies. A further robust advantage of the Kéromnès mechanism is its extensive documentation, comprising mechanistic reaction pathways, rate constants, and thermodynamic properties. Such detail significantly facilitates its incorporation into computational models and minimises the chances of implementation errors. In addition, the

mechanism bases its workings on the existing work of Mueller et al. [53], whose original H_2-O_2 mechanism has been thoroughly tested against experiment. Utilising this existing work as a starting point provides a solid testing platform for judging the accuracy of the current implementation. Having access to the original Mueller mechanism also provides a simple means of cross-validation, strengthening the results. Beyond these functional and scientific considerations, the platform developed through this thesis was also thought to be flexible. It is compatible with the implementation of other kinetic mechanisms with minimal modification, ensuring the tool remains useful for whatever future research needs arise. Therefore, while the Kéromnès mechanism was chosen based on its resilience, traceability, and simplicity, the platform remains suitable for implementing other mechanisms when necessary. This connection of a robust kinetic model with a capable simulation framework forms a solid foundation for H_2-O_2 combustion phenomenon investigation and explanation.

Chapter 4

The numerical model

Building upon the theoretical framework presented in Chapter 2, it is now essential to outline the numerical considerations that guide the construction of the computational program.

4.1 Simulation Environment and Assumptions

The developed program is designed to simulate zero-dimensional (0D) combustion within a perfectly mixed reactor operating under constant pressure and adiabatic conditions. Its modular architecture allows for future extensions, enabling adaptation to other combustion environments beyond the current configuration.

At present, the program supports only Arrhenius-type rate constants, excluding alternative parametrisations such as Chebyshev polynomials, and Linear Burke expressions. For pressure-dependent reactions, it incorporates both the Troe and Lindemann formulations to model the fall-off behaviour. The thermodynamic model is limited to the gas phase and does not account for non-ideal mixing effects. The equation of state is based on the ideal gas law, with no support for more complex models, such as the Peng–Robinson or Redlich–Kwong models.

Despite these limitations, the program offers flexibility in simulating systems under either constant-volume or constant-pressure conditions, providing a solid foundation for combustion analysis in simplified reactor configurations.

4.2 Governing Equations

Consider a control volume V (bidimensional or tridimensional) fixed in space relative to an inertia referential bound by a control surface A with $\vec{n}$ as a unit vector perpendicular to the surface in each point. It is possible to label $f(\vec{r}, t)$ as a generic variable which satisfies a conservation principle per volume unit and $F(t)$ the integration value of this variable in the control volume:

$$F(t) = \int_V f(\vec{r}, t) dV \quad (4.1)$$

Where $\vec{r}$ represents the position vector and t is the time.

The value for $F(t)$ can vary through time due to the advective and diffusive flux which crosses the control volume boundary. Let $\vec{\varphi}_f$ represent the flux of F that goes through the control volume boundary per volume unit and per surface unit. If F increases due to this flux, the flux will be positive, i.e. $\vec{\varphi}_f \cdot \vec{n} < 0$, and the flux will be negative if it decreases the value of F. On the other hand, the value of F can change due to its production or consumption inside the control volume. Therefore, it is possible to define s_f as the quantity of F produced by a unit of volume and time, considering that the production results in a positive sign and the consumption in a negative sign.

Is it now possible to write all the contributions for the change of $F(t)$ inside the control volume:

$$\int_V \frac{\partial f}{\partial t} dV = -\int_A \vec{\varphi}_f \cdot \vec{n} dA + \int_V s_f dV \quad (4.2)$$

Using the Gauss theorem and integrating the above expression, it is possible to rewrite it in the following form:

$$\frac{\partial f}{\partial t} + \nabla \cdot \vec{\varphi}_f = s_f \quad (4.3)$$

Through this equation, it is possible to derive all the conservation relations needed for the construction of the numerical model.

4.2.1 Species Mass Conservation

The species continuity or species mass conservation, similarly to the continuity equation, can be written considering f as the mass fraction of species i ($f = \rho y_i$), $\vec{\varphi}_f$ as the mass flux of the specie i ($\vec{\varphi}_f = \rho \vec{v}_i y_i$) and the source term as the production rate of the specie ($s_f = W_i \dot{\omega}_i$):

$$\frac{\partial(\rho y_i)}{\partial t} + \nabla \cdot (\rho \vec{v} y_i) = -\nabla \cdot \vec{j}_i + W_i \dot{\omega}_i \quad (4.4)$$

Where $\vec{j}_i$ is the diffusive flux of specie i defined as:

$$\vec{j}_i = \rho y_i \vec{V}_i \quad (4.5)$$

Where $\vec{\mathrm{V}}_i$ is the diffusive velocity of specie i. The diffusive flux can be divided into three main factors: ordinary diffusion (due to the concentration gradients), thermal diffusion (Soret effect), and pressure diffusion. In combustion, the diffusion due to the pressure gradient can be neglected, as well as the Soret effect [36]. Through some manipulation, and considering the diffusion due to the concentration gradient, is approximated by Fick's law of diffusion, it is possible to write the species continuity equation in the following

form:

$$\rho \frac{Dy_i}{Dt} = \nabla \cdot \left(\rho D_i^M \nabla y_i \right) + M_i \dot{\omega}_i \quad (4.6)$$

Where D_i^M is the mean diffusion coefficient calculated through:

$$D_i^M = \frac{1 - y_i}{\sum_{j=1}^{N} \frac{x_i}{D_{ij}}}, \text{where } j \neq i \quad (4.7)$$

Where D_{ij} is the binary diffusion coefficient.

4.2.2 Energy Conservation

The energy conservation equation can be derived when considering f as the total energy per unit of volume ($f = \rho e$), $\vec{\varphi}_f$ is composed of three terms: advective ($\rho e \vec{v}$), work done by pressure and viscose forces ($\overrightarrow{\overrightarrow{\sigma}} \cdot \vec{v}$), and heat ($\vec{j}_q$). The source term is related to the heat transmission due to radiation ($\dot{q}_R'''$):

$$\frac{\partial(\rho e)}{\partial t} + \nabla \cdot (\rho \vec{v} e) = \nabla \cdot \left(\overrightarrow{\overrightarrow{\sigma}} \cdot \vec{v} \right) - \nabla \cdot \vec{j}_q + \dot{q}_R''' \quad (4.8)$$

Where $\overrightarrow{\overrightarrow{\sigma}}$ is the total stress tensor, defined by:

$$\overrightarrow{\overrightarrow{\sigma}} = -p \overrightarrow{\overrightarrow{I}} + \overrightarrow{\overrightarrow{\tau}} \quad (4.9)$$

Where, p is the pressure, $\overrightarrow{\overrightarrow{I}}$ is the identity tensor, and $\overrightarrow{\overrightarrow{\tau}}$ is the viscous stress tensor.

The heat flux can be subdivided into three contributions: conductive heat flux ($\vec{j}_q^c$), governed by Fourier's law, which arises due to temperature gradients; Dufour heat flux ($\vec{j}_q^D$), which results from concentration gradients, and represents cross-effects between mass and heat transfer; and diffusive heat flux ($\vec{j}_q^d$)), associated with the transport of enthalpy due to mass diffusion.

The energy conservation equation can also be written with the temperature as the dependent variable:

$$\rho c_p \frac{DT}{Dt} = \frac{Dp}{Dt} + \nabla \cdot (\lambda \nabla T) - \sum_{i=1}^{N} c_{p,i} \vec{j}_i \cdot \nabla T - \sum_{i=1}^{N} h_i W_i \dot{\omega}_i + \overrightarrow{\overrightarrow{\tau}} : \nabla \vec{v} + \dot{q}_R''' \quad (4.10)$$

Where c_p is the specific heat capacity, λ is the thermal conductivity of the mixture, and h_i is the enthalpy, W_i is the molar mass, and $\dot{\omega}_i$ is the production rate of specie i. For this deduction it has considered that every chemical specie behaves accordingly to the ideal gas law, the Dufour effect is neglectable and the radiation is the only heat source.

Considering the same specific heat for all the species, the third term on the right-hand side of Equation 4.10 can be neglected. Furthermore, the fifth term in the equation is also commonly neglected, as noted by Coelho and Costa [36]. Additionally, the radiative heat source term ($\dot{q}_R'''$) can be excluded when soot formation is minimal, which is typically the case in combustion systems such as liquid rocket engines.

Considering these simplifications, the expression of the energy conservation, using the temperature as the dependent variable, can be rewritten as follows:

$$\rho\frac{DT}{Dt} = \frac{1}{c_p}\frac{Dp}{Dt} + \nabla\cdot\left(\frac{\lambda}{c_p}\nabla T\right) - \sum_{i=1}^{N}\frac{h_i W_i \dot{\omega}_i}{c_p} \quad (4.11)$$

4.3 Problem Formulation

Equation 2.65 defines the problem to be solved to determine the time evolution of each species' concentration. To facilitate the problem formulation, it is possible to rewrite the equation in a generic form:

$$\dot{\omega}_i = \frac{d\left[X_i\right]}{dt} = f_i\left(\left[X_1\right], \left[X_2\right], ..., \left[X_S\right]\right), \text{ where } i = 1, 2, ..., S \quad (4.12)$$

Where S is the number of species in the kinetic mechanism, it is crucial to note that the species' concentrations are a function of time.

Writing similar expressions for each species results in a system of ordinary differential equations (ODEs) comprising S equations and S variables. Typically, the temperature is also unknown, requiring the inclusion of the energy conservation equation in the system [36]. The complete ODE system, therefore, consists of S species mass conservation equations, along with the energy conservation equation, where temperature T is treated as the dependent variable.

As previously mentioned, the program simulates an isobaric and adiabatic flow reactor. Under this assumption, the system of ordinary differential equations (ODEs) can be simplified by considering uniform composition and temperature throughout the control volume. This implies the absence of species or temperature gradients and, therefore, no associated fluxes. Additionally, there is no heat or mass exchange with the reactor walls. Since the model assumes a single gas phase, interphase heat and mass transfer are also neglected. Finally, the gas phase is treated as ideal and incompressible. The resulting system of ODEs is composed of the following equations:

$$\dot{y}_s = \frac{\dot{\omega}_s W_s}{\rho} \quad (4.13)$$

$$\dot{T} = -\frac{1}{\bar{c}_p c} \sum_{s=1}^{S} \bar{h}_s \dot{\omega}_s \quad (4.14)$$

Where y_s is the mass fraction ($\dot{y}_s = dy_s/dt$), W_s is the molar mass, $\bar{h}_s$ is the enthalpy, and $\dot{\omega}_s$ is the production rate for each specie s, and T is the temperature, $\bar{c}_p$ is the specific heat capacity, ρ is the density, and c is the molar concentration of the mixture. A constant-pressure or constant-volume process is obtained by keeping either p or ρ constant, respectively. For a constant-volume process c_p and h_s should be replaced by c_v and u_s, respectively.

It is important to note that Equation 4.14 is expressed in terms of molar-based properties rather than the mass-based formulation initially presented. This change introduces minor modifications to the equation, including the addition of molar concentration.

The equations are closed by the ideal gas equation:

$$\rho = \frac{pW}{\mathcal{R}T} \quad (4.15)$$

Where p is the pressure, W is the molar mass, T is the temperature of the mixture, and $\mathcal{R}$ is the universal gas constant.

Since the ODE system is homogenous, it is sufficient to compute a solution to know the initial concentration and temperature. This type of problem has the name of "initial-value problem" (IVP) and can be abstractly represented, according to Cohen et al. [164], as:

$$\begin{cases} \dfrac{du}{dt} = f(t,u) \\ u(t_0) = u_0 \end{cases} \text{, where } y \in \mathbb{R}^N. \quad (4.16)$$

The problem can be written in a vector form, according to the notation of Stone and Bisetti [165]:

$$\begin{cases} \dot{u}(t) = f(u(t), q) \\ u(t = t_0) = \left[y_1(t_0), y_2(t_0), ..., y_S(t_0), T(t_0)\right]^T \end{cases} \quad (4.17)$$

Where $u(t)$ is the vector of unknowns at some time t, q is a set of non-integrated parameters (e.g., p or ρ), and t is the independent variable with initial conditions given by t_0. Note that the system is written in autonomous form, neglecting any dependence of f on t.

4.4 Ordinary Differential Equation Solver

In reactive systems, the presence of radicals leads to varying production rates among species. Radicals tend to react more rapidly than more stable species, resulting in different chemical time scales for each element. This disparity gives rise to a stiff system of ODE. To ensure numerical stability in such cases, implicit integration schemes are generally the most suitable approach [36].

Every numerical solver aims to advance the solution from $u(t)$ to $u(t+h)$, where h is the adaptive integration step size. Solvers are generally classified into two main categories: one-step and multistep methods. One-step methods compute the solution at t_{i+1} using only information from the previous point t_i. Although they may evaluate the function at intermediate points between t_i and t_{i+1}, this information is not retained for future steps. Each step is treated as a new, independent problem [165, 166].

Since numerical error tends to accumulate over successive steps, it becomes essential to incorporate more accurate historical data when estimating the solution at t_{i+1}. Methods that utilise multiple previous points to improve accuracy are known as multistep methods [166].

A multistep method can be written according to Radhakrishnan [167] as it follows:

$$u_n = \sum_{i=0}^{K_1} \alpha_{n,i} u_{n-i} + h_n \sum_{i=0}^{K_2} \beta_{n,i} f(u_{n-i}, q) \quad (4.18)$$

If the $\beta_{0,i} = 0$ the method is called explicit, and if $\beta_{0,i} \neq 0$ is implicit, because u_n occurs in both sides of Equation 4.18. Implicit methods are usually more expensive because to solve them, it is first necessary to solve the implicit equation for u_{i+1}, at least at the beginning of the calculations [166]. However, they are preferred to explicit methods since they are more stable and hence can use larger step lengths, and because they are more accurate for the same order and step size because they have smaller error coefficients [167]. An explicit method could be used as a "predictor", but usually, an implicit method is used to refine the solution, acting as a "corrector".

4.4.1 Multi-step implicit methods

From Equation 4.18 it is possible to retrieve different multistep methods like the Adams-Moulton (AM) methods, where $K_1 = 1$ and $K_2 = q - 1$, where q order varies between 1 and 12, or the backward differentiation formula (BDF) methods, considering $K_1 = q$ and $K_2 = 0$, with q varying between 1 and 5 [164]. The BDF methods provide much better stability than the AM methods and, therefore, are preferred to stiff problems [167].

In either case, the non-linear Equation 4.18 is solved iteratively. Defining the iteration

function as:

$$G(u_n) \equiv u_n - h\beta_0 f(u_n, q) - a_n = 0 \quad (4.19)$$

Where a_n is defined as:

$$a_n \equiv \sum_{i=0}^{K_1} \alpha_{n,i} u_{n-i} + h_n \sum_{i=0}^{K_2} \beta_{n,i} f(u_{n-i}, q) \quad (4.20)$$

Note that $\alpha_{n,0} = 1$ by notation. This method can sometimes be called "linear multistep methods" because u_i and $f(u_n, q)$ occur linearly [167].

In an implicit scheme, Equation 4.19 will be solved using an iteration technique, e.g., Newton-Raphson, Jacobi-Newton or functional iteration (where no matrices are involved). This last method, although simpler, converges only linearly and requires a small step size to converge successfully, becoming restrictive for stiff problems [167]. Conversely, the Newton-Raphson method converges quadratically and can be applied to larger sizes. For these reasons, this method is attractive to solve stiff problems [165]. Using it, the problem can be written in the following form:

$$\begin{aligned} \left[I - h\beta_0 J\left(u_n^{(i)}\right)\right] \delta u_n^{(i)} &= -G\left(u_n^{(i)}\right) \\ u_{n+1}^{(i+1)} &= u_n^{(i)} + \delta u_n^{(i)} \end{aligned} \quad (4.21)$$

Where I represents the identity matrix and J the Jacobian matrix of $u(t)$, defined by:

$$J(u(t)) = \begin{bmatrix} \frac{\partial u_1}{\partial y_1} & \frac{\partial u_1}{\partial y_2} & \cdots & \frac{\partial u_1}{\partial y_s} & \frac{\partial u_1}{\partial T} \\ \frac{\partial u_2}{\partial y_1} & \frac{\partial u_2}{\partial y_2} & \cdots & \frac{\partial u_2}{\partial y_s} & \frac{\partial u_2}{\partial T} \\ \vdots & \vdots & \vdots & \vdots & \vdots \\ \frac{\partial u_{s+1}}{\partial y_1} & \frac{\partial u_{s+1}}{\partial y_2} & \cdots & \frac{\partial u_{s+1}}{\partial y_s} & \frac{\partial u_{s+1}}{\partial T} \end{bmatrix} \quad (4.22)$$

An effortless simplification can be made without knowing the kinetic mechanism. In Equation 4.17, it is possible to see that only u_{s+1} will be temperature dependent. Therefore, all the terms in the top right column in the Jacobian matrix can be nullified except the last one. A similar logic can be applied to the last row in the matrix because u_{s+1} is exclusively temperature dependent:

$$J(u(t)) = \begin{bmatrix} \frac{\partial u_1}{\partial y_1} & \frac{\partial u_1}{\partial y_2} & \cdots & \frac{\partial u_1}{\partial y_s} & 0 \\ \frac{\partial u_2}{\partial y_1} & \frac{\partial u_2}{\partial y_2} & \cdots & \frac{\partial u_2}{\partial y_s} & 0 \\ \vdots & \vdots & \vdots & \vdots & 0 \\ 0 & 0 & 0 & 0 & \frac{\partial u_{s+1}}{\partial T} \end{bmatrix} \quad (4.23)$$

To solve the Equation system 4.21, it is possible to use a direct method, like Gauss elimination or LU factorisation. The use of a dense matrix based on ODE is the common approach to solving a detailed kinetic mechanism. For a small, detailed mechanism (containing fewer than 50 species), this approach is effective. However, with the increase in the number of species and reactions considered, the dense matrix approach could become a limiting factor in simulation run times. [168].

When using these methods to solve linear systems, much of the core memory required is used to store the coefficient matrix and its decomposition factors, which could be highly restrictive for large problems [169, 170]. Instead, the Krylov methods can be associated with the linear systems which arise at each time step. They do not require the storage of coefficients and decomposition factors and, therefore, reduce memory usage [169]. The work developed by Brown and Hindmarsh [171] developed a matrix-free method to solve stiff ODE systems and used the Incomplete Orthogonalised Method (IOM), which was coupled with Newton's method to solve the system in Equation 4.21. Later, Brown and Hindmarsh [169] and Brown et al. [170] used a preconditioned Krylov subspace (GMRES) to reduce the extensive memory usage in the direct methods for an ODE and a differential-algebraic equation (DAE) system, respectively. This approach requires the explicit use of a Jacobian matrix. This work aims to improve upon the previous study [171], in which the researchers concluded that including preconditioning in the linear iteration can be applied to a broader problem class.

Similarly, McNenly et al. [168] showed that the use of the GMRES methods used in the CVODE solver [164] could decrease the computation time compared to the classical approach using the EPISODE solver [172] and the CHEMKIN-PRO ODE solver. Results show that for smaller detailed mechanisms such as the Ó Conaire et al. [56] and the GRI-Mech 3.0 [82] for methane-oxygen combustion (contains 53 species), the classical methods have a faster computation. However, for larger mechanisms, e.g., the 7172 species for the combustion of 2-methylnonadecane, the preconditioned GMRES method has a clear superior advantage over the two other approaches (3125 and 14 times faster than the classical and the CHEMKIN-PRO approaches, respectively).

4.4.2 Available Solvers

The following subsection compares some of the available solvers for systems of ODE. The focus was on the well-known solvers developed by the Lawrence Livermore National Laboratory (LLNL), which are published under various packages and programming languages. They were preselected due to their easy availability and the extensive online documentation that facilitated the solver's implementation. Other combustion frameworks, like OpenSMOKE++ [173], also utilise these solvers, proving the packages' robustness and trustworthiness.

The LSODE (Livermore Solver for Ordinary Differential Equations) solver and its variant

the LSODI developed by Alan [174] were created to improve the existing solver GEAR [175] (and its variants GEARB and GEARIB). The solver enclosed both GEAR and GEARB packages, resulting in greater flexibility to user controls and options while facilitating the use and installation in a library environment [176].

The LSODE was the precursor of the ODEPACK, which is a collection of nine ODE solvers. The collection is composed of LSODE, LSODES, LSODA, LSODAR, LSODPK, LSODKR, LSODI, LSODIBT, and LSODIS, and as a vast range of usability: allows for stiff and non-stiff systems; problems in linearly implicit form (LSODI, LSOIBT, and LSODIS) instead of an explicit form; two of the solvers use general sparse matrix solvers (LSODES and LSODIS); two other use iterative methods instead of direct ones (LSODPK and LSODKR) [177]. The LSODI family is a variant of LSODE, which allowed the ODE systems to be presented in a linearly implicit form: A dy/dt = g(t,y), where A is a square matrix. The LSODA and the LSODAR are both able to automatically alternate between the Adams and BDF methods for nonstiff and stiff problems, respectively. This could be easier for a user to implement because they are not concerned with stiffness and is potentially more efficient than the LSODE when the solution changes between stiff and nonstiff [177]. Furthermore, the LSODAR is capable of finding the root of a function for the independent and dependent variables in the ODE system, which could be used for particle tracking problems to determine if the particle path reaches any of the walls of the container [177].

Simultaneously, the GEAR packages were transformed from a fixed-coefficient to a variable-coefficient BDF method. This was motivated by the inability of the GEAR package to handle specific chemical kinetic problems where the coefficient functions and solutions exhibit sharp and frequent time variations. This work resulted in two new solvers, the EPISODE and its variants, the EPISODEB [172] and the EPISODEIB, which allow a system with banded Jacobian matrices and problems in linearly implicit form with banded Jacobian matrices, respectively. This was done similarly to the GEAR package and variants (GEARB and GEARIB).

Later, Brown and co-workers [176] introduced the VODE package, which coupled the EPISODE and the EPISODEB solvers. Similarly to the LSODE package, VODE has a highly efficient user interface. However, it also offers variable-coefficient AM and BDF methods, which are more flexible for problems that require frequent and wide changes in step size. One variant of VODE is the VODPK [169], which, instead of applying a direct method to solve Equation 4.19, used a preconditioned Krylov method. This approach could enable faster computation, as seen previously.

A different approach was presented by Brown et al. [170] when considering a solver to compute DAE, the DASPK. The solver, similarly to the VODPK, used the Krylov subsystems approach but applied it to a DAE system. This solver is based on the integration methods in the previous solver DASSL [170].

All of the previously mentioned solvers were written in FORTRAN 77 and are available in

both single and double precision. It is possible to distinguish them by the prefix S or D for a single or double precision, respectively.

The CVODE solver [164] was the first effort to develop a new solver package. It was designed to combine the VODE and the VODPK solvers into a single solver. Simultaneously, it addressed some drawbacks that both solvers had related to differences in declarations and linear solvers. The solver allows for stiff and nonstiff systems and, in the case of stiff systems, the choice to use direct methods (full or banded) and the preconditioned GMRES method (Krylov method) [164].

The solver package referenced is the widely used SUNDIALS suite (SUite of Nonlinear and DIfferential/ALgebraic equation Solvers) [178, 179]. Developed in ANSI standard C, SUNDIALS was designed to overcome the limitations of FORTRAN 77 by enabling a more object-oriented structure, promoting code modularity and reuse, and facilitating the transition from serial to parallel implementations [178]. It contains six solvers: CVODE, CVODES, IDA, IDAS, ARKODE, and KINSOL. The CVODES is an extension of CVODE for conducting forward or adjoint sensitivity analysis of ODE IVPs for the parameters p in problems in a form:

$$\begin{cases} \frac{dy}{dt} = f(y, q, p) \\ y(t_0) = y_0(p) \end{cases} \quad \text{, where } p \in \mathbb{R}^{N_p}. \quad (4.24)$$

The same happens for IDA and IDAS. The precursor of IDA was the DASPK, which targets the more general case of DAE and implicit ODE systems. The ARKODE targets ODE problems in the linearly implicit form. Lastly, the KINSOL solves nonlinear systems in root-finding or fixed-point form.

4.4.3 Solvers Comparison

Cuoci et al. [173] compared several ODE solvers (CVODE, DASPK, DLSODA, DLSODE, DVODE, RADAU5, and a native solver) for several conditions. The first condition set comprises 18 cases of constant-volume, adiabatic batch reactors burning a mixture, considering four different kinetic mechanisms. The set finds all the combinations of two pressures: 2 and 20 bar; three temperatures: 750, 1000 and 1500 K; and three equivalence ratios: 0.5, 1 and 2. For a n-heptane and air mixture, results show that the CVODE solver gives the best solutions, followed by the DASPK. However, this last one is not as robust as the CVODE due to the incapacity to yield results for one of the kinetic mechanisms. The DVODE and DLSODE solvers followed the other two but were five times slower than the CVODE solver. The RADAUS5 (an implicit Runge-Kutta method of order 5) showed outstanding accuracy but had a relatively slow running time. The DLSODA solver gave the worst performance. For larger hydrocarbon kinetic mechanisms, specifically for the combustion of methyl-decanoate and air, the results are analogous to those in the pre-

vious cases. The last simulations used a diesel surrogate, showing similar results. Here, CVODE had the best performance, with a running time 20 times faster than that of the DSLODE and DVODE solvers. A simulation has also been conducted for a jet-stirred reactor, yielding results similar to those previously obtained.

Stone and Bisetti [165] compared different multistep and one-step ODE's for two different scenarios. The first is a 0D combustion simulation at atmospheric pressure, initial temperature of 1001 K, and with an initial mole fraction of $H_2/O_2/N_2$ = 2/1/4. The second using a 1D laminar premixed flame simulation. Both cases use the GRI-Mech 3.0 [82] methane-air submechanism with 53 species and 325 reactions. For the first set of conditions, the CVODE [164] showed to be the most efficient one for large step sizes. However, for smaller step sizes, fully implicit (FIRK) and singly diagonally implicit (SDIRK) Runge-Kutta methods were shown to have slightly better performance than the CVODE solver. For the second kinetic problem, one of the FIRK computations was faster than the CVODE for some of the analysed step sizes.

The combustion of hydrogen and oxygen is characterised by a small kinetic mechanism, especially when compared to heavy hydrocarbons, which can involve thousands of species and reactions. As shown by McNenly et al. [168], for a small kinetic mechanism, the use of a direct method for resolving a Newton method is quicker than a preconditioned Krylov method.

In the developed program, the CVODE solver from the SUNDIALS suite was used with a Krylov method. Because future applications such as methane combustion or skeletal n heptane with hydrogen will require a preconditioned Krylov subspace method like GMRES, this approach was adopted in the implementation. Additionally, since the program is built on the SUNDIALS framework, it is possible to implement alternative solvers without compromising the overall architecture.

4.5 Model Implementation

The resulting program can be divided into three segments: Kinetic Pre-Processor, Solver, and Graphical Post-Processor. The core sections (Kinetic Pre-Processor and Solver) are written in FORTRAN 90, in conformity to the existing AEROG research group programs. Figure 4.1 illustrates how the different inputs for each segment as well as the program's workflow.

The program operates with SI units, and therefore, the universal gas constant has a value of 8.314462618 J mol^{-1} K^{-1}.

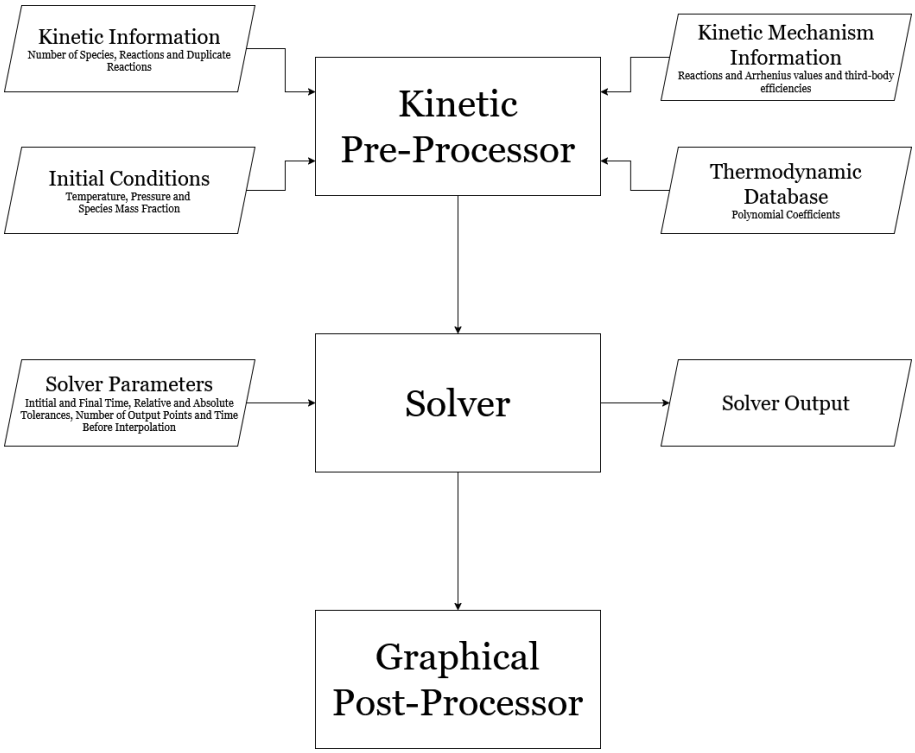

Figure 4.1: Program's Flowchart.

4.5.1 Kinetic Pre-Processor

The first segment, the Kinetic Pre-Processor, is responsible for reading the necessary input files and calculating the variables in Equations 4.13 and 4.14. This process is composed of seven modules:

1. *m_constants*;
2. *m_forward_rate_constant*;
3. *m_mixing_model*;
4. *m_reverse_rate_constant*;
5. *m_store_data*;
6. *m_thermodynamic_properties*;
7. *m_third_body_concentration*.

The first module, *m_constants* module, stores relevant physical constants, such as the universal gas constant and the reference pressure.

The *m_store_data* module reads all input data files, including kinetic information (such as the number of species, reactions, and duplicated reactions), initial conditions (pressure, temperature, and species mass fractions), and the reaction data (stoichiometric co-

efficients) with corresponding Arrhenius parameters for the selected kinetic mechanism. If necessary, it also converts the pre-exponential factor A and the activation energy E_a (in Equation 2.59) to SI units.

The *m_thermodynamic_properties* module provides functions to calculate thermodynamic properties, including specific heat capacity at constant pressure, enthalpy, and Gibbs free energy. These properties are computed using NASA's 7-term polynomials, developed by Gordon and McBride [37]. The polynomial coefficients were obtained from the Burcat and Ruscic database [113], except for those of OH^*, for which the values reported by Kéromnès et al. [55] were used.

The *m_forward_rate_constant* and *m_reverse_rate_constant* modules compute the values of $k_{f,r}$, through Equation 2.59 and $k_{b,r}$, through Equation 2.70, respectively. The *m_third_body_concentration* module calculates the third-body concentration for each reaction, through Equation 2.53, and returns the corresponding value used in the computation of $k_{f,r}$ for pressure-dependent reactions. This value is also passed to the module responsible for setting up the ODE system.

Lastly, the *m_mixing_model* module enables the calculation of mixture properties, such as heat capacity at constant pressure, and molar mass, using an molar-weight model, defined by:

$$\bar{c}_{p,mix} = \sum_{s=1}^{S} \bar{c}_{p,s} x_s \quad (4.25)$$

$$W_{mix} = \frac{1}{\sum_{s=1}^{S} \frac{x_s}{W_s}} \quad (4.26)$$

Where $\bar{c}_{p,mix}$, and W_{mix} are the molar specific heat capacity at constant pressure, and the molar mass for the mixture, and $\bar{c}_{p,s}$, the molar specific heat capacity at constant pressure, W_s, the molar mass, and x_s mole fraction for species s.

4.5.2 Solver

The Solver uses the SUNDIALS suite, namely the CVODE solver, to compute the ODE solution.

The process is composed of four modules:

1. *m_jacobian_auxiliary*;
2. *m_print_output*;
3. *m_solver*;

4. *m_solver_setup*.

The *m_solver_setup* module is responsible for generating the right-hand side of Equations 4.13 and 4.14. Within this module, the mixture's thermodynamic properties, such as molar weight, density, and specific heat capacity, are calculated. Additionally, it computes the rate-of-progress variable rate (q_r), the species production rate ($\dot{\omega}$), through Equations 2.64 and 2.61, respectively. Additionally, it sets the root finder function, if desired, and the Jacobian matrix to be used by the solver to compute the ODE system. The root-finder subroutine is optional and does not need to be used in every simulation. It allows the user to define a target value for a variable, such as a species mass fraction or temperature. It returns the time at which the system reaches that specified value.

The *m_jacobian_auxiliary* module was developed to assist in the setup of the Jacobian matrix. While the use of a Jacobian matrix is not mandatory, it is often recommended for larger kinetic mechanisms, as it can significantly improve the convergence rate of the system. In the present case, the Jacobian matrix was not utilised, because the GMRES method was preferred .

The *m_print_output* module provides customised information regarding the solver's performance. The *m_solver* module is where the solver itself is constructed. By using the SUNDIALS suite, the program offers high flexibility in selecting the numerical method used by CVODE. Any modifications to the solver configuration can be made without requiring changes to other program modules. Furthermore, the structure enables the integration of other solvers from the SUNDIALS suite, providing additional adaptability for future developments.

The solver allows for the definition of a relative tolerance, common for all variables, and different values for the absolute tolerances. These are used to calculate the acceptable error within the solver through the following equation [180]:

$$Err_i = \frac{1}{rtol|y_i| + atol_i} \quad (4.27)$$

Where $rtol$ is the relative tolerance, Err_i is the error, $atol_i$ is the absolute tolerance, and y_i is the current value of variable i.

4.5.3 Graphical Post-Processor

Finally, the third segment, the Graphical Post-Processing, uses a Python script to generate the required plots. The script offers high flexibility in developing user-required plots.

4.6 Solver Settings

The program uses the Scaled, Preconditioned, Generalised Minimum Residual method (SPGMR) coupled with the default non-linear method, the Newton iteration, to solve Equation 4.19. The SPGMR linear solver is given by a SUNDIALS module enabling the method implementation. As seen before, this Krylov method has a faster computation time for large mechanisms. Even though McNenly [168] showed that for a smaller hydrogen-oxygen mechanism, a more straightforward dense matrix approach could be faster, the time difference is not significant. On the other hand, to expand the kinetic base, the implementation of SPGMR will ensure that future applications will not encounter problems with solution convergence time.

As previously discussed, error calculations involve both relative and absolute tolerances. In the present work, the relative tolerance was set to 10^{-6}, which falls within the recommended range [180]. This value is applied uniformly across all variables in the system. On the other hand, the absolute tolerance vector allows for assigning different tolerances to each variable, which is particularly useful in systems where the species' concentrations have different magnitudes. For major species such as O_2 and H_2, a "looser" tolerance can be used due to their higher concentrations. However, for radicals and intermediate species, a "tighter" tolerance is more appropriate. Table 4.1 presents the absolute tolerances used during the simulations.

Table 4.1: Absolute tolerance during simulations.

Species	O2	O	H2	H	OH	H2O
Tolerance	1×10^{-14}	1×10^{-21}	1×10^{-14}	1×10^{-21}	1×10^{-18}	1×10^{-16}

Species	HO2	H2O2	Ar	He	N2	OH*
Tolerance	1×10^{-20}	1×10^{-20}	1×10^{-16}	1×10^{-16}	1×10^{-16}	1×10^{-20}

Temperature	T
Tolerance	1×10^{-2}

Furthermore, the SUNDIALS suite allows the use of a constrain vector. This tool ensures that the program runs when the variables are bigger or smaller than a certain value. In this case, it has been defined that every variable (species' mass fraction and temperature) should have a value greater than 0, preventing unphysical values during running time.

As for the SPGMR linear method, the default settings were considered. Since the mechanism, even though stiff, is not very complex and therefore easy to compute. However, if the number of species or reactions is increased, a more detailed analysis of the solver's settings may enhance the program's efficiency.

Chapter 5

Results and Discussion

The numerical model described in Chapter 4 was implemented to simulate H_2-O_2 combustion in an isobaric and adiabatic flow reactor, using a zero-dimensional framework. The experimental datasets used for validation, obtained from Mueller et al. [53] and Yetter et al. [181], are introduced in Section 5.1. Section 5.2 outlines key considerations for ensuring a meaningful comparison between numerical and experimental results. In Section 5.3, the numerical results are compared with these experimental data to validate the model and to gain deeper insight into combustion behaviour under varying initial conditions.

5.1 Overview of simulation cases

In order to validate the combustion model using the Kéromnès et al. mechanism [55], experimental data from flow reactor studies were employed, namely those from Mueller et al. [53] and Yetter et al. [181]. In the work of Mueller et al. [53], the experiments were conducted exclusively with O_2–H_2 mixtures, while Yetter et al. [181] primarily investigated CO–O_2 mixtures, using only one case involving an O_2–H_2 mixture. In both experimental setups, the reactants were not premixed. Instead, they were introduced separately into the reactor. Nitrogen served as the balance gas, meaning it occupied the remaining fraction of the mixture not filled by the reactive species. Detailed descriptions of the experimental apparatus used in both studies can be found in the respective publications.

The comprehensive data set of Mueller et al. [53] was the primary reference for model validation. Their experiments cover pressure and initial temperature ranges of 0.3–15.7 atm and 850–943 K, respectively, for mixtures spanning from fuel-lean to stoichiometric conditions. This dataset is widely used in the literature to assess mechanism performance, including by Kéromnès et al. [55] during the development of their mechanism. Consequently, numerical predictions from the model are expected to show very good agreement with these experimental results. Moreover, this dataset is particularly valuable because it explores conditions beyond the first explosion limit, where reactions involving the formation and consumption of HO_2 and H_2O_2 become especially relevant. Additionally, the single O_2–H_2 dataset from Yetter et al. [181] was also used for validation. This case corresponds to a pressure of 1.00 atm, an initial temperature of 910 K, and an equivalence ratio of 0.28. Table 5.1 summarizes all experimental cases used in the model validation.

Figure 5.1 to 5.14 compare the simulations with experimental data. Results show the ex-

Table 5.1: Initial conditions for the experimental analysed data (x_{N_2}, from balance).

Experimental Case	Figure	p [atm]	T_{in} [K]	x_{H_2} [%]	x_{O_2} [%]	Time Shift [s]	Source
1	5.1	3.02	934	0.95	0.49	0.124	[53]
2	5.4	2.55	935	1.01	0.52	0.295	[53]
3	5.5	3.44	933	1.01	0.52	0.264	[53]
4	5.6	6.00	934	1.02	0.52	0.324	[53]
5	5.2	0.30	880	0.50	0.50	0.064	[53]
6	5.7	0.60	897	0.50	0.34	0.075	[53]
7	5.7	0.60	896	0.50	0.76	0.044	[53]
8	5.8	2.55	935	1.01	0.52	0.288	[53]
9	5.8	2.50	943	1.00	1.50	0.231	[53]
10	5.9	15.70	914	1.18	0.61	0.265	[53]
11	5.9	15.70	914	1.18	2.21	0.315	[53]
12	5.10	6.50	884	1.29	2.19	0.305	[53]
13	5.11	6.50	889	1.30	2.21	0.591	[53]
14	5.12	6.50	906	1.32	2.19	0.496	[53]
15	5.13	6.50	914	1.36	2.24	0.420	[53]
16	5.14	6.50	934	1.36	2.24	0.266	[53]
17	5.3	1.00	910	0.8482	1.052	0.255	[181]

pected behaviour and are in very good agreement with the experimental data. Some discrepancies appear in the predicted concentrations of H_2 and H_2O in Figures 5.1 and 5.5, a behaviour that is also noted in the original work of Mueller et al. [53]. According to the authors, at these pressure levels the reaction rate in the thermal/chain-branching regime increases, and the transition associated with crossing the second explosion limit becomes less pronounced. As a result, the experimental identification of this transition becomes more challenging, which may account for the observed discrepancies. Conversely, Figure 5.8 also shows noticeable differences between the experimental and numerical results, particularly for case 9. This deviation may be again linked to the transitional chemistry behaviour previously discussed. However, as will be shown later, the composition of the radical pool is highly sensitive to the mixture stoichiometry, and even small shifts in the equivalence ratio can lead the system to follow different reaction pathways. Therefore, it is reasonable to suggest that the discrepancy observed in case 9 may arise from inaccuracies in the Arrhenius parameters used to describe the reactions governing the system's evolution.

For every figure in this chapter, the numerical results are represented as non-continuous lines, the concentration usually in blue and the temperature in red. As for the experimental data points different representation were used as hollow circle, triangles, squares, and circles.

5.2 Time shift

As highlighted by several authors, including O'Conaire et al. [56], Li et al. [57], Burke et al. [51], and Mueller et al. [53], a time shift is commonly applied to align numerical results

with experimental species profiles. This adjustment compensates for the non-ideal mixing that occurs at the reactor inlet, where diffusion and incomplete homogenisation can alter the onset of the chemical induction period and delay the observable ignition behaviour in experiments [53].

Mueller et al. [53] emphasise that near the injection point, mixing and diffusion play a significant role in determining the chemical induction time. Further downstream, however, the flow enters a regime of high convective velocity. Under these conditions, convective transport dominates over radial diffusion, effectively suppressing spatial gradients in temperature and species concentration. Consequently, the diffusive terms in the governing equations can be neglected, as discussed in Section 4.3, and the test section can be modelled as a zero-dimensional (0D) system.

This simplification assumes that chemical perturbations introduced in the mixing region do not leave a "memory effect" once the flow reaches the high-velocity test section. While these perturbations affect induction chemistry and cannot be modelled explicitly, they do not significantly influence the main reaction zone, where major species evolve [181]. For a meaningful comparison between simulations and experiments, numerical results are shifted along the time axis so that the point of 50% fuel consumption matches the corresponding experimental value [56]. Table 5.1 summarises the specific time shifts for each experimental case.

However, under certain experimental conditions where reactions occur over very short timescales, diffusive processes may no longer be negligible. In these scenarios, the assumption of negligible axial diffusion becomes less reliable. Comparisons between experimental data and 0D model predictions should be interpreted with caution. This limitation is acknowledged throughout the present analysis.

The time shift for each condition was not explicitly studied in the original work by Kéromnès et al. [55]. Nevertheless, it was possible to retrieve these values for the conditions examined in this study. Although the numerical results obtained with the present mechanism do not exactly match those of earlier studies, which is expected due to differences in the chemical mechanisms used, the time shift values show good agreement with those reported by O'Conaire et al. [56], who also compared calculated values using the mechanism proposed by Mueller et al. [53].

5.3 Influence of key initial conditions on system evolution

The present section presents a comparison between numerical simulations and experimental data. It begins by characterizing the system's behaviour under different explosion limits, highlighting how these regimes influence reaction times and combustion dynamics. Following this, the results are organized based on their initial conditions, namely pressure, equivalence ratio, and temperature, to facilitate a clearer analysis of how each

parameter affects the evolution of the system and the dominant reaction pathways.

Cases 2, 3, and 4 share similar initial temperatures and compositions, with pressure being the changed variable (2.55, 3.44, and 15.7 atm, respectively). In contrast, Cases 5 through 11 are grouped in pairs, each set maintaining constant initial temperature and pressure while varying the equivalence ratio by adjusting the initial oxygen mole fraction. Finally, Cases 12 to 16 focus on the impact of initial temperature on combustion behaviour, highlighting how thermal conditions influence the progression and nature of the reaction mechanisms.

5.3.1 Explosion limits

Figures 5.1, 5.2, and 5.3 show the evolution of the reactive mixture under sub-atmospheric, atmospheric, and super-atmospheric conditions, respectively. The results demonstrate good agreement with the experimental data, with a slight overestimation of temperature observed in the sub-atmospheric and super-atmospheric cases. These differences were also observed by Mueller et al. [53] who suggested the inclusion of a correction factor to have into consideration the heat loss through the reactors walls. However, the inclusion of this parameter, in the super-atmospheric case, did not yield considerable changes in the predicted temperature profile. Therefore, as in the work of Mueller et al. [53] the present mechanism also did not include the global heat transfer coefficient.

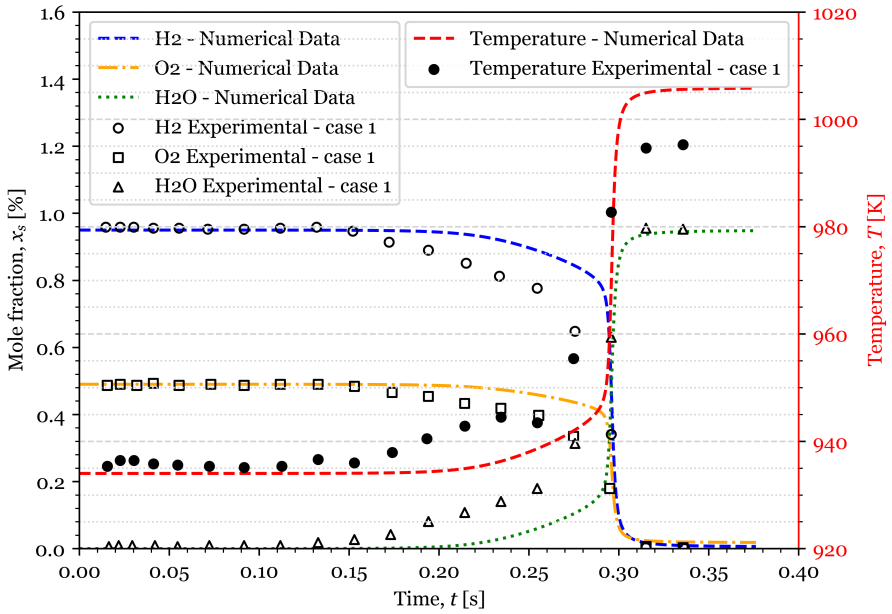

Figure 5.1: Reaction profiles for the H_2/O_2 reaction at 3.02 atm, T_{intial} = 934 K, and ϕ = 0.97.

At the beginning of the reaction, in Figure 5.1, the mixture is in the thermal/chain explosion regime, characterised by a slower reaction rate where reactants interact through pathways involving heavier intermediates. After approximately 20% of the fuel is con-

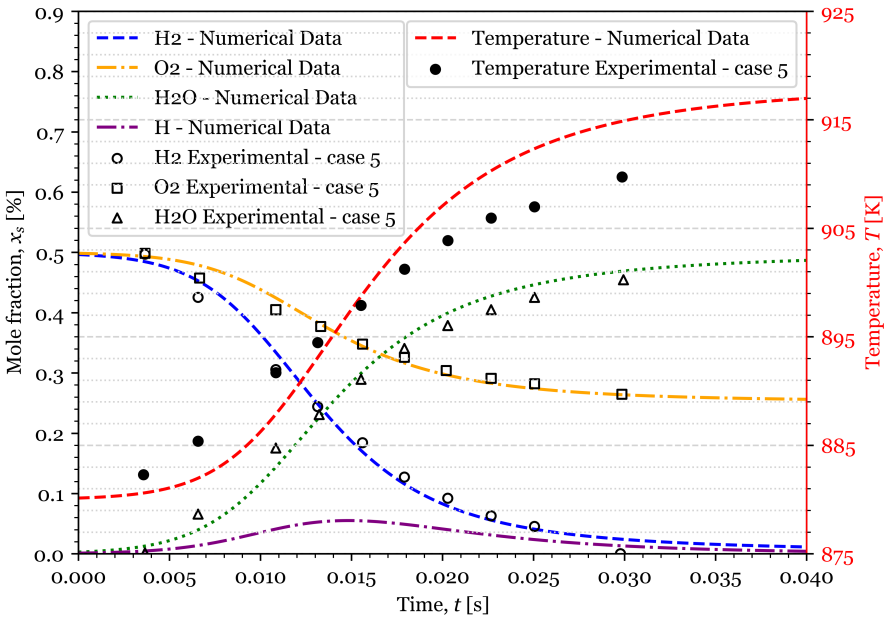

Figure 5.2: Reaction profiles of the H_2/O_2 reaction at 0.3 atm, T_{intial} = 880 K and ϕ = 0.5.

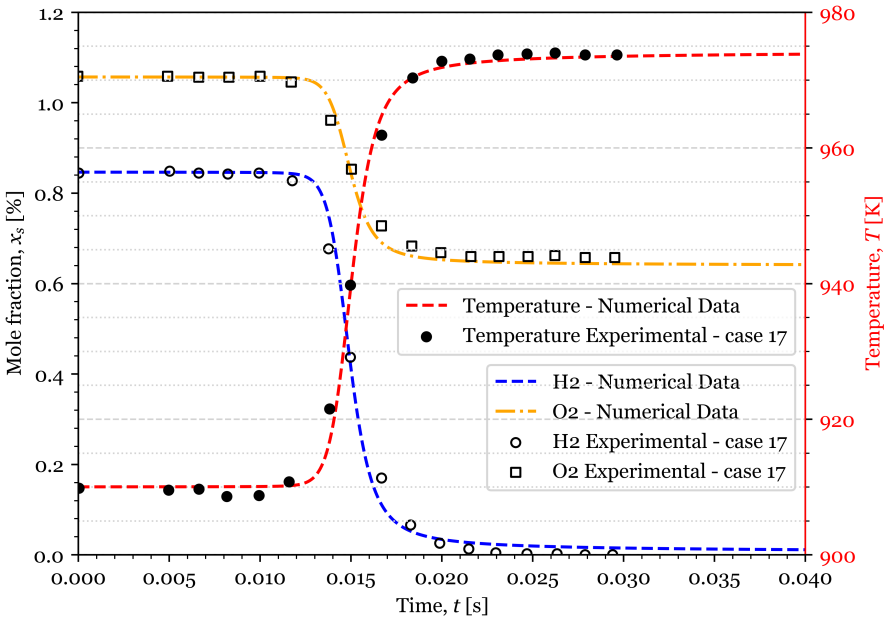

Figure 5.3: Reaction profiles of the H_2/O_2 reaction at 1.0 atm, $T_{initial}$ = 910 K and ϕ = 0.28.

sumed, the reaction rate increases significantly and the remaining fuel is consumed within 0.5 s. This behaviour suggests a transition to a chain-branching explosion regime, where the rise in temperature (crossing to the extended second limit) accelerates the reaction through rapid chain-branching processes. Although not plotted due to its relatively low concentration, the mole fraction of the dominant radical H begins to increase at this stage, marking the onset of more intense reactivity.

In contrast, Figures 5.2 and 5.3 exhibit behaviour typical of a chain-branching explosion regime from the outset, with rapid consumption of reactants. Interestingly, the reaction at sub-atmospheric pressure proceeds even faster. This can be attributed to the lower pressure conditions, which favour chain-branching reactions and promote a more explosive combustion regime. Compared to the high-pressure case, the difference is evident: both the sub- and atmospheric pressure reactions are almost completely developed by 40 ms, while the high-pressure case shows minimal change in composition at the same time.

Figure 5.2 also includes the evolution of the H radical. Under chain explosion conditions (first explosion limit), light radicals such as H dominate the reactive mixture and play a critical role in determining the reaction pathway. Comparing this to the high-pressure case, where the H radical is not plotted due to its initially low concentration, it becomes apparent that the formation of H is closely linked to the transition into a more explosive regime, as predicted in literature.

5.3.2 Influence of pressure on the system evolution

Figures 5.4, 5.5, and 5.6 show the numerical and experimental results for three systems with similar initial temperatures (935 K) and composition (1.01% H_2, 0.52% O_2, and 98.47% N_2), and at three different pressures (2.55, 3.44 and 6.0 atm). The results show the system evolution in the extended second limit (see Figure 3.1).

It is important to note that the zero-dimensional assumption may not be valid for the reaction at 2.55 atm and during the rapid portion of the reaction at 3.44 atm [53].

At 2.55 atm, the mixture is well within the chain-branching explosion regime. After a short induction period, a rapid reaction occurs, leading to the complete consumption of the reactants. At 3.44 atm, the mixture transitions into the thermal/chain explosion regime, where the reaction proceeds more slowly compared to the previous case. Nevertheless, the heat released during the reaction is sufficient to raise the temperature and drive the mixture into an explosive state. At 6.0 atm, however, the heat release is no longer adequate to trigger a chain explosion. As a result, the reactants are consumed gradually, and the reaction proceeds in a slow and steady manner.

The numerical results show good agreement with the experimental data, particularly for the 2.55 atm and 6.0 atm cases. However, the combustion model encounters difficulties in accurately predicting the behaviour under transitional chemistry conditions, such

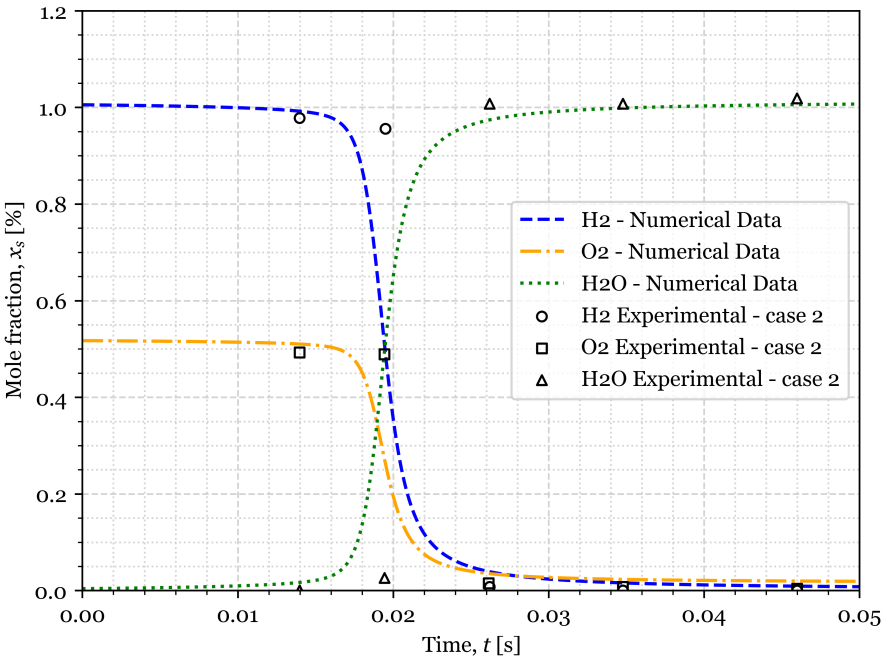

Figure 5.4: Reaction profiles of the H_2/O_2 reaction at 2.55 atm, T_{intial} = 935 K and ϕ = 0.97.

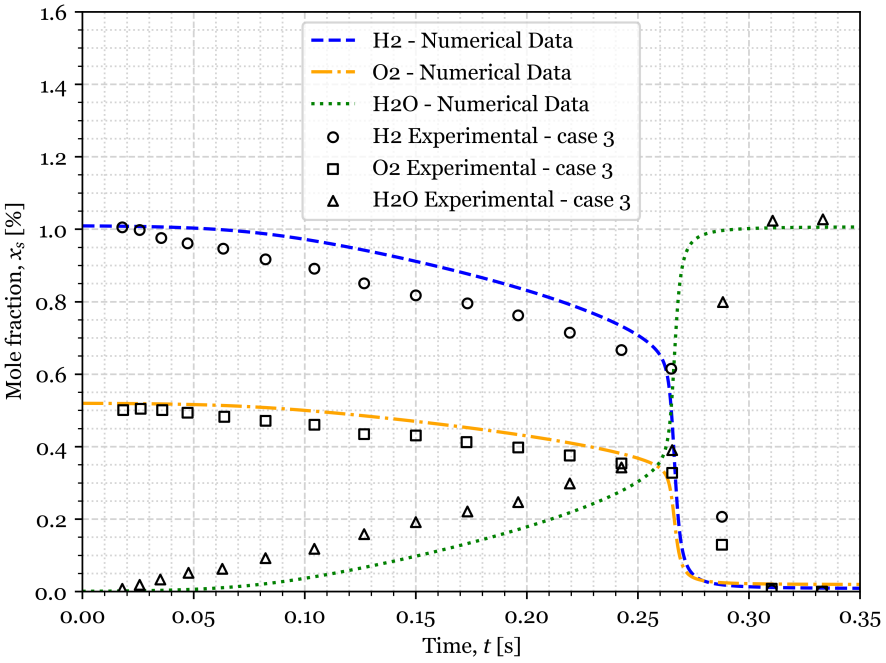

Figure 5.5: Reaction profiles of the H_2/O_2 reaction at 3.44 atm, T_{intial} = 933 K and ϕ = 0.97.

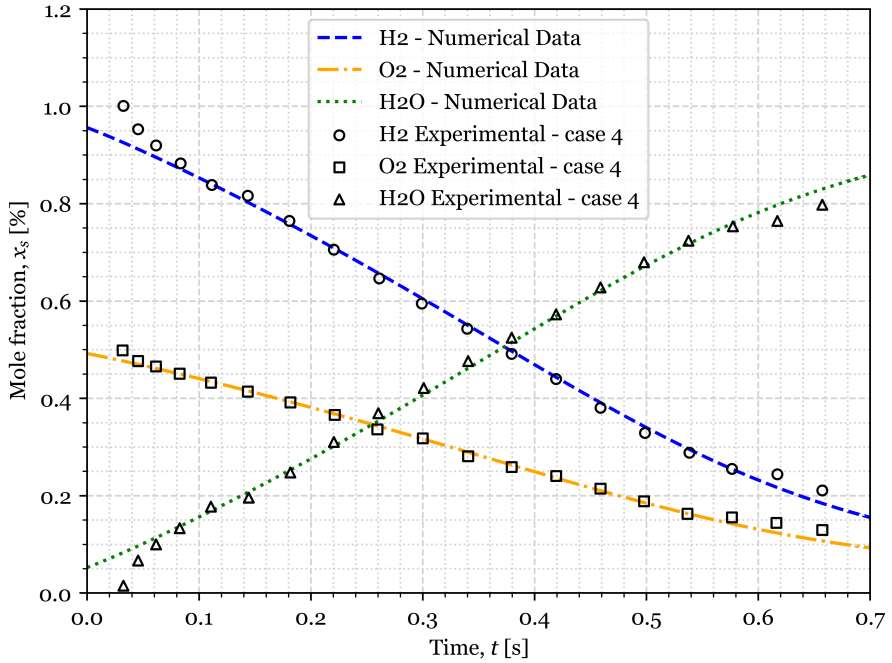

Figure 5.6: Reaction profiles of the H_2/O_2 reaction at 6.0 atm, T_{intial} = 934 K and ϕ = 0.97.

as at 3.44 atm. As in the case shown in Figure 5.1, the reaction initially proceeds slowly during the induction phase and becomes more reactive as temperature rises and chain-branching pathways accelerate. Mueller et al. [53] note that, within the 3.0–6.5 atm range characteristic of transitional chemistry, the transition across the extended second explosion limit becomes less pronounced and increasingly difficult to observe experimentally. This reduced experimental visibility, coupled with the extreme sensitivity of the reaction rate to small variations in temperature near the explosion limit, likely contributes to the discrepancies observed at 3.44 atm.

5.3.3 Influence of initial equivalence ratio on the system evolution

Figures 5.7, 5.8, and 5.9 illustrate the simulation and the experimental data for the six different systems. Three different pressures where selected to represent the chain-branching explosion regime, the transition regime (extended second explosion limit), and the thermal/chain regime, respectively.

It is important to note at the zero-dimensional assumption may not be valid for the stoichiometric reaction at 2.55 atm.

Once again it is simple to see the differences between the chain explosion and the thermal/chain regimes (0.6 and 15.70 atm). In Figure 5.7, both reactions occur very rapidly, consuming the fuel in under 30 ms. Case 7 is slightly faster.

The case illustrated in Figure 5.8 offers valuable insight into the behaviour of H_2-O_2 com-

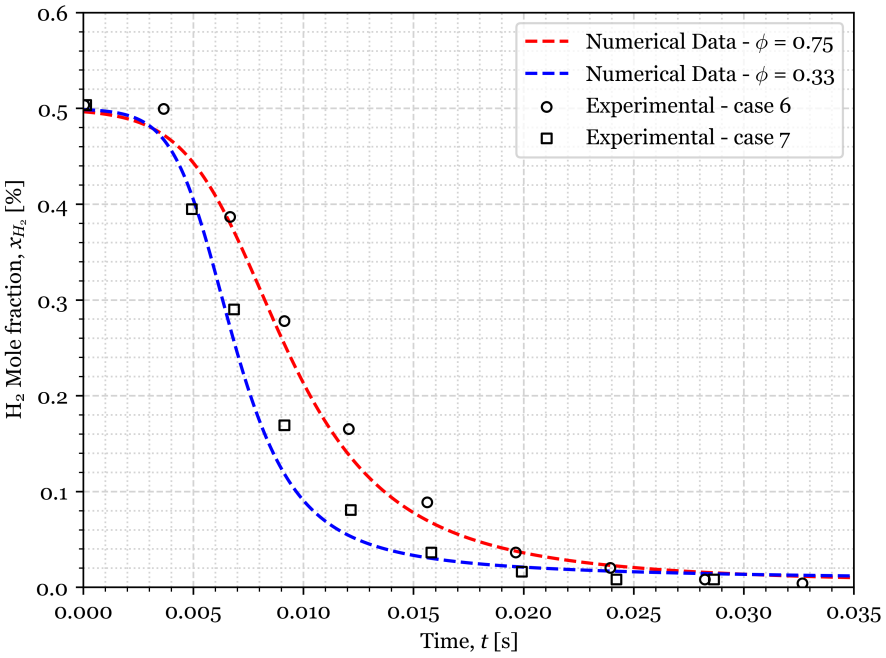

Figure 5.7: Reaction profiles of the H_2/O_2 reaction at 0.6 atm and T_{intial} = 897 K for ϕ = 0.75 and ϕ = 0.55.

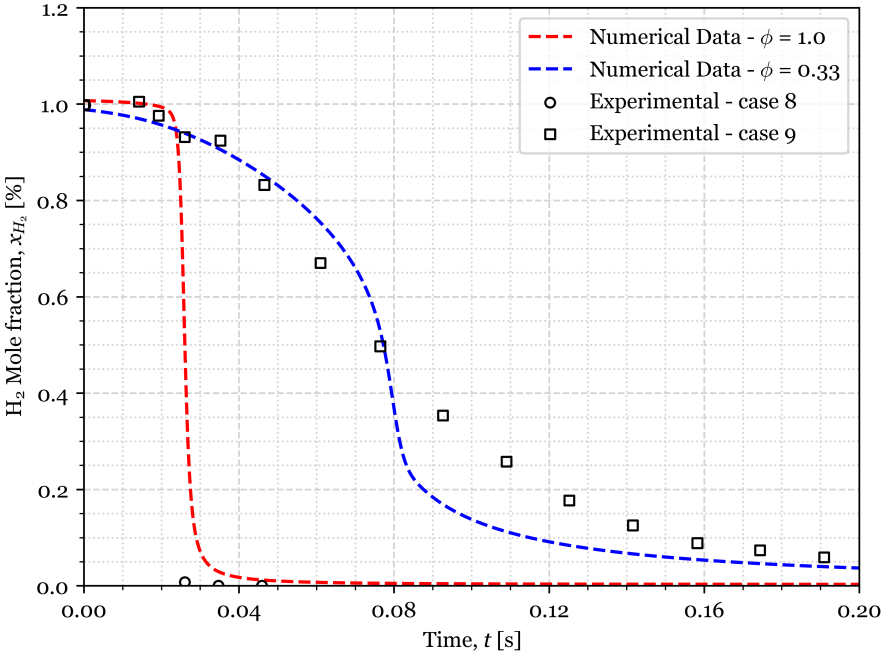

Figure 5.8: Reaction profiles of the H_2/O_2 reaction at 2.55 and 2.50 atm and T_{intial} = 940 K for ϕ = 1.0 and ϕ = 0.33.

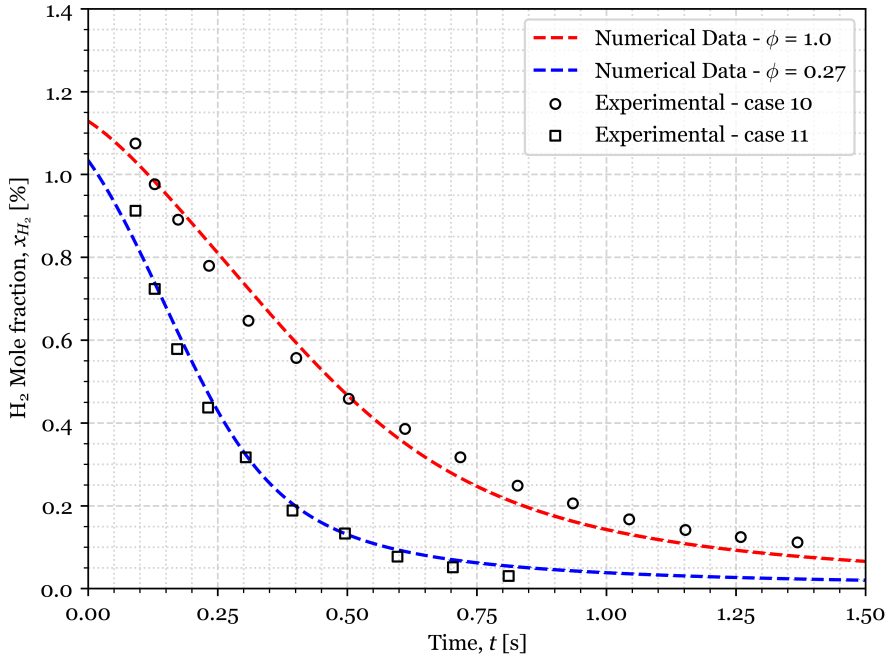

Figure 5.9: Reaction profiles of the H_2/O_2 reaction at 15.70 atm and T_{intial} = 914 K for ϕ = 1.0 and ϕ = 0.27.

bustion kinetics near the extended second explosion limit, particularly around 3 atm. As shown, the system exhibits a high sensitivity to variations in the equivalence ratio under these conditions. Following the methodology of Mueller et al. [53], the maximum mole fractions of key radicals — H, O, OH, HO_2, and H_2O_2 — were calculated for six different cases. The results obtained using the developed model are presented in Table 5.2, while those based on Mueller et al.'s mechanism are shown in Table 5.3. Both tables report the radical concentrations in parts per million (ppm).

Table 5.2: Maximum mole fraction of radicals in different conditions.

	p = 0.6		p = 2.55		p = 15.7	
Species	ϕ = 0.75	ϕ = 0.33	ϕ = 1.0	ϕ = 0.33	ϕ = 1.0	ϕ = 0.27
H	13.2	8.39	5.48	0.237	0.00102	0.000323
O	19.2	26.7	7.51	1.62	0.00152	0.00315
OH	16.3	26.1	10.3	2.07	0.00666	0.0131
HO2	1.72	3.59	9.31	16.9	6.43	9.20
H2O2	0.0627	0.160	9.87	39.9	31.2	51.3

Table 5.3: Maximum mole fraction of radicals in different conditions using Mueller et al. mechanism [53].

	p = 0.6		p = 2.55		p = 15.7	
Species	ϕ = 0.75	ϕ = 0.33	ϕ = 1.0	phi = 0.33	ϕ = 1.0	ϕ = 0.27
H	318	215	127	6.3	0.02	0.01
O	27.2	39.1	10.9	2.7	0.002	0.004
OH	18.5	29.7	13	3	0.006	0.01
HO2	0.9	2.3	3.8	11.4	4.4	6.4
H2O2	0.02	0.08	0.1	3.6	12.4	22.6

A comparison between the results presented in Tables 5.2 and 5.3 reveals a noticeable discrepancy in the predicted radical concentrations. This divergence may stem from the fact that the data reported by Mueller et al. [53] is based on the maximum reaction rates, whereas the present results are not. Additionally, differences in the applied kinetic mechanisms could also contribute to the observed inconsistencies. Nevertheless, it is noteworthy that the overall evolution of the radical pool follows a similar trend across both datasets.

In the sub-atmospheric case, the radical pool is predominantly governed by fast-reacting radicals, indicating that combustion proceeds mainly through chain-branching reactions. At 2.55 atm, the system appears to enter a transitional regime, where the distribution of radicals becomes more balanced. This is particularly evident in the fuel-lean mixture, where heavier radicals begin to dominate the radical pool. At higher pressures, combustion clearly shifts toward a thermal regime, characterized by the formation of HO_2 and H_2O_2, as expected.

Furthermore, it is important to highlight the sensitivity of mixtures near the second explosion limit to changes in the equivalence ratio. At stoichiometric conditions, the mixture exhibits behaviour typical of a chain explosion regime, as evidenced by the rapid reaction progression and swift consumption of reactants. However, the addition of excess oxygen significantly alters the reaction kinetics. In fuel-lean conditions, the radical pool becomes dominated by heavier species, particularly HO_2, and the overall reaction rate decreases, indicating a transition to a thermal/chain regime.

This shift can be attributed to changes in the dominant reaction pathways. In the chain explosion regime, HO_2 is primarily consumed via reaction R30, driven by the high concentration of atomic hydrogen. In contrast, under fuel-lean conditions, the reduced concentration of H, now comparable to other fast radicals such as O and OH, leads to alternative consumption pathways for HO_2, including reactions R32 and R33.

5.3.4 Influence of initial temperature on the system evolution

Figures 5.11 - 5.14 exhibit five mixtures both at 6.5 atm with similar compositions (1.29 - 1.36% H2, 2.19 - 2.24% O2, and 96.40 - 96.52% N2), and with different mixture initial temperatures (884, 889, 906, 914, and 934 K).

The agreement between experimental and numerical results is generally good, with the exception of the initial data at lower simulation times for the mixture with an initial temperature of 906 K, and the final data point for the mixture at 889 K. These discrepancies were also noted by Mueller et al. [53].

This set of results highlights the significant influence of initial mixture temperature on the overall reaction behaviour. At this high pressure, the reaction evolution is highly sensitive to temperature variations. In fact, a relatively small increase of just 50 K causes the system

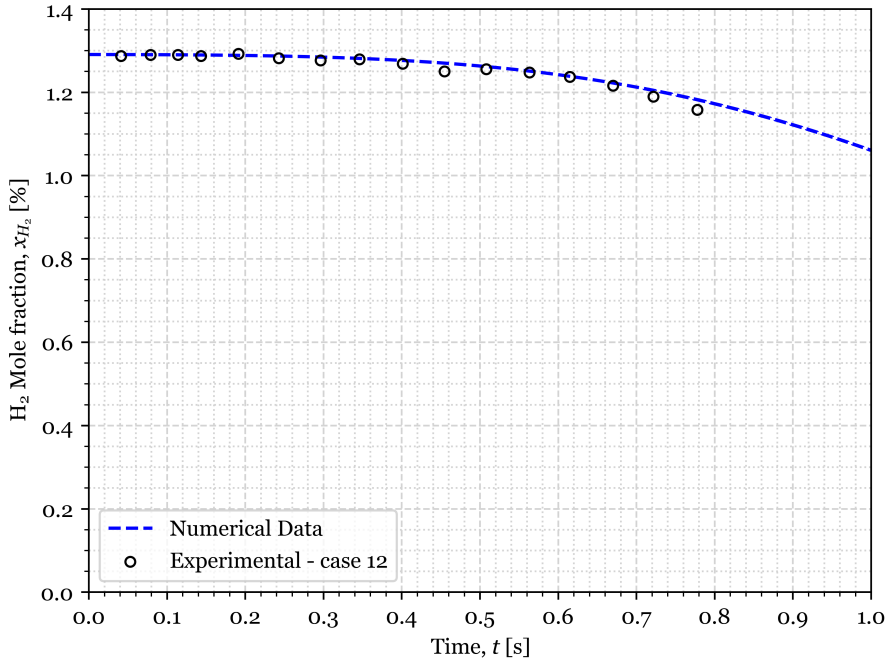

Figure 5.10: Reaction profiles of $H_2/O_2/N_2$ mixture at 6.5 atm, T_{intial} = 884 K and ϕ = 0.29.

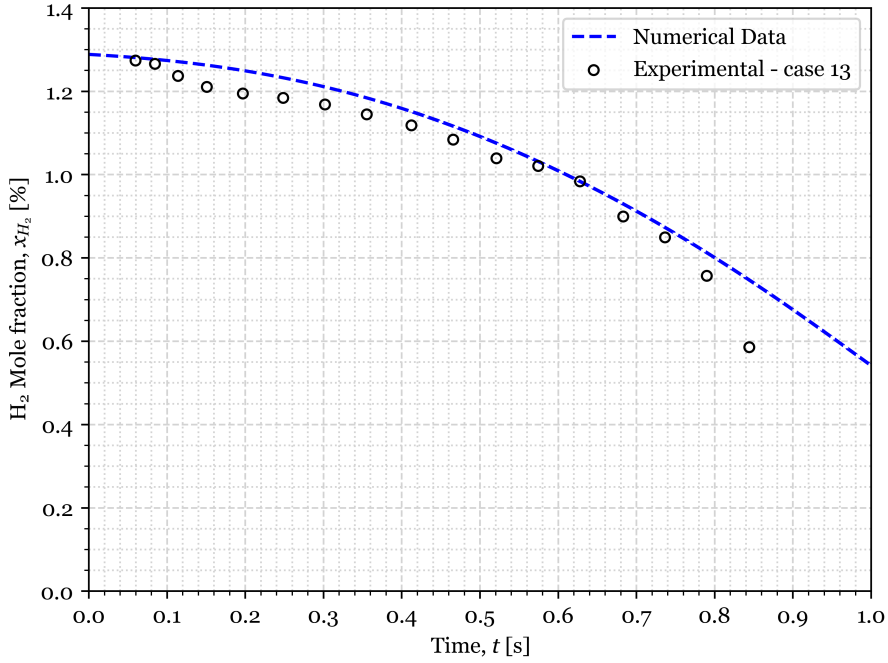

Figure 5.11: Reaction profiles of $H_2/O_2/N_2$ mixture at 6.5 atm, T_{intial} = 889 K and ϕ = 0.29.

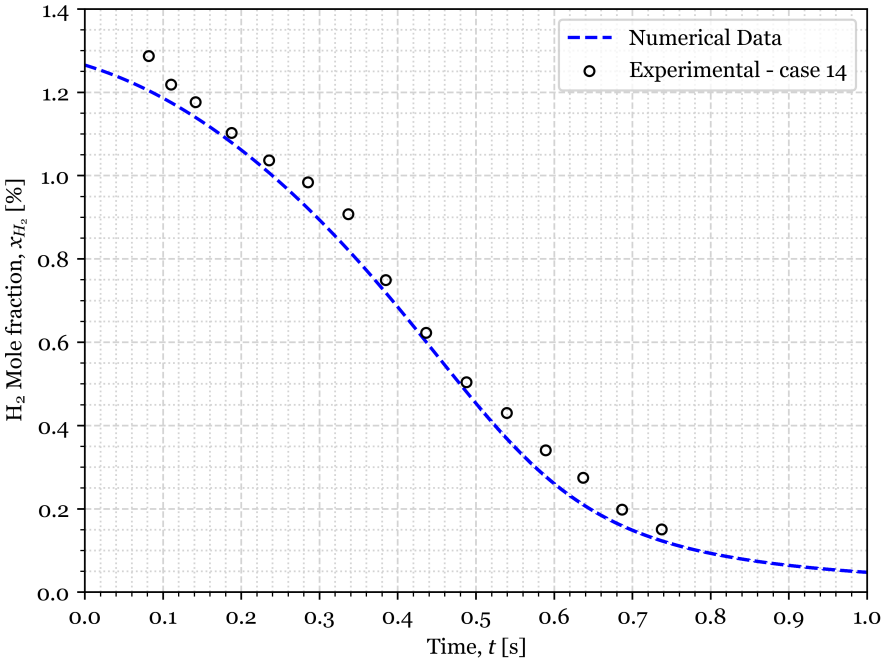

Figure 5.12: Reaction profiles of $H_2/O_2/N_2$ mixture at 6.5 atm, T_{intial} = 906 K and ϕ = 0.30.

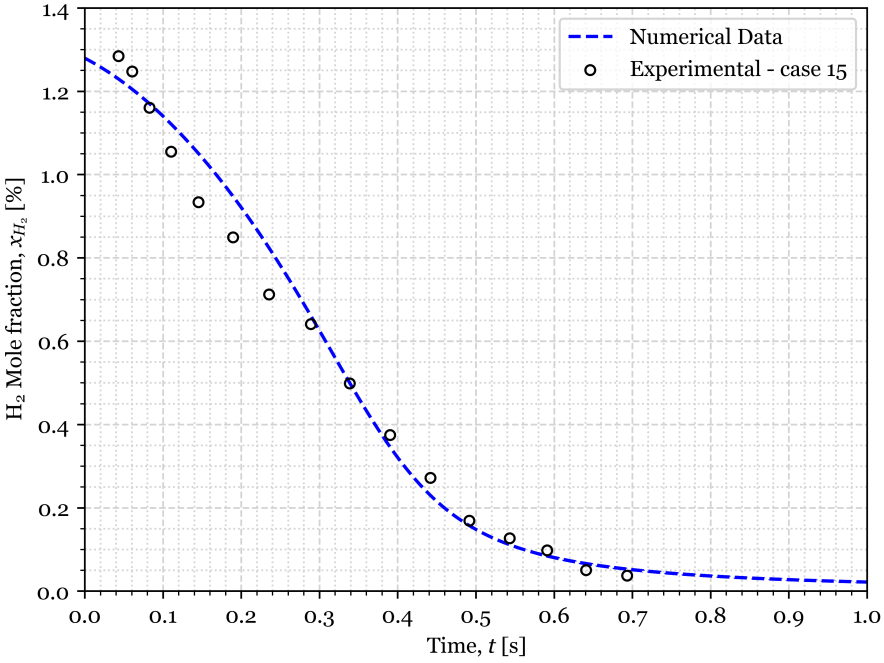

Figure 5.13: Reaction profiles of $H_2/O_2/N_2$ mixture at 6.5 atm, T_{intial} = 914 K and ϕ = 0.30.

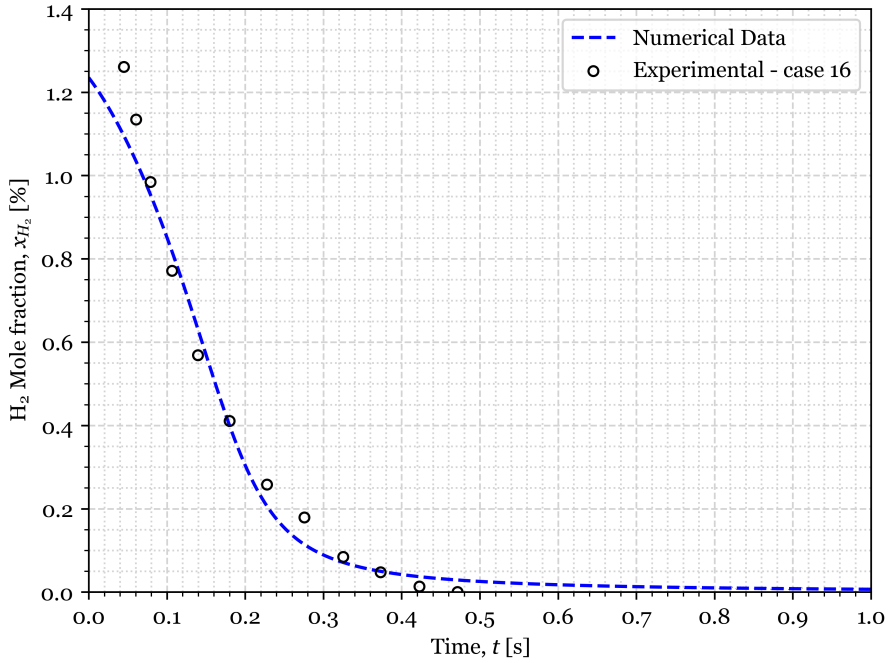

Figure 5.14: Reaction profiles of $H_2/O_2/N_2$ mixture at 6.5 atm, T_{intial} = 934 K and ϕ = 0.30.

to shift from a slow, steady reaction to a rapid and complete consumption of hydrogen in under 0.8 seconds. While previous analysis have emphasised the role of pressure in determining reaction pathways, these results clearly demonstrate that temperature also plays a critical role in defining the combustion regime and reaction dynamics.

Chapter 6

Conclusions and Future Work

This chapter presents the conclusions derived from the numerical model implementation for analysing chemical kinetic mechanisms. Section 6.1 summarises the key outcomes of the combustion model and reflects on aspects that could have been further improved. Additionally, Section 6.2 outlines several promising directions for future research, building upon the findings and capabilities established throughout this study.

6.1 Conclusions

The present work focused on the development of a numerical model designed to simulate chemical kinetic mechanisms. The model was used to analyse an H_2-O_2 mechanism and to validate its behaviour under various conditions.

A review of commonly used propellants highlighted the oxygen/hydrogen combination as one of the most popular choices, which justified its selection for further investigation. Additionally, an examination of kinetic modelling approaches confirmed that detailed chemical mechanisms were the most reliable method for capturing the complex behaviour of reactive flows under high-pressure conditions. Following the adoption of this modelling strategy, it became essential to understand how these kinetic schemes were parametrised to accurately represent the reactions pathways and rates within the numerical model. In this work, the mechanism developed by Kéromnès et al. [55] was selected for implementation.

The combustion model was implemented using the SUNDIALS suite, specifically the CVODE solver, which provided flexibility for future adaptations. The resulting model featured a modular architecture designed to facilitate integration and adaptability. To evaluate its accuracy and reliability, the model was applied to a well-established kinetic mechanism and tested under simplified conditions—namely, adiabatic, isobaric, and zero-dimensional flow reactor configurations. These conditions isolated the chemical kinetics from fluid dynamic effects, enabling focused validation and verification of species interactions. Comparisons with experimental data confirmed the model's ability to reproduce the expected species evolution, thereby validating its suitability for future coupling with a comprehensive reactive flow simulation framework.

As demonstrated in Chapter 5, the numerical model accurately reproduces the expected behaviour of the kinetic mechanism across a range of initial conditions. The experimental

dataset used for validation spans pressures from 0.3 to 15.7 atm, initial temperatures between 880 and 943 K, and initial equivalence ratios from 0.27 to 1.0. This wide range of conditions enabled a robust validation, particularly around the second and extended second explosion limits of H_2-O_2 combustion, which are critical for understanding ignition behaviour.

However, the accessibility to other experimental data for broader validation was limited. The most comprehensive dataset for flow reactor experiments found was presented by Mueller et al. [53], which provides detailed measurements primarily focused on the second explosion limit and its immediate vicinity. While the results obtained in this work align well with those data, further validation under different conditions would strengthen the conclusions.

In particular, it would be valuable to compare simulation results with experimental data representative of conditions relevant to LRE applications, namely higher pressures up to 10 MPa. Such comparisons would help assess the mechanism's performance in regimes of practical engineering interest and guide future improvements to the model.

Alternatively, some other kinetic mechanism could have been employed in this research. While the mechanism of Kéromnès et al. [55] was selected because of its robustness and good documentation, it should be pointed out that it was developed as an advancement of a previous mechanism that may not have been optimised for typical conditions of LREs. On the other hand, the Shimizu et al. mechanism [60] was explicitly formulated to mimic combustion under the high-pressure regime characteristic of LREs. However, the lack of proper experimental data to validate the combustion model with the Shimizu mechanism may have posed serious difficulties. Furthermore, the Kéromnès mechanism belongs to a highly tested and well-documented family of models, which helped simplify its validation and reduce potential implementation errors. As a final remark, it must be noted that the primary objective of this work was not the performance optimisation at high-pressure conditions but to implement a strong and flexible combustion model that can handle a wide range of kinetic mechanisms and operating conditions.

6.2 Future work

Following the literature and existing research, several promising directions for future studies can also be identified. One immediate extension is to use the developed numerical model to simulate shock tube conditions. This would allow for a direct comparison with experimentally determined ignition delay times and concentration profiles of species, providing a further test of the kinetic mechanisms adopted. Additionally, incorporating diffusion effects would enable the model to simulate flame propagation, starting from one-dimensional laminar flames and subsequently extending to more complex turbulent combustion regimes. This would later be integrated with the turbulence model worked

out at AEROG to produce an in-house tool that can simulate real combustion chamber conditions in LREs.

Another worthwhile area of extension is the implementation of kinetic mechanisms with heavier hydrocarbons, namely methane. Methane is being considered a feasible substitute for hydrogen as a rocket fuel due to its higher density, allowing it to have smaller and lighter tanks [182]. Its higher boiling point reduces insulation requirements and simplifies thermal management. In addition, methane's ease of handling (being self-venting and thermally compatible with liquid oxygen) enables the use of common components, further lowering system complexity and cost [183]. These advantages make methane a likely candidate for future propulsion systems, especially in reusable launch vehicles and interplanetary space missions [184].

However, modelling heavier hydrocarbons involves considerable computational challenges, as increased species and reactions are required in detailed kinetic mechanisms. An alternative is to design and apply reduced kinetic mechanisms. These keep the reaction paths at their fundamental levels but reduce the computational power required immensely, making them more feasible for simulations on a large scale or real-time applications. Reduced schemes would be beneficial when simulating complex fuels or simulating entire combustion chambers.

At the same time, one should also aim for improvements in computational efficiency. This implies exploring new parametrisations of the solver and other numeric methods (linear and non-linear) with the potential to reduce simulation times. All these are necessary when faced with more complex hydrocarbon combustion or when scaling up to simulate overall combustion chamber dynamics.

Finally, there is an additional research path, which is experimental verification. It would make a big difference in model credibility if experimental setups for measuring rate constants or generating high-pressure data sets were available. Even though theoretical methods, like ab initio calculations, have improved, they are nevertheless typically inferior to experiment accuracy. Experimental data are still required to optimise significant parameters and validate model predictions. Additionally, sensitivity analyses that associate observables with rate constants can identify key reactions, inform experimental priorities, and enhance model robustness. Synergies between contemporary quantum chemistry and judicious experimentation will be essential to develop predictive combustion modelling [185].

Bibliography

[1] ESA, "ESA for Earth." https://www.esa.int/Applications/Observing_the_Earth/ESA_for_Earth. Accessed: 06-03-2024. 1

[2] H. Jones, "The Recent Large Reduction in Space Launch Cost," in *48th International Conference on Environmental Systems (ICES)*, (Albuquerque, New Mexico, USA), ICES, 2018. 1

[3] United Nations Office for Outer Space Affairs, "Online Index of Objects Launched into Outer Space." https://www.unoosa.org/oosa/osoindex/search-ng.jspx, 2025. Accessed: 16-06-2025. 1

[4] Our World in Data, "Annual Number of Objects Launched into Space." https://ourworldindata.org/grapher/yearly-number-of-objects-launched-into-outer-space, 2025. Accessed: 16-06-2025. 2

[5] S. Candel, M. Juniper, G. Singla, P. Scouflaire, and C. Rolon, "Structure and Dynamics of Cryogenic Flames at Supercritical Pressure," *Combustion Science and Technology*, vol. 178, no. 1-3, pp. 161–192, 2006. 1

[6] M. Foust, M. Deshpande, S. Pal, T. Ni, C. Merkle, and R. Santoro, "Experimental and Analytical Characterization of a Shear Coaxial Combusting GO2/GH2 Flowfield," in *34th Aerospace Sciences Meeting and Exhibit*, AIAA, 1996. 2

[7] D. T. Banuti and K. Hannemann, "Real Gas Library in Continuous Phase Propellant Injection Model for Liquid Rocket Engines," in *49th AIAA/ASME/SAE/ASEE Joint Propulsion Conference*, (San Jose, California, USA), AIAA, 2013. 2

[8] C.-A. Schley, G. Hagemann, P. Tucker, S. Venkateswaran, and C. L. Merkle, "Comparison of Computational Codes for Modeling Hydrogen-Oxygen Injectors," in *33rd AIAA/ASME/SAE/ASEE Joint Propulsion Conference and Exhibit*, (Seattle, Washington, USA), pp. 97–3302, American Institute of Aeronautics and Astronautics, 1997. 2

[9] S. R. Turns, *An Introduction to Combustion: Concepts and Applications*. New York, NY: McGraw-Hill, 2 ed., 2000. 2, 14, 21, 24, 27

[10] M. Habiballah, M. Orain, F. Grisch, L. Vingert, and P. Gicquel, "Experimental Studies of High-Pressure Cryogenic Flames on the Mascotte Facility," *Combustion Science and Technology*, vol. 178, no. 1-3, pp. 101–128, 2006. 2

[11] J. M. M. Barata, I. Gokalp, and A. R. R. Silva, "Numerical Study of Cryogenic Jets Under Supercritical Conditions," *Journal of Propulsion and Power*, vol. 19, no. 1, pp. 142–147, 2003. 2

[12] E. Antunes, A. Silva, and J. Barata, "Evaluation of Numerical Variable Density Approach to Cryogenic Jets," in *50th AIAA Aerospace Sciences Meeting Including the New Horizons Forum and Aerospace Exposition*, (Nashville, TN, USA), American Institute of Aeronautics and Astronautics, 2012. 2

[13] E. F. Antunes, A. R. Silva, and J. M. Barata, "RANS Modeling of Transcritical and Supercritical Nitrogen Jets," in *53rd AIAA Aerospace Sciences Meeting*, (Kissimmee, FL, USA), p. 0469, American Institute of Aeronautics and Astronautics, 2015. 2

[14] E. Antunes, A. Silva, and J. Barata, "Variable Density Approach for Modeling of Transcritical and Supercritical Jets," *Journal of Engineering and Applied Sciences*, vol. 12, no. 20, pp. 5147–5159, 2017. 2

[15] E. Antunes, A. Silva, and J. Barata, "Modelling of Transcritical and Supercritical Nitrogen Jets," *Combustion Engines*, vol. 169, no. 2, pp. 125–132, 2017. 2

[16] L. Magalhães, F. Carvalho, A. Silva, and J. Barata, "Turbulence Modeling Insights into Supercritical Nitrogen Mixing Layers," *Energies*, vol. 13, no. 7, p. 1586, 2020. 2

[17] L. Magalhães, F. Carvalho, A. Silva, and J. Barata, "Turbulence Quantification in Supercritical Nitrogen Injection: An Analysis of Turbulence Models," in *International Congress on Engineering – Engineering for Evolution (ICEUBI2019)*, pp. 356–367, Knowledge E, 2020. 2

[18] L. B. Magalhães, A. R. Silva, and J. M. Barata, "The Role of Injector Heat Transfer in Supercritical Injection Phenomena," in *AIAA Propulsion and Energy 2020 Forum*, (Virtual Event), p. 3658, American Institute of Aeronautics and Astronautics, 2020. 2

[19] L. B. Magalhães, A. R. Silva, and J. M. Barata, "Contribution to the Physical Description of Supercritical Cold Flow Injection: The Case of Nitrogen," *Acta Astronautica*, vol. 190, pp. 251–260, 2022. 3

[20] L. B. Magalhães, A. R. Silva, and J. M. Barata, "Supercritical Injection Modeling by an Incompressible but Variable Density Approach," *Aerospace*, vol. 10, no. 2, p. 114, 2023. 3

[21] J. R. d. S. Pedrosa, "Development of a Preliminary Framework for the Evaluation of Oxygen-Hydrogen Combustion Characteristics," Master's thesis, Universidade da Beira Interior, Covilhã, Portugal, 2023. 3

[22] G. P. Sutton and O. Biblarz, *Rocket Propulsion Elements*. John Wiley & Sons, 9 ed., 2016. 4, 5, 6, 7, 8

[23] S. Wassom, D. Lester, G. Farmer, and M. Holmes, "Solar Thermal Propulsion IHPRPT Demonstration Program Status," in *37th Joint Propulsion Conference and Exhibit*, (Salt Lake City, UT, USA), American Institute of Aeronautics and Astronautics, 2001. 4

[24] S. R. Oleson, R. M. Myers, C. A. Kluever, J. P. Riehl, and F. M. Curran, "Advanced Propulsion for Geostationary Orbit Insertion and North-South Station Keeping," *Journal of Spacecraft and Rockets*, vol. 34, no. 1, pp. 22–28, 1997. 4

[25] J. J. Rehder and K. E. Wurster, "Electric vs Chemical Propulsion for a Large-Cargo Orbit Transfer Vehicle," *Journal of Spacecraft and Rockets*, vol. 16, no. 3, pp. 129–134, 1979. 4

[26] R. V. Petrescu, R. Aversa, B. Akash, R. Bucinell, J. Corchado, A. Apicella, and F. I. Petrescu, "Modern Propulsions for Aerospace–A Review," *Journal of Aircraft and Spacecraft Technology*, vol. 1, no. 1, pp. 1–8, 2017. 4

[27] D. Thunnissen, C. Guernsey, R. Baker, and R. Miyake, "Advanced Space Storable Propellants for Outer Planet Exploration," 2004. 4

[28] O. J. Haidn, "Advanced rocket engines," in *Advances on Propulsion Technology for High-Speed Aircraft*, RTO-EN-AVT-150, pp. 6.1–6.40, Neuilly-sur-Seine, France: NATO Research and Technology Organisation, 2007. Presented at the RTO-AVT-VKI Lecture Series on "Advances on Propulsion Technology for High-Speed Aircraft", held in 2007. 4, 8, 9

[29] G. P. Sutton, *History of Liquid Propellant Rocket Engines*. American Institute of Aeronautics and Astronautics, 2006. 4

[30] NASA Glenn Research Center, "Brief History of Rockets." `https://www.grc.nasa.gov/www/k-12/TRC/Rockets/history_of_rockets.html`. Accessed: 16-05-2025. 4

[31] C. Bramanti, A. Cervone, and L. d'Agostino, "Assessment of the Propulsive Performance of Fuel Vapor Pressurized Hydrogen Peroxide-Ethane Rocket Engines," in *XVIII Congresso Nazionale AIDAA*, (Volterra, Italy), 2005. 7, 8

[32] M. Poschner and M. Pfitzner, "Real Gas CFD Simulation of Supercritical H2-LOX in the MASCOTTE Single Injector Combustor Using a Commercial CFD Code," in *46th AIAA Aerospace Sciences Meeting and Exhibit*, p. 952, 2008. 9

[33] A. Clifford and T. Clifford, *Fundamentals of Supercritical Fluids*. Oxford Science Publications, Oxford University Press, 1999. 9

[34] H. D. Baehr and S. Kabelac, *Thermodynamik: Eine Einführung in die Grundlagen und ihre technischen Anwendungen*. Springer-Lehrbuch, Springer, 9 ed., 1996. 10

[35] M. Wensing, T. Vogel, and G. Götz, "Transition of Diesel Spray to a Supercritical State under Engine Conditions," *International Journal of Engine Research*, vol. 17, no. 1, pp. 108–119, 2016. 11

[36] P. Coelho and M. Costa, *Combustão*. Lisboa, Portugal: Edições Orion, 2007. 13, 23, 24, 26, 31, 64, 66, 68

[37] S. Gordon and B. J. McBride, "Computer Program for Calculation of Complex Chemical Equilibrium Compositions, Rocket Performance, Incident and Reflected Shocks, and Chapman-Jouguet Detonations," NASA Special Publication NASA-SP-273, NASA Lewis Research Center, Cleveland, OH, USA, 1976. 16, 49, 75

[38] G. Indelicato, P. E. Lapenna, D. Durigon, and F. Creta, "Simulations of Turbulent Combustion and Wall Heat Transfer in Single and Multi Injectors GCH_4/GO_x Rocket Combustors," in *Proceedings of the 8th European Conference for Aeronautics and Space Sciences (EUCASS)*, (Madrid, Spain), European Aeronautics Science Network (EASN), 2019. 21

[39] C. K. Westbrook and F. L. Dryer, "Chemical Kinetic Modeling of Hydrocarbon Combustion," *Progress in Energy and Combustion Science*, vol. 10, no. 1, pp. 1–57, 1984. 23, 24, 26, 27, 36, 37, 40, 46

[40] M. C. Barbet and M. P. Burke, "Impact of "Missing" Third-Body Efficiencies on Kinetic Model Predictions of Combustion Properties," *Proceedings of the Combustion Institute*, vol. 38, no. 1, pp. 425–432, 2021. 24

[41] F. A. Lindemann, S. Arrhenius, I. Langmuir, N. R. Dhar, J. Perrin, and W. C. M. Lewis, "Discussion on "The Radiation Theory of Chemical Action"," *Transactions of the Faraday Society*, vol. 17, pp. 598–606, 1922. 29

[42] Reaction Design, *ANSYS Chemkin Theory Manual 17.0*. ANSYS, Inc., San Diego, CA, USA, 2016. Available from ANSYS Help Portal. 30, 31, 32

[43] J. Troe, "Thermal Dissociation and Recombination of Polyatomic Molecules," in *Proceedings of the 15th International Symposium on Combustion*, (Pittsburgh, PA, USA), pp. 667–679, The Combustion Institute, 1975. 31

[44] P. H. Stewart, C. W. Larson, and D. M. Golden, "Pressure and Temperature Dependence of Reactions Proceeding via a Bound Complex. II. Application to $2CH_3 \rightarrow C_2H_5 + H$," *Combustion and Flame*, vol. 75, no. 1, pp. 25–31, 1989. 32

[45] H. Pergament, "A Theoretical Analysis of Non-Equilibrium Hydrogen-Air Reactions in Flow Systems," in *Hypersonic Ramjet Conference*, (Cleveland, OH, USA), p. 113, American Institute of Aeronautics and Astronautics (AIAA), 1963. 36

[46] E. Spiegler, M. Wolfshtein, and Y. Manheimer-Timnat, "A Model of Unmixedness for Turbulent Reacting Flows," *Acta Astronautica*, vol. 3, no. 3–4, pp. 265–280, 1976. 36, 47

[47] C. J. Jachimowski, "An Analytical Study of the Hydrogen-Air Reaction Mechanism with Application to Scramjet Combustion," NASA Technical Publication NASA-TP-2791, NASA Langley Research Center, Hampton, VA, USA, 1988. 37, 44, 47, 48, 49, 58, 59

[48] C. K. Law, *Combustion Physics*. New York, NY, USA: Cambridge University Press, 2006. 39

[49] R. A. Yetter, F. L. Dryer, and H. Rabitz, "A Comprehensive Reaction Mechanism for Carbon Monoxide/Hydrogen/Oxygen Kinetics," *Combustion Science and Technology*, vol. 79, no. 1–3, pp. 97–128, 1991. 38, 39, 47, 48, 49, 50, 116

[50] N. Zettervall and C. Fureby, "A Computational Study of Ramjet, Scramjet and Dual-Mode Ramjet Combustion in a Combustor with a Cavity Flameholder," in *Proceedings of the AIAA Aerospace Sciences Meeting*, no. AIAA 2018-1146, (Kissimmee, FL, USA), American Institute of Aeronautics and Astronautics (AIAA), 2018. 38, 39, 48, 57, 59, 60, 125

[51] M. P. Burke, M. Chaos, Y. Ju, F. L. Dryer, and S. J. Klippenstein, "Comprehensive H_2/O_2 Kinetic Model for High-Pressure Combustion," *International Journal of Chemical Kinetics*, vol. 44, no. 7, pp. 444–474, 2012. 38, 39, 40, 42, 43, 44, 46, 48, 54, 55, 56, 57, 80, 122

[52] H. Hashemi, J. M. Christensen, S. Gersen, and P. Glarborg, "Hydrogen Oxidation at High Pressure and Intermediate Temperatures: Experiments and Kinetic Modeling," *Proceedings of the Combustion Institute*, vol. 35, no. 1, pp. 553–560, 2015. 39, 44, 45, 48, 56

[53] M. A. Mueller, T. J. Kim, R. A. Yetter, and F. L. Dryer, "Flow Reactor Studies and Kinetic Modeling of the H_2/O_2 Reaction," *International Journal of Chemical Kinetics*, vol. 31, no. 2, pp. 113–125, 1999. 39, 42, 44, 48, 50, 51, 60, 61, 79, 80, 81, 82, 84, 86, 88, 89, 94

[54] J. S. Evans and C. J. J. Schexnayder, "Influence of Chemical Kinetics and Unmixedness on Burning in Supersonic Hydrogen Flames," *AIAA Journal*, vol. 18, no. 2, pp. 188–193, 1980. 39, 47

[55] A. Kéromnès, W. K. Metcalfe, K. A. Heufer, N. Donohoe, A. K. Das, C.-J. Sung, J. Herzler, C. Naumann, P. Griebel, O. Mathieu, and E. L. Petersen, "An Experimental and Detailed Chemical Kinetic Modeling Study of Hydrogen and Syngas Mixture Oxidation at Elevated Pressures," *Combustion and Flame*, vol. 160, no. 6, pp. 995–1011, 2013. 40, 41, 42, 43, 44, 46, 48, 55, 56, 57, 58, 59, 60, 75, 79, 81, 93, 94, 123

[56] M. Ó Conaire, H. J. Curran, J. M. Simmie, W. J. Pitz, and C. K. Westbrook, "A Comprehensive Modeling Study of Hydrogen Oxidation," *International Journal of*

Chemical Kinetics, vol. 36, no. 11, pp. 603–622, 2004. 40, 42, 43, 47, 48, 50, 51, 52, 53, 54, 55, 56, 57, 59, 60, 70, 80, 81, 118

[57] J. Li, Z. Zhao, A. Kazakov, M. Chaos, F. L. Dryer, and J. J. Scire Jr., "A Comprehensive Kinetic Mechanism for CO, CH_2O, and CH_3OH Combustion," *International Journal of Chemical Kinetics*, vol. 39, no. 3, pp. 109–136, 2007. 40, 55, 56, 80

[58] A. A. Konnov, "Remaining Uncertainties in the Kinetic Mechanism of Hydrogen Combustion," *Combustion and Flame*, vol. 152, no. 4, pp. 507–528, 2008. 40, 42, 43, 44, 48, 51, 53, 54, 56, 57, 119

[59] Z. Hong, D. F. Davidson, and R. K. Hanson, "An Improved H_2/O_2 Mechanism Based on Recent Shock Tube/Laser Absorption Measurements," *Combustion and Flame*, vol. 158, no. 4, pp. 633–644, 2011. 40, 41, 42, 43, 44, 48, 52, 55, 56, 57, 59, 120

[60] K. Shimizu, A. Hibi, M. Koshi, Y. Morii, and N. Tsuboi, "Updated Kinetic Mechanism for High-Pressure Hydrogen Combustion," *Journal of Propulsion and Power*, vol. 27, no. 2, pp. 383–395, 2011. 40, 41, 42, 43, 44, 48, 53, 57, 94, 121

[61] H. Hippler, H. Neunaber, and J. Troe, "Shock Wave Studies of the Reactions HO + $H_2O_2 \rightarrow H_2O + HO_2$ and HO + $HO_2 \rightarrow H_2O + O_2$ Between 930 and 1680 K," *The Journal of Chemical Physics*, vol. 103, no. 9, pp. 3510–3516, 1995. 42, 43

[62] C. Kappel, K. Luther, and J. Troe, "Shock Wave Study of the Unimolecular Dissociation of H_2O_2 in Its Falloff Range and of Its Secondary Reactions," *Physical Chemistry Chemical Physics*, vol. 4, no. 18, pp. 4392–4398, 2002. 42, 43

[63] Z. Hong, S. S. Vasu, D. F. Davidson, and R. K. Hanson, "Experimental Study of the Rate of OH + $HO_2 \rightarrow H_2O + O_2$ at High Temperatures Using the Reverse Reaction," *The Journal of Physical Chemistry A*, vol. 114, no. 17, pp. 5520–5525, 2010. 42, 53, 54

[64] N. K. Srinivasan, M.-C. Su, J. W. Sutherland, J. V. Michael, and B. Ruscic, "Reflected Shock Tube Studies of High-Temperature Rate Constants for OH + $NO_2 \rightarrow$ HO_2 + NO and OH + $HO_2 \rightarrow H_2O + O_2$," *The Journal of Physical Chemistry A*, vol. 110, no. 21, pp. 6602–6607, 2006. 42

[65] J. Li, Z. Zhao, A. Kazakov, and F. L. Dryer, "An Updated Comprehensive Kinetic Model of Hydrogen Combustion," *International Journal of Chemical Kinetics*, vol. 36, no. 10, pp. 566–575, 2004. 42, 43, 47, 48, 50, 52, 53, 54, 55, 60, 117

[66] V. A. Alekseev, M. Christensen, and A. A. Konnov, "The Effect of Temperature on the Adiabatic Burning Velocities of Diluted Hydrogen Flames: A Kinetic Study Using an Updated Mechanism," *Combustion and Flame*, vol. 162, no. 5, pp. 1884–1898, 2015. 42, 43, 48, 57, 58

[67] R. R. Baldwin, M. E. Fuller, J. S. Hillman, D. Jackson, and R. W. Walker, "Second Limit of Hydrogen + Oxygen Mixtures: The Reaction H + HO_2," *Journal of the Chemical Society, Faraday Transactions 1: Physical Chemistry in Condensed Phases*, vol. 70, pp. 635–641, 1974. 42

[68] M. J. Day, K. Thompson, and G. Dixon-Lewis, "Some Reactions of Hydroperoxyl and Hydroxyl Radicals at High Temperatures," in *Proceedings of the 14th Symposium (International) on Combustion*, vol. 14, pp. 47–59, Elsevier, 1973. 42

[69] Z. Hong, R. D. Cook, D. F. Davidson, and R. K. Hanson, "A Shock Tube Study of OH + $H_2O_2 \rightarrow H_2O$ + HO_2 and H_2O_2 + M $\rightarrow$ 2OH + M Using Laser Absorption of H_2O and OH," *The Journal of Physical Chemistry A*, vol. 114, no. 18, pp. 5718–5727, 2010. 43, 53

[70] H. Sun, S. I. Yang, G. Jomaas, and C. K. Law, "High-Pressure Laminar Flame Speeds and Kinetic Modeling of Carbon Monoxide/Hydrogen Combustion," *Proceedings of the Combustion Institute*, vol. 31, no. 1, pp. 439–446, 2007. 43, 56

[71] S. G. Davis, A. V. Joshi, H. Wang, and F. Egolfopoulos, "An Optimized Kinetic Model of H_2/CO Combustion," *Proceedings of the Combustion Institute*, vol. 30, no. 1, pp. 1283–1292, 2005. 43, 48, 51, 54, 55, 56, 57, 59

[72] R. Oldenborg, W. Chinitz, M. Friedman, R. Jaffe, C. Jachimowski, M. Rabinowitz, and G. Schott, "Hypersonic Combustion Kinetics: Status Report of the Rate Constant Committee, NASP High Speed Propulsion Technology Team," Technical Memorandum NASP TM-1107, NASP Rate Constant Committee, 1990. 44, 49

[73] J. V. Michael, J. W. Sutherland, L. B. Harding, and A. F. Wagner, "Initiation in H2/O2: Rate Constants for H2 + O2 $\rightarrow$ H + HO2 at High Temperature," *Proceedings of the Combustion Institute*, vol. 28, no. 2, pp. 1471–1478, 2000. 44

[74] G. J. Wilson and R. W. MacCormack, "Modeling Supersonic Combustion Using a Fully Implicit Numerical Method," *AIAA Journal*, vol. 30, no. 4, pp. 1008–1015, 1992. 44, 48, 49, 115

[75] R. J. Kee, F. M. Rupley, J. A. Miller, M. E. Coltrin, J. F. Grcar, E. Meeks, H. K. Moffat, A. E. Lutz, G. Dixon-Lewis, M. D. Smooke, J. Warnatz, G. H. Evans, R. S. Larson, R. E. Mitchell, L. R. Petzold, W. C. Reynolds, M. Caracotsios, W. E. Stewart, P. Glarborg, C. Wang, C. L. McLellan, O. Adigun, W. G. Houf, C. P. Chou, S. F. Miller, P. Ho, P. D. Young, D. J. Young, D. W. Hodgson, M. V. Petrova, and K. V. Puduppakkam, *CHEMKIN Collection, Release 4.1.1.* Reaction Design, San Diego, CA, 2007. 46, 55

[76] H. Wang, X. You, A. V. Joshi, S. G. Davis, A. Laskin, F. Egolfopoulos, and C. K. Law, "High-Temperature Combustion Reaction Model of H_2/CO/C1–C4 Compounds,

USC Mech Version II." https://ignis.usc.edu/about.html, 2007. Accessed: 17-06-2025. 46, 55, 59, 60

[77] R. J. Kee, G. Dixon-Lewis, J. Warnatz, M. E. Coltrin, and J. A. Miller, "A Fortran Computer Code Package for the Evaluation of Gas-Phase Multicomponent Transport Properties," Tech. Rep. SAND86-8246, Sandia National Laboratories, Livermore, CA, 1986. Prepared under DOE Contract No. AC04-76DR00789. 46

[78] L. S. Kassel, "The Mechanism of the Combustion of Hydrogen," *Chemical Reviews*, vol. 21, no. 2, pp. 331–345, 1937. 46

[79] D. L. Baulch, D. D. Drysdale, D. G. Horne, and A. C. Lloyd, *Evaluated Kinetic Data for High Temperature Reactions, Volume 1: Homogeneous Gas Phase Reactions of the H2-O2 System*. London: Butterworths, 1972. 46

[80] W. C. J. Gardiner and D. B. Olson, "Chemical Kinetics of High Temperature Combustion," *Annual Review of Physical Chemistry*, vol. 31, no. 1, pp. 377–399, 1980. 46

[81] T. J. Kim, R. A. Yetter, and F. L. Dryer, "New Results on Moist CO Oxidation: High Pressure, High Temperature Experiments and Comprehensive Kinetic Modeling," in *Proceedings of the 25th Symposium (International) on Combustion*, vol. 25, (Pittsburgh, PA), pp. 759–766, The Combustion Institute, 1994. 48, 50, 51

[82] G. P. Smith, D. M. Golden, M. Frenklach, N. W. Moriarty, B. Eiteneer, M. Goldenberg, C. T. Bowman, R. K. Hanson, S. Song, W. C. J. Gardiner, V. V. Lissianski, and Z. Qin, "GRI-Mech 3.0: An Optimized Detailed Chemical Reaction Mechanism for Methane Combustion." http://combustion.berkeley.edu/gri-mech/version30/text30.html, 1999. Accessed: 17-06-2025. 48, 50, 51, 52, 53, 56, 58, 59, 60, 70, 73

[83] A. A. Konnov, "Refinement of the Kinetic Mechanism of Hydrogen Combustion," *Chemical Physics (Химическая физика)*, vol. 23, no. 8, pp. 5–18, 2004. 48, 52

[84] S. Kitano, M. Fukao, A. Susa, N. Tsuboi, A. K. Hayashi, and M. Koshi, "Spinning Detonation and Velocity Deficit in Small Diameter Tubes," *Proceedings of the Combustion Institute*, vol. 32, no. 2, pp. 2355–2362, 2009. 48, 53

[85] T. Varga, T. Nagy, C. Olm, I. G. Zsély, R. Pálvölgyi, É. Valkó, G. Vincze, M. Cserháti, H. J. Curran, and T. Turányi, "Optimization of a Hydrogen Combustion Mechanism Using Both Direct and Indirect Measurements," *Proceedings of the Combustion Institute*, vol. 35, no. 1, pp. 589–596, 2015. 48, 56, 124

[86] D. R. Stull and H. Prophet, *JANAF Thermochemical Tables, Second Edition*. Washington, DC: American Chemical Society, 1971. Prepared by the Dow Chemical Co., Thermal Laboratory, Midland, MI. 49

[87] W. C. Gardiner and A. Burcat, *Combustion Chemistry*. New York: Springer-Verlag, 1984. 49

[88] P. Gerlinger, H. Möbus, and D. Brüggemann, "An Implicit Multigrid Method for Turbulent Combustion," *Journal of Computational Physics*, vol. 167, no. 2, pp. 247–276, 2001. 49

[89] M. W. Chase, J. L. Curnutt, J. R. Downey, R. A. McDonald, A. N. Syverud, and E. A. Valenzuela, "JANAF Thermochemical Tables, Third Edition, Supplement I," *Journal of Physical and Chemical Reference Data*, vol. 14, no. Supplement 1, pp. 1–1856, 1982. 49

[90] A. J. Hills and C. J. Howard, "Rate Coefficient Temperature Dependence and Branching Ratio for the OH+ClO Reaction," *The Journal of Chemical Physics*, vol. 81, no. 10, pp. 4458–4465, 1984. 49, 50

[91] R. J. Kee, F. M. Rupley, and J. A. Miller, "The CHEMKIN Thermodynamic Data Base," Technical Report SAND87-8215, Sandia National Laboratories, Livermore, CA, 1987. Available from Sandia National Laboratories. 49, 50

[92] E. R. Ritter and J. W. Bozzelli, "THERM: Thermodynamic Property Estimation for Radicals and Molecules," Technical Report, Department of Chemical Engineering, Chemistry, and Environmental Science, New Jersey Institute of Technology, Newark, NJ, 1987. Internal Report. 49

[93] B. Ruscic, A. F. Wagner, L. B. Harding, R. L. Asher, D. Feller, D. A. Dixon, K. A. Peterson, Y. Song, X. Qian, C.-Y. Ng, J. Liu, W. Chen, and D. W. Schwenke, "On the Enthalpy of Formation of Hydroxyl Radical and Gas-Phase Bond Dissociation Energies of Water and Hydroxyl," *The Journal of Physical Chemistry A*, vol. 106, no. 11, pp. 2727–2747, 2002. 50, 55

[94] G. P. Smith, "Diagnostics for Detailed Kinetic Modeling," in *Applied Combustion Diagnostics* (K. Kohse-Höinghaus and J. B. Jefferies, eds.), pp. 693–744, Boca Raton, FL: CRC Press, 2002. 50

[95] J. T. Herbon, R. K. Hanson, D. M. Golden, and C. T. Bowman, "A Shock Tube Study of the Enthalpy of Formation of OH," *Proceedings of the Combustion Institute*, vol. 29, no. 1, pp. 1201–1208, 2002. 50, 55

[96] S. G. Davis, A. V. Joshi, H. Wang, and F. N. Egolfopoulos, "A Comprehensive and Optimized Kinetic Model of H_2/CO Combustion," in *Proceedings of the Third Joint Meeting of the U.S. Sections of the Combustion Institute*, (Chicago, IL), 2003. 50

[97] M. W. Slack, "Rate Coefficient for H + O_2 + M = HO_2 + M Evaluated from Shock Tube Measurements of Induction Times," *Combustion and Flame*, vol. 28, pp. 241–249, 1977. 50, 52

[98] S. D. Tse, D. L. Zhu, and C. K. Law, "Morphology and Burning Rates of Expanding Spherical Flames in H_2/O_2/Inert Mixtures up to 60 Atmospheres," *Proceedings of the Combustion Institute*, vol. 28, no. 2, pp. 1793–1800, 2000. 50, 51, 60

[99] A. A. Konnov, "Detailed Reaction Mechanism for Small Hydrocarbons Combustion: Release 0.5." `http://homepages.vub.ac.be/~akonnov/`, 2000. Accessed: 17-06-2025. 50, 52

[100] K. J. Hughes, T. Turányi, A. R. Clague, and M. J. Pilling, "Development and Testing of a Comprehensive Chemical Mechanism for the Oxidation of Methane," *International Journal of Chemical Kinetics*, vol. 33, no. 9, pp. 513–538, 2001. 50, 59

[101] D. R. Dowdy, D. B. Smith, S. C. Taylor, and A. Williams, "The use of expanding spherical flames to determine burning velocities and stretch effects in hydrogen/air mixtures," in *Twenty-Third Symposium (International) on Combustion*, vol. 23, pp. 325–332, Elsevier, The Combustion Institute, 1990. 51

[102] F. N. Egolfopoulos and C. K. Law, "An Experimental and Computational Study of the Burning Rates of Ultra-Lean to Moderately-Rich $H_2/O_2/N_2$ Laminar Flames with Pressure Variations," in *Proceedings of the 23rd Symposium (International) on Combustion*, vol. 23, (Pittsburgh, PA), pp. 333–340, The Combustion Institute, 1991. 51, 53

[103] C. M. Vagelopoulos, F. N. Egolfopoulos, and C. K. Law, "Further Considerations on the Determination of Laminar Flame Speeds with the Counterflow Twin-Flame Technique," in *Proceedings of the Combustion Institute*, vol. 25, pp. 1341–1347, Elsevier, 1994. 51

[104] O. C. Kwon and G. M. Faeth, "Flame/Stretch Interactions of Premixed Hydrogen-Fueled Flames: Measurements and Predictions," *Combustion and Flame*, vol. 124, no. 4, pp. 590–610, 2001. 51

[105] I. C. McLean, D. B. Smith, and S. C. Taylor, "The Use of Carbon Monoxide/Hydrogen Burning Velocities to Examine the Rate of the CO + OH Reaction," in *Proceedings of the Combustion Institute*, vol. 25, pp. 749–757, Elsevier, 1994. 51

[106] C. M. Vagelopoulos and F. N. Egolfopoulos, "Laminar Flame Speeds and Extinction Strain Rates of Mixtures of Carbon Monoxide with Hydrogen, Methane, and Air," in *Proceedings of the 25th Symposium (International) on Combustion*, vol. 25, (Pittsburgh, PA), pp. 1317–1323, The Combustion Institute, 1994. 51

[107] J. Vandooren and J. Bian, "Validation of H_2/O_2 Reaction Mechanisms by Comparison with the Experimental Structure of a Rich Hydrogen-Oxygen Flame," in *Proceedings of the Combustion Institute*, vol. 23, pp. 341–346, Elsevier, 1991. 51, 53

[108] R. K. Cheng and A. K. Oppenheim, "Autoignition in Methane Hydrogen Mixtures," *Combustion and Flame*, vol. 58, no. 2, pp. 125–139, 1984. 51

[109] A. Cohen and J. Larsen, "Explosive Mechanism of the H_2-O_2 Reaction Near the Second Ignition Limit," Tech. Rep. BRL-1386, Ballistic Research Laboratories, Aberdeen Proving Ground, Maryland, 1967. 51

[110] E. L. Petersen, D. F. Davidson, M. Röhrig, and R. K. Hanson, "High-Pressure Shock-Tube Measurements of Ignition Times in Stoichiometric H_2/O_2/Ar Mixtures," in *Proceedings of the 20th International Symposium on Shock Waves*, pp. 941–946, Springer, 1995. 51

[111] A. M. Dean, D. C. Steiner, and E. E. Wang, "A Shock Tube Study of the H_2/O_2/CO/Ar and H_2/N_2O/CO/Ar Systems: Measurement of the Rate Constant for H + N_2O = N_2 + OH," Tech. Rep. UMO-2-PU, Department of Chemistry, University of Missouri–Columbia, Columbia, Missouri, 1977. Project SQUID Technical Report. 51

[112] R. J. Kee, F. M. Rupley, J. A. Miller, M. E. Coltrin, J. F. Grcar, E. Meeks, H. K. Moffat, A. E. Lutz, G. Dixon-Lewis, M. D. Smooke, *et al.*, "CHEMKIN Collection, Release 3.6," Technical Report, Reaction Design, San Diego, California, 2000. 51, 52

[113] A. Burcat and B. Ruscic, "Third Millennium Ideal Gas and Condensed Phase Thermochemical Database for Combustion (with Update from Active Thermochemical Tables)," Technical Report, Argonne National Laboratory, Argonne, IL, United States, 2005. 51, 52, 55, 75

[114] A. D. Snyder, J. Robertson, D. L. Zanders, and G. B. Skinner, "Shock Tube Studies of Fuel-Air Ignition Characteristics," Technical Report AFAPL-TR-65-93, Monsanto Research Corporation, Dayton, OH, United States, 1965. 52, 59

[115] K. T. Aung, M. I. Hassan, and G. M. Faeth, "Flame Stretch Interactions of Laminar Premixed Hydrogen/Air Flames at Normal Temperature and Pressure," *Combustion and Flame*, vol. 109, no. 1–2, pp. 1–24, 1997. 52

[116] K. T. Aung, M. I. Hassan, and G. M. Faeth, "Effects of Pressure and Nitrogen Dilution on Flame/Stretch Interactions of Laminar Premixed $H_2/O_2/N_2$ Flames," *Combustion and Flame*, vol. 112, no. 1–2, pp. 1–15, 1998. 52, 60

[117] A. A. Paletskii, L. V. Kuibida, T. A. Bolshova, O. P. Korobeinichev, and R. M. Fristrom, "Study of the Structure of a Ten-Atmosphere H_2-O_2-Ar Flame Using Molecular-Beam Inlet Mass-Spectrometric Probing," *Combustion, Explosion, and Shock Waves*, vol. 32, pp. 245–250, 1996. 52, 53

[118] D. L. Baulch, C. T. Bowman, C. J. Cobos, R. A. Cox, T. Just, J. A. Kerr, M. J. Pilling, D. Stocker, J. Troe, W. Tsang, R. W. Walker, and J. Warnatz, "Evaluated Kinetic

Data for Combustion Modeling: Supplement II," *Journal of Physical and Chemical Reference Data*, vol. 34, no. 3, pp. 757–1397, 2005. 52

[119] Z. Hong, D. F. Davidson, E. A. Barbour, and R. K. Hanson, "A New Shock Tube Study of the H + O_2 → OH + O Reaction Rate Using Tunable Diode Laser Absorption of H_2O Near 2.5 μm," *Proceedings of the Combustion Institute*, vol. 33, no. 1, pp. 309–316, 2011. 53

[120] D. A. Masten, R. K. Hanson, and C. T. Bowman, "Shock Tube Study of the Reaction H + O_2 → OH + O Using OH Laser Absorption," *Journal of Physical Chemistry*, vol. 94, no. 18, pp. 7119–7128, 1990. 53

[121] R. T. E. Hermanns, A. A. Konnov, R. J. M. Bastiaans, and L. P. H. de Goey, "Laminar Burning Velocities of Diluted Hydrogen–Oxygen–Nitrogen Mixtures," *Energy & Fuels*, vol. 21, no. 4, pp. 1977–1981, 2007. 53

[122] F. N. Egolfopoulos and C. K. Law, "Chain Mechanisms in the Overall Reaction Orders in Laminar Flame Propagation," *Combustion and Flame*, vol. 80, no. 1, pp. 7–16, 1990. 53

[123] M. P. Burke, M. Chaos, F. L. Dryer, and Y. Ju, "Negative Pressure Dependence of Mass Burning Rates of H_2/CO/O_2/Diluent Flames at Low Flame Temperatures," *Combustion and Flame*, vol. 157, no. 4, pp. 618–631, 2010. 53, 54

[124] G. Dixon-Lewis, M. M. Sutton, and A. Williams, "Flame Structure and Flame Reaction Kinetics-IV. Experimental Investigations of a Fuel-Rich Hydrogen+Oxygen+Nitrogen Flame at Atmospheric Pressure," *Proceedings of the Royal Society of London. A. Mathematical and Physical Sciences*, vol. 317, no. 1529, pp. 227–234, 1970. 53

[125] E. Hu, L. Pan, Z. Gao, X. Lu, X. Meng, and Z. Huang, "Shock Tube Study on Ignition Delay of Hydrogen and Evaluation of Various Kinetic Models," *International Journal of Hydrogen Energy*, vol. 41, no. 30, pp. 13261–13280, 2016. 54, 59, 60

[126] G. Mittal, C.-J. Sung, and R. A. Yetter, "Autoignition of H_2/CO at Elevated Pressures in a Rapid Compression Machine," *International Journal of Chemical Kinetics*, vol. 38, no. 8, pp. 516–529, 2006. 55

[127] T. Le Cong and P. Dagaut, "Experimental and Detailed Modeling Study of the Effect of Water Vapor on the Kinetics of Combustion of Hydrogen and Natural Gas, Impact on NO_x," *Energy & Fuels*, vol. 23, no. 2, pp. 725–734, 2009. 55

[128] G. Bagheri, E. Ranzi, M. Pelucchi, A. Parente, A. Frassoldati, and T. Faravelli, "Comprehensive Kinetic Study of Combustion Technologies for Low Environmental Impact: MILD and OXY-Fuel Combustion of Methane," *Combustion and Flame*, vol. 212, pp. 142–155, 2020. 56, 58

[129] S. Gersen, H. Darmeveil, and H. Levinsky, "The Effects of CO Addition on the Autoignition of H_2, CH_4 and CH_4/H_2 Fuels at High Pressure in an RCM," *Combustion and Flame*, vol. 159, no. 12, pp. 3472–3475, 2012. 57

[130] J. Herzler and C. Naumann, "Shock-Tube Study of the Ignition of Methane/Ethane/Hydrogen Mixtures with Hydrogen Contents from 0% to 100% at Different Pressures," *Proceedings of the Combustion Institute*, vol. 32, no. 1, pp. 213–220, 2009. 57, 59, 60

[131] E. Goos, A. Burcat, and B. Ruscic, *Extended Third Millennium Ideal Gas and Condensed Phase Thermochemical Database for Combustion with Updates from Active Thermochemical Tables*. Argonne National Laboratory and Technion – Israel Institute of Technology, 2010. 57

[132] A. V. Ivanov, S. Trakhtenberg, A. K. Bertram, Y. M. Gershenzon, and M. J. Molina, "OH, HO_2, and Ozone Gaseous Diffusion Coefficients," *The Journal of Physical Chemistry A*, vol. 111, no. 9, pp. 1632–1637, 2007. 57

[133] C. Olm, I. G. Zsély, R. Pálvölgyi, T. Varga, T. Nagy, H. J. Curran, and T. Turányi, "Comparison of the Performance of Several Recent Hydrogen Combustion Mechanisms," *Combustion and Flame*, vol. 161, no. 9, pp. 2219–2234, 2014. 57

[134] A. Larsson, N. Zettervall, T. Hurtig, E. J. K. Nilsson, A. Ehn, P. Petersson, M. Aldén, J. Larfeldt, and C. Fureby, "Skeletal Methane–Air Reaction Mechanism for Large Eddy Simulation of Turbulent Microwave-Assisted Combustion," *Energy & Fuels*, vol. 31, no. 2, pp. 1904–1926, 2017. 57

[135] D. Davidenko, I. Gökalp, E. Dufour, and P. Magre, "Numerical Simulation of Hydrogen Supersonic Combustion and Validation of Computational Approach," in *12th AIAA International Space Planes and Hypersonic Systems and Technologies*, (Norfolk, VA, USA), American Institute of Aeronautics and Astronautics, 2003. 58

[136] N. M. Marinov, C. K. Westbrook, and W. J. Pitz, "Detailed and Global Chemical Kinetics Model for Hydrogen," in *Transport Phenomena in Combustion*, vol. 1, pp. 118–129, Abingdon, UK: Taylor & Francis, 1996. 58

[137] E. Ranzi, A. Frassoldati, S. Granata, and T. Faravelli, "Wide-Range Kinetic Modeling Study of the Pyrolysis, Partial Oxidation, and Combustion of Heavy n-Alkanes," *Industrial & Engineering Chemistry Research*, vol. 44, no. 14, pp. 5170–5183, 2005. 58

[138] E. Ranzi, A. Frassoldati, A. Stagni, M. Pelucchi, A. Cuoci, and T. Faravelli, "Reduced Kinetic Schemes of Complex Reaction Systems: Fossil and Biomass-Derived Transportation Fuels," *International Journal of Chemical Kinetics*, vol. 46, no. 9, pp. 512–542, 2014. 58, 59

[139] A. Frassoldati, T. Faravelli, and E. Ranzi, "A Wide Range Modeling Study of NOx Formation and Nitrogen Chemistry in Hydrogen Combustion," *International Journal of Hydrogen Energy*, vol. 31, no. 15, pp. 2310–2328, 2006. 58, 59, 60

[140] E. Ranzi, C. Cavallotti, A. Cuoci, A. Frassoldati, M. Pelucchi, and T. Faravelli, "New Reaction Classes in the Kinetic Modeling of Low Temperature Oxidation of n-Alkanes," *Combustion and Flame*, vol. 162, no. 5, pp. 1679–1691, 2015. 58

[141] E. Ranzi, A. Frassoldati, R. Grana, A. Cuoci, T. Faravelli, A. P. Kelley, and C. K. Law, "Hierarchical and Comparative Kinetic Modeling of Laminar Flame Speeds of Hydrocarbon and Oxygenated Fuels," *Progress in Energy and Combustion Science*, vol. 38, no. 4, pp. 468–501, 2012. 58

[142] M. Pelucchi, C. Cavallotti, T. Faravelli, and S. J. Klippenstein, "H-Abstraction Reactions by OH, HO_2, O, O_2 and Benzyl Radical Addition to O_2 and Their Implications for Kinetic Modelling of Toluene Oxidation," *Physical Chemistry Chemical Physics*, vol. 20, no. 16, pp. 10607–10627, 2018. 58

[143] M. Pelucchi, M. Bissoli, C. Cavallotti, A. Cuoci, T. Faravelli, A. Frassoldati, E. Ranzi, and A. Stagni, "Improved Kinetic Model of the Low-Temperature Oxidation of n-Heptane," *Energy & Fuels*, vol. 28, no. 11, pp. 7178–7193, 2014. 58

[144] M. Pelucchi, C. Cavallotti, E. Ranzi, A. Frassoldati, and T. Faravelli, "Relative Reactivity of Oxygenated Fuels: Alcohols, Aldehydes, Ketones, and Methyl Esters," *Energy & Fuels*, vol. 30, no. 10, pp. 8665–8679, 2016. 58

[145] W. Pejpichestakul, E. Ranzi, M. Pelucchi, A. Frassoldati, A. Cuoci, A. Parente, and T. Faravelli, "Examination of a Soot Model in Premixed Laminar Flames at Fuel-Rich Conditions," *Proceedings of the Combustion Institute*, vol. 37, no. 1, pp. 1013–1021, 2019. 58

[146] P. di Milano CRECK Modeling Group, "Detailed Kinetic Mechanisms." `https://www.creckmodeling.polimi.it/menu-kinetics/menu-kinetics-detailed-mechanisms/`, 2025. Accessed: 24-01-2025. 58

[147] Y. Li, C.-W. Zhou, K. P. Somers, K. Zhang, and H. J. Curran, "The Oxidation of 2-Butene: A High Pressure Ignition Delay, Kinetic Modeling Study and Reactivity Comparison with Isobutene and 1-Butene," *Proceedings of the Combustion Institute*, vol. 36, no. 1, pp. 403–411, 2017. 58

[148] C.-W. Zhou, Y. Li, E. O'Connor, K. P. Somers, S. Thion, C. Keesee, O. Mathieu, E. L. Petersen, T. A. DeVerter, M. A. Oehlschlaeger, *et al.*, "A Comprehensive Experimental and Modeling Study of Isobutene Oxidation," *Combustion and Flame*, vol. 167, pp. 353–379, 2016. 58

[149] U. Burke, W. K. Metcalfe, S. M. Burke, K. A. Heufer, P. Dagaut, and H. J. Curran, "A Detailed Chemical Kinetic Modeling, Ignition Delay Time and Jet-Stirred Reactor

Study of Methanol Oxidation," *Combustion and Flame*, vol. 165, pp. 125–136, 2016. 58

[150] S. M. Burke, U. Burke, R. McDonagh, O. Mathieu, I. Osorio, C. Keesee, A. Morones, E. L. Petersen, W. Wang, T. A. DeVerter, *et al.*, "An Experimental and Modeling Study of Propene Oxidation. Part 2: Ignition Delay Time and Flame Speed Measurements," *Combustion and Flame*, vol. 162, no. 2, pp. 296–314, 2015. 58

[151] S. M. Burke, W. Metcalfe, O. Herbinet, F. Battin-Leclerc, F. M. Haas, J. Santner, F. L. Dryer, and H. J. Curran, "An Experimental and Modeling Study of Propene Oxidation. Part 1: Speciation Measurements in Jet-Stirred and Flow Reactors," *Combustion and Flame*, vol. 161, no. 11, pp. 2765–2784, 2014. 58

[152] W. K. Metcalfe, S. M. Burke, S. S. Ahmed, and H. J. Curran, "A Hierarchical and Comparative Kinetic Modeling Study of C1–C2 Hydrocarbon and Oxygenated Fuels," *International Journal of Chemical Kinetics*, vol. 45, no. 10, pp. 638–675, 2013. 58

[153] N. U. of Ireland Galway, "AramcoMech 2.0." `https://www.universityofgalway.ie/combustionchemistrycentre/mechanismdownloads/aramcomech20/`, 2025. Accessed: 24-01-2025. 59, 60

[154] U. of California San Diego, "Chemical Mechanism: Combustion Research Group at UC San Diego." `http://web.eng.ucsd.edu/mae/groups/combustion/mechanism.html`, 2025. Accessed: 24-01-2025. 59

[155] G. Saccone, P. Natale, L. Cutrone, and M. Marini, "Hydrogen/Air Supersonic Combustion Modelling and Validation for Scramjet Applications," *Journal of Fluid Flow, Heat and Mass Transfer*, vol. 9, 2022. 59, 60

[156] R. R. Craig, "A Shock Tube Study of the Ignition Delay of Hydrogen-Air Mixtures Near the Second Explosion Limit," Master's thesis, The Ohio State University, 1966. Also published as Technical Report AFAPL-TR-66-74, Air Force Aero Propulsion Laboratory, Wright-Patterson Air Force Base, Ohio. 59

[157] B. L. Wang, H. Olivier, and H. Grönig, "Ignition of Shock-Heated H_2-Air-Steam Mixtures," *Combustion and Flame*, vol. 133, no. 1–2, pp. 93–106, 2003. 59

[158] D. J. Beerer and V. G. McDonell, "Autoignition of Hydrogen and Air Inside a Continuous Flow Reactor with Application to Lean Premixed Combustion," *Journal of Engineering for Gas Turbines and Power*, vol. 130, no. 6, p. 051507, 2008. 59

[159] G. Saccone and M. Marini, "High Pressure Hydrogen Oxygen Combustion Kinetic Assessment for Air-Breathing Propulsion Supersonic Green Aviation," in *Proceedings of the 33rd Congress of the International Council of the Aeronautical Sciences (ICAS)*, (Stockholm, Sweden), ICAS, 2022. 59, 60

[160] E. Peterson, M. Krejci, O. Mathieu, A. Vissotski, S. Ravi, T. Sikes, A. Levacque, and C. Aul, "Turbulent Flame Speeds and NOx Kinetics of HHC Fuels with Contaminants and High Dilution Levels," Technical Report DOE/FE0004679, Texas A&M Engineering Experiment Station, College Station, TX, United States, 2011. 59, 60

[161] G. Saccone, P. Natale, L. Cutrone, and M. Marini, "Kinetic Analysis and CFD Modelling of Hydrogen-Air Combustion Applied to Scramjet Vehicles," in *Proceedings of the 7th World Congress on Momentum, Heat and Mass Transfer (MHMT'22)*, (Lisbon, Portugal), International ASET Inc., 2022. Best Paper Award. 59, 60

[162] G. Saccone and M. Marini, "Chemical Kinetic Analysis of High-Pressure Hydrogen Ignition and Combustion toward Green Aviation," *Aerospace*, vol. 11, no. 2, p. 112, 2024. 60

[163] M. C. Krejci, O. Mathieu, A. J. Vissotski, S. Ravi, T. G. Sikes, E. L. Petersen, A. Kérmonès, W. Metcalfe, and H. J. Curran, "Laminar Flame Speed and Ignition Delay Time Data for the Kinetic Modeling of Hydrogen and Syngas Fuel Blends," *Journal of Engineering for Gas Turbines and Power*, vol. 135, no. 2, p. 021503, 2013. 60

[164] S. D. Cohen, A. C. Hindmarsh, and P. F. Dubois, "CVODE, a Stiff/Nonstiff ODE Solver in C," *Computers in Physics*, vol. 10, no. 2, pp. 138–143, 1996. 67, 68, 70, 72, 73

[165] C. P. Stone and F. Bisetti, "Comparison of ODE Solver for Chemical Kinetics and Reactive CFD Applications," in *52nd AIAA Aerospace Sciences Meeting*, (National Harbor, Maryland), pp. AIAA 2014–0822, American Institute of Aeronautics and Astronautics, 2014. 67, 68, 69, 73

[166] R. L. Burden and J. D. Faires, *Numerical Analysis, 9th Edition*. Boston, MA: Brooks/Cole, Cengage Learning, 2010. 68

[167] K. Radhakrishnan, "LSENS: A General Chemical Kinetics and Sensitivity Analysis Code for Homogeneous Gas-Phase Reactions. Part 1: Theory and Numerical Solution Procedures," Tech. Rep. NASA-RP-1328, NASA Lewis Research Center, Cleveland, OH, United States, 1994. 68, 69

[168] M. J. McNenly, R. A. Whitesides, and D. L. Flowers, "Faster Solvers for Large Kinetic Mechanisms Using Adaptive Preconditioners," *Proceedings of the Combustion Institute*, vol. 35, no. 1, pp. 581–587, 2015. 70, 73, 77

[169] P. N. Brown and A. C. Hindmarsh, "Reduced Storage Matrix Methods in Stiff ODE Systems," *Applied Mathematics and Computation*, vol. 31, pp. 40–91, 1989. 70, 71

[170] P. N. Brown, A. C. Hindmarsh, and L. R. Petzold, "Using Krylov Methods in the Solution of Large-Scale Differential-Algebraic Systems," *SIAM Journal on Scientific Computing*, vol. 15, no. 6, pp. 1467–1488, 1994. 70, 71

[171] P. N. Brown and A. C. Hindmarsh, "Matrix-Free Methods for Stiff Systems of ODEs," *SIAM Journal on Numerical Analysis*, vol. 23, no. 3, pp. 610–638, 1986. 70

[172] G. D. Byrne and A. C. Hindmarsh, "A Polyalgorithm for the Numerical Solution of Ordinary Differential Equations," *ACM Transactions on Mathematical Software (TOMS)*, vol. 1, no. 1, pp. 71–96, 1975. 70, 71

[173] A. Cuoci, A. Frassoldati, T. Faravelli, and E. Ranzi, "OpenSMOKE++: An Object-Oriented Framework for the Numerical Modeling of Reactive Systems with Detailed Kinetic Mechanisms," *Computer Physics Communications*, vol. 192, pp. 237–264, 2015. 70, 72

[174] A. C. Hindmarsh, "LSODE and LSODI, Two New Initial Value Ordinary Differential Equation Solvers," *ACM SIGNUM Newsletter*, vol. 15, no. 4, pp. 10–11, 1980. 71

[175] A. C. Hindmarsh and R. J. Gelinas, "GEAR: Ordinary Differential Equation System Solver," Tech. Rep. UCID-30001 (Rev.1), Lawrence Livermore Laboratory, University of California, Livermore, CA, United States, 1971. 71

[176] P. N. Brown, G. D. Byrne, and A. C. Hindmarsh, "VODE: A Variable-Coefficient ODE Solver," *SIAM Journal on Scientific and Statistical Computing*, vol. 10, no. 5, pp. 1038–1051, 1989. 71

[177] A. C. Hindmarsh, "ODEPACK, A Systematized Collection of ODE Solvers," in *Scientific Computing* (R. S. Stepleman, M. B. Carver, R. L. Peskin, W. F. Ames, and R. Vichnevetsky, eds.), vol. 1 of *IMACS Transactions on Scientific Computation*, pp. 55–64, Amsterdam: North-Holland, 1983. 71

[178] A. C. Hindmarsh, P. N. Brown, K. E. Grant, S. L. Lee, R. Serban, D. E. Shumaker, and C. S. Woodward, "SUNDIALS: Suite of Nonlinear and Differential/Algebraic Equation Solvers," 2005. 72

[179] D. J. Gardner, D. R. Reynolds, C. S. Woodward, and C. J. Balos, "Enabling New Flexibility in the SUNDIALS Suite of Nonlinear and Differential/Algebraic Equation Solvers," *ACM Transactions on Mathematical Software (TOMS)*, vol. 48, no. 3, pp. 31:1 – 31:24, 2022. 72

[180] Lawrence Livermore National Security and Southern Methodist University, "User Documentation for SUNDIALS." `https://sundials.readthedocs.io/en/latest/`, 2025. Accessed: 2025-05-30. 76, 77

[181] R. A. Yetter, F. L. Dryer, and H. Rabitz, "Flow Reactor Studies of Carbon Monoxide/Hydrogen/Oxygen Kinetics," *Combustion Science and Technology*, vol. 79, no. 1–3, pp. 129–140, 1991. 79, 80, 81

[182] J. Haemisch, D. Suslov, and M. Oschwald, "Experimental and Numerical Investigation of Heat Transfer Processes in Rocket Engine Cooling Channels Operated with Cryogenic Hydrogen and Methane at Supercritical Conditions," *Transactions of the Japan Society for Aeronautical and Space Sciences, Aerospace Technology Japan*, vol. 19, no. 1, pp. 96–105, 2021. 95

[183] M. Börner, C. Manfletti, J. Hardi, D. Suslov, G. Kroupa, and M. Oschwald, "Laser Ignition of a Multi-Injector LOX/Methane Combustor," *CEAS Space Journal*, vol. 10, pp. 273–286, 2018. 95

[184] E. A. Hurlbert, H. Ueno, L. Alexander, M. D. Klem, E. D'Aversa, J.-M. Ruault, C. Manfletti, J.-N. Caruana, H. Asakawa, and R. J. Whitley, "International Space Exploration Coordination Group Assessment of Technology Gaps for LOX/Methane Propulsion Systems for the Global Exploration Roadmap," in *AIAA SPACE 2016 Conference and Exposition*, (Long Beach, California), pp. AIAA 2016–5280, American Institute of Aeronautics and Astronautics, 2016. 95

[185] J. A. Miller, M. J. Pilling, and J. Troe, "Unravelling Combustion Mechanisms Through a Quantitative Understanding of Elementary Reactions," *Proceedings of the Combustion Institute*, vol. 30, no. 1, pp. 43–88, 2005. 95

Appendix A

Chemical Kinetic Mechanisms

A.1 Modified Jachimowski Hydrogen-Oxygen Kinetic Mechanism

Table A.1: Modified Jachimowski Hydrogen-Oxygen Kinetic Mechanism[a] [74].

j	Reaction	A	n	E_a
(1)	$O + H_2 \rightleftharpoons H + OH$	1.0×10^{14}	0	56000
(2)	$H + O_2 \rightleftharpoons OH + O$	1.2×10^{17}	-0.91	16513
(3)	$O + H_2 \rightleftharpoons OH + H$	1.8×10^{10}	1.0	8900
(4)	$OH + H_2 \rightleftharpoons H_2O + H$	2.2×10^{13}	0	5150
(5)	$OH + OH \rightleftharpoons H_2O + O$	6.3×10^{12}	0	1090
(6)[b]	$H + OH + M \rightleftharpoons H_2O + M$	2.2×10^{22}	-2.0	0
(7)[c]	$H + H + M \rightleftharpoons H_2 + M$	6.4×10^{17}	-1.0	0
(8)[d]	$H + O + M \rightleftharpoons OH + M$	6.0×10^{16}	-0.6	0
(9)[e]	$H + O_2 + M \rightleftharpoons HO_2 + M$	2.1×10^{15}	0	-1000
(10)	$HO_2 + H \rightleftharpoons OH + OH$	1.4×10^{14}	0	1080
(11)	$HO_2 + H \rightleftharpoons H_2O + O$	1.0×10^{13}	0	1080
(12)	$HO_2 + O \rightleftharpoons O_2 + OH$	1.5×10^{13}	0	950
(13)	$HO_2 + OH \rightleftharpoons H_2O + O_2$	8.0×10^{12}	0	0
(14)	$HO_2 + HO_2 \rightleftharpoons H_2O_2 + O_2$	2.0×10^{12}	0	0
(15)	$H + H_2O_2 \rightleftharpoons H_2 + HO_2$	1.4×10^{12}	0	3600
(16)	$O + H_2O_2 \rightleftharpoons OH + HO_2$	1.4×10^{13}	0	6400
(17)	$OH + H_2O_2 \rightleftharpoons H_2O + HO_2$	6.1×10^{12}	0	1430
(18)[b]	$H_2O_2 + M \rightleftharpoons OH + OH + M$	1.2×10^{17}	0	45500
(19)	$O + O + M \rightleftharpoons O_2 + M$	6.0×10^{13}	0	-1800

[a] $k_f = AT^{\beta}e^{-\frac{E_a}{\mathcal{R}T}}$; units are seconds, moles, cubic centimetres, calories, and Kelvin.
[b] ε_{H_2O} = 6.0 relative to N_2 (ε_{N_2} = 1).
[c] ε_{H_2} = 2.0 and ε_{H_2O} = 6.0 relative to N_2 (ε_{N_2} = 1).
[d] ε_{H_2O} = 5.0 relative to N_2 (ε_{N_2} = 1).
[e] ε_{H_2} = 2.0 and ε_{H_2O} = 16.0 relative to N_2 (ε_{N_2} = 1).

A.2 Yetter Hydrogen-Oxygen Kinetic Mechanism

Table A.2: Yetter Hydrogen-Oxygen Kinetic Mechanism[a] [49].

j	Reaction	log(A)	n	E_a
H_2-O_2 Chain Reactions				
(1)	$H + O_2 \rightleftharpoons OH + O$	14.28	0.00	16440
(2)	$O + H_2 \rightleftharpoons OH + H$	4.71	2.67	6290
(3)	$OH + H_2 \rightleftharpoons H_2O + H$	8.33	1.51	3430
(4)	$OH + OH \rightleftharpoons H_2O + O$	$k = 5.46 \times 10^{11} \exp(0.00149 \times T)$		
H_2-O_2 Dissociation/Recombination Reactions				
(5)	$H_2 + M \rightleftharpoons H + H + M\,(N_2)$ [b]	19.66	-1.40	104380
	$H_2 + M \rightleftharpoons H + H + M\,(Ar)$ [c]	18.77	-1.10	104380
(6)	$O + O + M \rightleftharpoons O_2 + M\,(N_2)$ [b]	15.79	-0.50	0.00
	$O + O + M \rightleftharpoons O_2 + M\,(Ar)$ [c]	13.28	0.00	-1790
(7)	$H + O + M \rightleftharpoons OH + M$	18.67	-1.00	0.00
(8)	$H + OH + M \rightleftharpoons H_2O + M\,(N_2)$ [b]	22.35	-2.00	0.00
	$H + OH + M \rightleftharpoons H_2O + M\,(Ar)$ [c]	21.92	-2.00	0.00
Formation and Consumption of HO_2				
(9)	$H + O_2 + M \rightleftharpoons HO_2 + M\,(N_2)$ [b]	19.83	-1.42	0.00
	$H + O_2 + M \rightleftharpoons HO_2 + M\,(Ar)$ [c]	15.18	0.00	-1000
(10)	$HO_2 + H \rightleftharpoons H_2 + O_2$	13.82	0.00	2130
(11)	$HO_2 + H \rightleftharpoons OH + OH$	14.23	0.00	870
(12)	$HO_2 + O \rightleftharpoons O_2 + OH$	13.24	0.00	-400
(13)	$HO_2 + OH \rightleftharpoons H_2O + O_2$	16.16	-1.0	0.00
Formation and Consumption of H_2O_2				
(14)	$HO_2 + HO_2 \rightleftharpoons H_2O_2 + O_2$	12.48	0.00	1390
(15)	$H_2O_2 + M \rightleftharpoons OH + OH + M\,(N_2)$ [b]	17.08	0.00	45500
	$H_2O_2 + M \rightleftharpoons OH + OH + M\,(Ar)$ [c]	16.93	0.00	45500
(16)	$H_2O_2 + H \rightleftharpoons H_2O + OH$	13.00	0.00	3590
(17)	$H_2O_2 + H \rightleftharpoons H_2 + HO_2$	13.68	0.00	7950
(18)	$H_2O_2 + O \rightleftharpoons OH + HO_2$	6.98	2.00	3970
(19)	$H_2O_2 + OH \rightleftharpoons H_2O + HO_2$	12.85	0.00	1430

[a] $k = AT^{\beta}e^{-\frac{E_a}{\mathcal{R}T}}$; units are seconds, moles, cubic centimetres, calories, and Kelvin.
[b] ε_{N_2} = 1.0, ε_{H_2O} = 12.0, and ε_{Ar} = 0.75. All other species have efficiencies equal to unity.
[c] The third-body efficiencies for the species listed above are scaled such that ε_{Ar} = 1, all other species not listed have efficiencies equal to unity.

A.3 Li Hydrogen-Oxygen Kinetic Mechanism

Table A.3: Li Hydrogen-Oxygen Kinetic Mechanism[a] [65].

j	Reaction		A	n	E_a
H_2-O_2 Chain Reactions					
(1)	$H + O_2 \rightleftharpoons OH + O$		3.55×10^{15}	-0.41	16600
(2)	$O + H_2 \rightleftharpoons OH + H$		5.08×10^{4}	2.67	6290
(3)	$OH + H_2 \rightleftharpoons H_2O + H$		2.16×10^{8}	1.51	3430
(4)	$H_2O + O \rightleftharpoons OH + OH$		2.97×10^{6}	2.02	13400
H_2-O_2 Dissociation/Recombination Reactions					
	$H_2 + M \rightleftharpoons H + H + M$		4.58×10^{19}	-1.40	104380
(5)[b]	$H_2 + Ar \rightleftharpoons H + H + Ar$		5.84×10^{18}	-1.10	104380
	$H_2 + He \rightleftharpoons H + H + He$		5.84×10^{18}	-1.10	104380
	$O + O + M \rightleftharpoons O_2 + M$		6.16×10^{15}	-0.50	0.00
(6)[b]	$O + O + Ar \rightleftharpoons O_2 + Ar$		1.89×10^{13}	0.00	-1790
	$O + O + He \rightleftharpoons O_2 + He$		1.84×10^{13}	0.00	-1790
(7)[b]	$H + O + M \rightleftharpoons OH + M$		4.71×10^{18}	-1.00	0.00
(8)[c]	$H + OH + M \rightleftharpoons H_2O + M$		3.80×10^{22}	-2.00	0.00
Formation and Consumption of HO_2					
(9)	$H + O_2 + M \rightleftharpoons HO_2 + M$	k_0 [d]	6.37×10^{20}	-1.72	520
	$H + O_2 + M \rightleftharpoons HO_2 + M$	k_0 [e]	9.04×10^{19}	-1.50	490
		k_∞	1.48×10^{12}	0.6	0.00
(10)	$HO_2 + H \rightleftharpoons H_2 + O_2$		1.66×10^{13}	0.00	820
(11)	$HO_2 + H \rightleftharpoons OH + OH$		7.08×10^{13}	0.00	300
(12)	$HO_2 + O \rightleftharpoons O_2 + OH$		3.25×10^{13}	0.00	0.00
(13)	$HO_2 + OH \rightleftharpoons H_2O + O_2$		2.89×10^{13}	0.00	-500
Formation and Consumption of H_2O_2					
(14)[f]	$HO_2 + HO_2 \rightleftharpoons H_2O_2 + O_2$		4.20×10^{14}	0.00	11980
	$HO_2 + HO_2 \rightleftharpoons H_2O_2 + O_2$		1.30×10^{11}	0.00	-1630
(15)[g]	$H_2O_2 + M \rightleftharpoons OH + OH + M$	k_0	1.20×10^{17}	0.00	45500
	$H_2O_2 + M \rightleftharpoons OH + OH + M$	k_∞	2.95×10^{14}	0.00	48400
(16)	$H_2O_2 + H \rightleftharpoons H_2O + OH$		2.41×10^{13}	0.00	3970
(17)	$H_2O_2 + H \rightleftharpoons H_2 + HO_2$		4.82×10^{13}	0.00	7950
(18)	$H_2O_2 + O \rightleftharpoons OH + HO_2$		9.55×10^{6}	2.00	3970
(19)[f]	$H_2O_2 + OH \rightleftharpoons H_2O + HO_2$		1.00×10^{12}	0.00	0.00
	$H_2O_2 + OH \rightleftharpoons H_2O + HO_2$		5.80×10^{14}	0.00	9560

[a] $k = AT^{\beta}e^{-\frac{E_a}{\mathcal{R}T}}$; units are seconds, moles, cubic centimetres, calories, and Kelvin.

[b] ε_{H_2O} = 12.0, ε_{H_2} = 2.5, $\varepsilon_{0.75}$, and ε_{He} = 0.75. When a rate constant is declared specifically for Ar or He collision partner, the efficiency of Ar or He is set to zero when determining M for the same reaction.

[c] ε_{H_2O} = 12.0, ε_{H_2} = 2.5, ε_{Ar} = 0.38, and ε_{He} = 0.38.

[d] F_c = 0.8. ε_{H_2O} = 11.0, ε_{H_2} = 2.0, and ε_{O_2} = 0.78. Use this reaction when the bath gas is N_2.

[e] F_c = 0.5. ε_{H_2O} = 16.0, ε_{H_2} = 3.0, ε_{O_2} = 1.1, and ε_{He} = 1.2. Use this reaction when the main bath gas is Ar or He.

[f] Reactions (14) and (19) are expressed as the sum of the two rate expressions.

[g] F_c = 0.5. ε_{H_2O} = 12.0, ε_{H_2} = 2.5, ε_{Ar} = 0.64, and ε_{He} = 0.64.

A.4 Ó Conaire Hydrogen-Oxygen Kinetic Mechanism

Table A.4: Ó Conaire Hydrogen-Oxygen Kinetic Mechanism[a] [56].

j	Reaction	A	n	E_a
H_2-O_2 Chain Reactions				
(1)	$H + O_2 \rightleftharpoons OH + O$	1.91×10^{14}	0.00	16440
(2)	$O + H_2 \rightleftharpoons OH + H$	5.08×10^{4}	2.67	6292
(3)	$OH + H_2 \rightleftharpoons H_2O + H$	2.16×10^{8}	1.51	3430
(4)	$H_2O + O \rightleftharpoons OH + OH$	2.97×10^{6}	2.02	13400
H_2-O_2 Dissociation/Recombination Reactions				
(5)[b]	$H_2 + M \rightleftharpoons H + H + M$	4.57×10^{19}	-1.40	105100
(6)[c]	$O + O + M \rightleftharpoons O_2 + M$	6.17×10^{15}	-0.50	0.00
(7)[d]	$O + H + M \rightleftharpoons OH + M$	4.72×10^{18}	-1.00	0.00
(8)[e]	$H + OH + M \rightleftharpoons H_2O + M$	4.50×10^{22}	-2.00	0.00
Formation and Consumption of HO_2				
(9)[f, g]	$H + O_2 + M \rightleftharpoons HO_2 + M$	3.48×10^{16}	-0.41	-1120
	$H + O_2 \rightleftharpoons HO_2$	1.48×10^{12}	0.60	0.00
(10)	$HO_2 + H \rightleftharpoons H_2 + O_2$	1.66×10^{13}	0.00	820
(11)	$HO_2 + H \rightleftharpoons OH + OH$	7.08×10^{13}	0.00	300
(12)	$HO_2 + O \rightleftharpoons O_2 + OH$	3.25×10^{13}	0.00	0.00
(13)	$HO_2 + OH \rightleftharpoons H_2O + O$	2.89×10^{13}	0.00	-500
Formation and Consumption of H_2O_2				
(14)[h]	$HO_2 + HO_2 \rightleftharpoons H_2O_2 + O_2$	4.2×10^{14}	0.00	11980
	$HO_2 + HO_2 \rightleftharpoons H_2O_2 + O_2$	1.3×10^{11}	0.00	-1629
(15)[f, i]	$H_2O_2 + M \rightleftharpoons OH + OH + M$	1.27×10^{17}	0.00	45500
	$H_2O_2 \rightleftharpoons OH + OH$	2.95×10^{14}	0.00	48400
(16)	$H_2O_2 + H \rightleftharpoons H_2O + OH$	2.41×10^{13}	0.00	3970
(17)	$H_2O_2 + H \rightleftharpoons H_2 + HO_2$	6.03×10^{13}	0.00	7950
(18)	$H_2O_2 + O \rightleftharpoons OH + HO_2$	9.55×10^{6}	2.00	3970
(19)[h]	$H_2O_2 + OH \rightleftharpoons H_2O + HO_2$	1.0×10^{12}	0.00	0.00
	$H_2O_2 + OH \rightleftharpoons H_2O + HO_2$	5.8×10^{14}	0.00	9560

[a] $k = AT^{\beta}e^{-\frac{E_a}{RT}}$; units are seconds, moles, cubic centimetres, calories, and Kelvin.
[b] ε_{H_2O} = 12.0 and ε_{H_2} = 2.5.
[c] ε_{H_2O} = 12.0, ε_{H_2} = 2.5, ε_{Ar} = 0.83 and ε_{He} = 0.83.
[d] ε_{H_2O} = 12.0, ε_{H_2} = 2.5, ε_{Ar} = 0.75 and ε_{He} = 0.75.
[e] ε_{H_2O} = 12.0, ε_{H_2} = 0.73, ε_{Ar} = 0.38 and ε_{He} = 0.38.
[f] Reaction (9): a = 0.5, $T^{***} = 1.0 \times 10^{-30}$, $T^{*} = 1.0 \times 10^{30}$ and $T^{**} = 1.0 \times 10^{100}$; Reaction (15): a = 0.5, $T^{***} = 1.0 \times 10^{-30}$, $T^{*} = 1.0 \times 10^{30}$.
[g] ε_{H_2} = 1.3, ε_{H_2O} = 14, ε_{Ar} = 0.67 and ε_{He} = 0.67.
[h] Reactions (14) and (19) are expressed as the sum of the two rate expressions.
[i] ε_{H_2O} = 12.0, ε_{H_2} = 2.5, ε_{Ar} = 0.45 and ε_{He} = 0.45.

A.5 Konnov Hydrogen-Oxygen Kinetic Mechanism

Table A.5: Konnov Hydrogen-Oxygen Kinetic Mechanism[a] [58].

j	Reaction	A	n	E_a	F_C
(1a)[b]	$H + H + M \rightleftharpoons H_2 + M$	7.00×10^{17}	-1.0	0	—
(1b)	$H + H + H_2 \rightleftharpoons H_2 + H_2$	1.00×10^{17}	-0.6	0	—
(1c)	$H + H + N_2 \rightleftharpoons H_2 + N_2$	5.40×10^{18}	-1.3	0	—
(1d)	$H + H + H \rightleftharpoons H_2 + H$	3.20×10^{15}	0	0	—
(2)[c]	$O + O + M \rightleftharpoons O_2 + M$	1.00×10^{17}	-1.0	0	—
(3)[d]	$O + H + M \rightleftharpoons OH + M$	6.75×10^{18}	-1.0	0	—
(4a)[e]	$H_2O + M \rightleftharpoons H + OH + M$	6.06×10^{27}	-3.312	120770	—
(4b)	$H_2O + H_2O \rightleftharpoons H + OH + H_2O$	1.00×10^{26}	-2.44	120160	—
(5a)[f]	$H + O_2 + M \rightleftharpoons HO_2 + M$	4.66×10^{12}	0.44	0	—
	Low-pressure limit	5.70×10^{19}	-1.4	0	0.5
(5b)	$H + O_2 + Ar \rightleftharpoons HO_2 + Ar$	4.66×10^{12}	0.44	0	—
	Low-pressure limit	7.43×10^{18}	-1.2	0	0.5
(5c)	$H + O_2 + O_2 \rightleftharpoons HO_2 + O_2$	4.66×10^{12}	0.44	0	—
	Low-pressure limit	5.69×10^{18}	-1.094	0	0.5
(5d)	$H + O_2 + H_2O \rightleftharpoons HO_2 + H_2O$	9.06×10^{12}	0.2	0	—
	Low-pressure limit	3.67×10^{19}	-1.0	0	0.8
(6a)[g]	$OH + OH + M \rightleftharpoons H_2O_2 + M$	1.00×10^{14}	-0.37	0	—
	Low-pressure limit	2.38×10^{19}	-0.8	0	0.5
(6b)	$OH + OH + H_2O \rightleftharpoons H_2O_2 + H_2O$	1.00×10^{14}	-0.37	0	—
	Low-pressure limit	1.45×10^{18}	0	0	0.5
(7)	$O + H_2 \rightleftharpoons OH + H$	5.06×10^{04}	2.67	6290	—
(8)	$H + O_2 \rightleftharpoons OH + O$	2.06×10^{14}	-0.097	15022	—
(9)	$H_2 + OH \rightleftharpoons H_2O + H$	2.14^{08}	1.52	3450	—
(10)	$OH + OH \rightleftharpoons H_2O + O$	3.34×10^{04}	2.42	-1930	—
(11)	$HO_2 + O \rightleftharpoons OH + O_2$	1.63×10^{13}	0	-445	—
(12)	$H + HO_2 \rightleftharpoons OH + OH$	1.90×10^{14}	0	875	—
(13)	$H + HO_2 \rightleftharpoons H_2O + O$	1.45×10^{12}	0	0	—
(14)	$H + HO_2 \rightleftharpoons H_2 + O_2$	1.05×10^{14}	0	2047	—
(15)	$H_2 + O_2 \rightleftharpoons OH + OH$	2.04×10^{12}	0.44	69155	—
(16)[g]	$HO_2 + OH \rightleftharpoons H_2O + O_2$	2.89×10^{13}	0	-500	—
		9.27×10^{15}	0	17500	—
(17a)[g]	$HO_2 + HO_2 \rightleftharpoons H_2O_2 + O_2$	1.03×10^{14}	0	11040	—
		1.94×10^{11}	0	1409	—
(17b)	$HO_2 + HO_2 + M \rightleftharpoons H_2O_2 + O_2 + M$	6.84×10^{14}	0	-1950	—
(18)	$H_2O_2 + H \rightleftharpoons HO_2 + H_2$	1.70×10^{12}	0	3755	—
(19)	$H_2O_2 + H \rightleftharpoons H_2O + OH$	1.00×10^{13}	0	3575	—
(20)	$H_2O_2 + O \rightleftharpoons HO_2 + OH$	9.55×10^{6}	2	3970	—
(21)[h]	$H_2O_2 + OH \rightleftharpoons HO_2 + H_2O$	2.00×10^{12}	0	427	—
		1.70×10^{18}	0	29400	—

[a] $k = AT^{\beta}e^{-\frac{E_a}{\mathcal{R}T}}$; units are seconds, moles, cubic centimetres, and Kelvin.
[b] $\varepsilon_{H_2O} = 14.3$.
[c] $\varepsilon_O = 28.8$, $\varepsilon_{O_2} = 8$, $\varepsilon_{NO} = 2$, $\varepsilon_N = 2$, $\varepsilon_{N_2} = 2$ and $\varepsilon_{H_2O} = 5$.
[d] $\varepsilon_{H_2O} = 5$.
[e] $\varepsilon_{H_2} = 3$, $\varepsilon_{N_2} = 2$ and $\varepsilon_{O_2} = 1.5$.
[f] $\varepsilon_{H_2} = 1.5$ and $\varepsilon_{He} = 0.57$.
[g] The rate constant is the sum of two expressions.

A.6 Hong Hydrogen-Oxygen Kinetic Mechanism

Table A.6: Hong Hydrogen-Oxygen Kinetic Mechanism[a] [59].

j	Reaction j	A_j	n_j	E_j	F_c
(1)	$H + O_2 \rightleftharpoons OH + O$	1.04×10^{14}	0.00	15286	—
(2)[b]	$H + O_2 + Ar \rightleftharpoons HO_2 + Ar$	5.59×10^{13}	0.20	0.00	0.7
	Low-pressure limit	6.81×10^{18}	-1.2	0	0.7
	$H + O_2 + H_2O \rightleftharpoons HO_2 + H_2O$	5.59×10^{13}	0.2	0.00	0.8
	Low-pressure limit	3.70×10^{19}	-1.0	0.00	0.8
	$H + O_2 + O_2 \rightleftharpoons HO_2 + O_2$	5.59×10^{13}	0.20	0.00	0.7
	Low-pressure limit	5.69×10^{18}	-1.1	0.00	0.7
	$H + O_2 + M \rightleftharpoons HO_2 + M$	5.59×10^{13}	0.20	0.00	0.7
	Low-pressure limit	2.65×10^{19}	1.3	0.00	0.7
(3)[c]	$H_2O_2 + M \rightleftharpoons OH + OH + M$	8.59×10^{14}	0.00	48560	1
	Low-pressure limit	9.55×10^{15}	0.00	42203	1
(4)	$OH + H_2O_2 \rightleftharpoons H_2O + HO_2$	1.74×10^{12}	0.00	318	—
		7.59×10^{13}	0	7269	—
(5)	$OH + HO_2 \rightleftharpoons H_2O + O_2$	2.89×10^{13}	0.00	-500	—
(6)	$HO_2 + HO_2 \rightleftharpoons H_2O_2 + O_2$	1.30×10^{11}	0.00	-1603	—
		4.20×10^{14}	0.00	11980	—
(7)[d]	$H_2O + M \rightleftharpoons H + OH + M$	6.06×10^{27}	-3.31	120770	—
	$H_2O + H_2O \rightleftharpoons H + OH + H_2O$	1.00×10^{26}	-2.44	120160	—
(8)	$OH + OH \rightleftharpoons H_2O + O$	3.57×10^{04}	2.40	-2111	—
(9)	$O + H_2 \rightleftharpoons H + OH$	3.82×10^{12}	0.00	7948	—
		$8.79 \times 10_{14}$	0.00	19170	—
(10)	$H_2 + OH \rightleftharpoons H_2O + H$	2.17×10^{08}	1.52	3457	—
(11)	$H + HO_2 \rightleftharpoons OH + OH$	7.08×10^{13}	0.00	300	—
(12)	$H + HO_2 \rightleftharpoons H_2O + O$	1.45×10^{12}	0.00	0.00	—
(13)	$H + HO_2 \rightleftharpoons H_2 + O_2$	3.66×10^{06}	2.087	-1450	—
(14)	$O + HO_2 \rightleftharpoons OH + O_2$	1.63×10^{13}	0.00	-445	—
(15)	$H_2O_2 + H \rightleftharpoons HO_2 + H_2$	1.21×10^{07}	2.00	5200	—
(16)	$H_2O_2 + H \rightleftharpoons H_2O + OH$	1.02×10^{13}	0.00	3577	—
(17)	$H_2O_2 + O \rightleftharpoons OH + HO_2$	8.43×10^{11}	0.00	3970	—
(18)[e]	$H_2 + M \rightleftharpoons H + H + M$	5.84×10^{18}	-1.1	104380	—
	$H_2 + H_2 \rightleftharpoons H + H + H_2$	9.03×10^{14}	0.00	96070	—
	$H_2 + N_2 \rightleftharpoons H + H + N_2$	4.58×10^{19}	-1.4	104380	—
	$H_2 + O_2 \rightleftharpoons H + H + O_2$	4.58×10^{19}	-1.4	104380	—
(19)[f]	$O + O + M \rightleftharpoons O_2 + M$	6.16×10^{15}	-0.50	0.00	—
	$O + O + Ar \rightleftharpoons O_2 + Ar$	1.89×10^{13}	0.00	-1788	—
(20)[g]	$O + H + M \rightleftharpoons OH + M$	4.71×10^{18}	-1.00	0.00	—

[a] $k = AT^{\beta}e^{-\frac{E_a}{\mathcal{R}T}}$; units are seconds, moles, cubic centimetres, and Kelvin.
[b] ε_{N_2} = 1, ε_{H_2} = 1.5, ε_{Ar} = 0.0, ε_{H_2O} = 0.0 and ε_{O_2} = 0.0.
[c] ε_{Ar} = 1, ε_{N_2} = 1.5 and ε_{H_2O} = 9.0
[d] ε_{Ar} = 1.0, ε_{H_2O} = 0.0, ε_{H_2} = 3.0, ε_{N_2} = 2.0 and ε_{O_2} = 1.5.
[e] ε_{Ar} = 1.0, ε_{H_2O} = 14.4, ε_{H_2} = 0.0, ε_{N_2} = 0.0 and ε_{O_2} = 0.0.
[f] ε_{N_2} = 1.0, ε_{H_2} = 2.5, ε_{H_2O} = 12 and ε_{Ar} = 0.0.
[g] ε_{N_2} = 1.0, ε_{H_2} = 2.5, ε_{H_2O} = 12.0 and ε_{Ar} = 0.75.

A.7 Shimizu Hydrogen-Oxygen Kinetic Mechanism

Table A.7: Shimizu Hydrogen-Oxygen Kinetic Mechanism[a] [60].

j	Reaction	A	n	E_a	F_C
(1)	$OH + H_2 \rightleftharpoons H_2O + H$	2.160×10^8	1.51	3440	—
(2)	$H + O_2 \rightleftharpoons OH + O$	1.910×10^{14}	0.00	16440	—
(3)	$O + H_2 \rightleftharpoons OH + H$	5.080×10^4	2.67	6292	—
(4)	$OH + HO_2 \rightleftharpoons H_2O + O_2$	2.890×10^{13}	0.00	-500	—
(5)	$H + HO_2 \rightleftharpoons H_2 + O_2$	3.660×10^6	2.09	-1450	—
(6)	$H + HO_2 \rightleftharpoons OH + OH$	7.080×10^{13}	0.00	300	—
(7)	$H + HO_2 \rightleftharpoons H_2O + O_2$	1.340×10^{13}	0.00	1340	—
(8)	$O + HO_2 \rightleftharpoons O_2 + OH$	3.250×10^{13}	0.00	0.0	—
(9-A)[b]	$HO_2 + HO_2 \rightleftharpoons H_2O_2 + O_2$	4.200×10^{14}	0.00	12000	—
(9-B)[b]	$HO_2 + HO_2 \rightleftharpoons H_2O_2 + O_2$	1.320×10^{11}	0.00	-1192	0.5
(9-B)[b]	$HO_2 + HO_2 + M \rightleftharpoons H_2O_2 + O_2$	6.890×10^{14}	0.00	-1947	0.5
(10)	$OH + OH \rightleftharpoons O + H_2O$	4.330×10^3	2.7	-2485	—
(11)	$H_2O_2 + H \rightleftharpoons H_2O + OH$	8.190×10^8	1.55	3455	—
(12)[b]	$H_2O_2 + H \rightleftharpoons HO_2 + H_2$	8.067×10^{19}	-1.574	16838	—
	$H_2O_2 + H \rightleftharpoons HO_2 + H_2$	1.042×10^{13}	0.00	6569	—
(13)[b]	$H_2O_2 + OH \rightleftharpoons H_2O + HO_2$	1.7000×10^{18}	0.00	29407	—
	$H_2O_2 + OH \rightleftharpoons H_2O + HO_2$	2.000×10^{12}	0.00	427	—
(14)	$H_2O_2 + O \rightleftharpoons HO_2 + OH$	6.620×10^{11}	0.00	3974	—
(15)	$H + O_2 \rightleftharpoons HO_2$	1.933×10^{12}	0.56	0.00	0.62
	$H + O_2 + M \rightleftharpoons HO_2 + M$	4.570×10^{18}	-1.12	0.00	0.62
	$H + O_2 \rightleftharpoons HO_2$	1.933×10^{12}	0.56	0.00	0.5
	$H + O_2 + H_2 \rightleftharpoons HO_2 + H_2$	3.520×10^{18}	-0.896	0.00	0.5
	$H + O_2 \rightleftharpoons HO_2$	1.933×10^{12}	0.56	0.00	0.67
	$H + O_2 + N_2 \rightleftharpoons HO_2 + N_2$	1.750×10^{19}	-1.232	0.00	0.67
	$H + O_2 \rightleftharpoons HO_2$	1.933×10^{12}	0.56	0.00	0.5
	$H + O_2 + O_2 \rightleftharpoons HO_2 + O_2$	1.410×10^{18}	-0.849	0.00	0.5
	$H + O_2 \rightleftharpoons HO_2$	1.933×10^{12}	0.56	0.00	0.81
	$H + O_2 + H_2O \rightleftharpoons HO_2 + H_2O$	3.630×10^{18}	-1.00	0.00	0.81
	$H + O_2 \rightleftharpoons HO_2$	1.933×10^{12}	0.56	0.00	0.59
	$H + O_2 + He \rightleftharpoons HO_2 + He$	3.630×10^{19}	-1.00	0.00	0.59
(16)[c]	$H + H + M \rightleftharpoons H_2 + M$	7.000×10^{17}	-1.0	0.00	—
	$H + H + H_2 \rightleftharpoons H_2 + H_2$	1.000×10^{17}	-0.6	0.00	—
	$H + H + N_2 \rightleftharpoons H_2 + N_2$	5.400×10^{18}	-1.3	0.00	—
	$H + H + H \rightleftharpoons H_2 + H$	3.200×10^{15}	0.00	0.00	—
(17)[d]	$H + OH + M \rightleftharpoons H_2O + M$	3.500×10^{22}	-2.0	0.00	—
(18)[e]	$H + O + M \rightleftharpoons OH + M$	6.750×10^{18}	-1.0	0.00	—
(19)[f]	$O + O + M \rightleftharpoons O_2 + M$	6.160×10^{15}	-0.5	0.00	—
	$O + O + Ar \rightleftharpoons O_2 + Ar$	1.890×10^{13}	0.00	-1790	—
	$O + O + He \rightleftharpoons O_2 + He$	1.890×10^{13}	0.00	-1790	—
(20)	$H_2O_2 \rightleftharpoons OH + OH$	3.000×10^{14}	0.00	48482	0.44
	$H_2O_2 + M \rightleftharpoons OH + OH + M$	2.290×10^{16}	0.00	43634	—
(21)	$O + OH + M \rightleftharpoons HO_2 + M$	3.820×10^{15}	-0.216	0.00	—

[a] $k = AT^{\beta}e^{-\frac{E_a}{\mathcal{R}T}}$; units are seconds, moles, cubic centimetres, calories, and Kelvin.
[b] Expressed as the sum of the two rate expressions.
[c] ε_{O_2} = 2.2 and ε_{H_2O} = 14.4.
[d] ε_{H_2O} = 12.0, ε_{Ar} = 0.38 and ε_{He} = 0.38.
[e] ε_{H_2O} = 5.0.
[f] ε_{H_2O} = 12.0 and ε_{H_2} = 2.5.
[g] ε_{H_2O} = 15.0, ε_{H_2} = 3.0 and ε_{N_2} = 3.0 .

A.8 Burke Hydrogen-Oxygen Kinetic Mechanism

Table A.8: Burke Hydrogen-Oxygen Kinetic Mechanism[a] [51].

j	Reaction j		A_j	n_j	E_j
(1)	$H + O_2 \rightleftharpoons O + OH$		1.04×10^{14}	0.00	15310
(2)	$O + H_2 \rightleftharpoons H + OH$		3.82×10^{12}	0.00	7948
			8.79×10^{14}	0.00	19170
(3)	$H_2 + OH \rightleftharpoons H_2O + H$		2.16×10^{08}	1.51	3430
(4)	$OH + OH \rightleftharpoons O + H_2$		3.34×10^{04}	2.42	-1930
(5)[b]	$H_2 + M \rightleftharpoons H + H + M$		4.58×10^{19}	-1.40	104000
	$H_2 + Ar \rightleftharpoons H + H + Ar$		5.84×10^{18}	-1.10	104000
	$H_2 + He \rightleftharpoons H + H + He$		5.84×10^{18}	-1.10	104000
(6)[b]	$O + O + M \rightleftharpoons O_2 + M$		6.16×10^{15}	-0.50	0.00
	$O + O + Ar \rightleftharpoons O_2 + Ar$		1.89×10^{13}	0.00	-1790
	$O + O + He \rightleftharpoons O_2 + He$		1.89×10^{13}	0.00	-1790
(7)[c]	$O + H + M \rightleftharpoons OH + M$		4.71×10^{18}	-1.00	0.00
(8)[d]	$H_2O + M \rightleftharpoons H + OH + M$		6.06×10^{27}	-3.32	120800
	$H_2O + H_2O \rightleftharpoons H + OH + H_2O$		1.01×10^{26}	-2.44	120200
(9-A)[e]	$H + O_2 + M \rightleftharpoons HO_2 + M$	k_∞	4.65×10^{12}	0.44	0.00
		k_0	6.37×10^{20}	-1.72	525
(9-B)[f]	$H + O_2 + M \rightleftharpoons HO_2 + M$	k_∞	4.65×10^{12}	0.44	0.00
		k_0	9.04×10^{19}	-1.50	492
(10)	$HO_2 + H \rightleftharpoons H_2 + O_2$		2.75×10^{06}	2.09	-1451
(11)	$HO_2 + H \rightleftharpoons OH + OH$		7.08×10^{13}	0.00	295
(12)	$HO_2 + O \rightleftharpoons O_2 + OH$		2.85×10^{10}	1.00	-723.9
(13)	$HO_2 + OH \rightleftharpoons H_2O + O_2$		2.89×10^{13}	0.00	-497
(14)	$HO_2 + HO_2 \rightleftharpoons H_2O_2 + O_2$		4.20×10^{14}	0.00	12000
			1.30×10^{11}	0.00	-1630
(15)[g]	$H_2O_2 + M \rightleftharpoons OH + OH + M$	k_∞	2.00×10^{12}	0.90	48750
		k_0	2.49×10^{24}	-2.30	48750
(16)	$H_2O_2 + H \rightleftharpoons H_2O + OH$		2.41×10^{13}	0.00	3970
(17)	$H_2O_2 + H \rightleftharpoons H_2O + H_2$		4.82×10^{13}	0.00	7950
(18)	$H_2O_2 + O \rightleftharpoons OH + HO_2$		9.55×10^{06}	2.00	3970
(19)	$H_2O_2 + OH \rightleftharpoons HO_2 + H_2O$		1.74×10^{12}	0.00	318
			7.59×10^{13}	0.00	7270

[a] $k = AT^{\beta}e^{-\frac{E_a}{\mathcal{R}T}}$; units are seconds, moles, cubic centimetres, and Kelvin.

[b] ε_{H_2} = 2.5, ε_{H_2O} = 12.0, ε_{Ar} = 0.0 and ε_{He} = 0.0.

[c] ε_{H_2} = 2.5, ε_{H_2O} = 12.0, ε_{Ar} = 0.75 and ε_{He} = 0.75.

[d] ε_{H_2} = 3.0, ε_{H_2O} = 0.0, ε_{O_2} = 1.5, ε_{N_2} = 2.0 and ε_{He} = 0.75.

[e] Recommended for use with mixtures where N_2 is the primary bath gas. ε_{H_2} = 2.0, ε_{H_2O} = 14.0, ε_{O_2} = 0.78, ε_{Ar} = 0.67 and ε_{He} = 0.8. F_c = 0.5.

[f] Recommended for use with mixtures where Ar or He is the primary bath gas. ε_{H_2} = 3.0, ε_{H_2O} = 21.0, ε_{O_2} = 1.1, ε_{He} = 1.2 and ε_{N_2} = 1.5. F_c = 0.5.

[g] ε_{H_2} = 3.7, ε_{H_2O} = 7.5, $\varepsilon_{H_2O_2}$ = 7.7, ε_{O_2} = 1.2, ε_{N_2} = 1.5 and ε_{He} = 0.65. F_c = 0.42.

A.9 Kéromnès Hydrogen-Oxygen Kinetic Mechanism

Table A.9: Kéromnès Hydrogen-Oxygen Kinetic Mechanism[a] [55].

j	Reaction	A	n	E_a	F_C
(1)	$H + O_2 \rightleftharpoons O + OH$	1.040×10^{14}	0.00	15290	—
(2)	$O + H_2 \rightleftharpoons H + OH$	5.080×10^{04}	2.67	6292	—
(3)	$OH + H_2 \rightleftharpoons H + H_2O$	4.380×10^{13}	0.00	6990	—
(4)	$O + H_2O \rightleftharpoons OH + OH$	2.970×10^{6}	2.02	13400	—
(5)[b]	$H_2 + M \rightleftharpoons H + H + M$	4.577×10^{19}	-1.40	104400	—
(6)[c]	$O + O + M \rightleftharpoons O_2 + M$	6.165×10^{15}	-0.50	0.00	—
(7)[d]	$O + H + M \rightleftharpoons OH + M$	4.714×10^{18}	-1.00	0.00	—
(8)[e]	$H + OH + M \rightleftharpoons H_2O + M$	3.500×10^{22}	-2.00	0.00	—
(9)[f]	$H + O_2 + M \rightleftharpoons HO_2 + M$	4.650×10^{12}	0.44	0.00	0.67
	Low-pressure limit	1.737×10^{19}	-1.23	0.00	0.67
	$H + O_2 + Ar \rightleftharpoons HO_2 + Ar$	4.650×10^{12}	0.44	0.00	0.70
	Low-pressure limit	6.810×10^{18}	-1.20	0.00	0.70
	$H + O_2 + He \rightleftharpoons HO_2 + He$	4.650×10^{12}	0.44	0.00	0.59
	Low-pressure limit	9.190×10^{18}	-1.20	0.00	0.59
(10)	$H_2 + O_2 \rightleftharpoons H + HO_2$	$5.176 \times 10_{5}$	2.43	53500	—
(11)	$HO_2 + H \rightleftharpoons OH + OH$	7.079×10^{13}	0.00	295	—
(12)	$HO_2 + O \rightleftharpoons OH + O_2$	3.250×10^{13}	0.00	0.00	—
(13)	$HO_2 + OH \rightleftharpoons H_2O + O_2$	2.456×10^{13}	0.00	-497	—
(14)	$HO_2 + HO_2 \rightleftharpoons H_2O_2 + O_2$	1.300×10^{11}	0.00	-1630	—
		3.658×10^{14}	0.00	12000	—
(15)[g]	$H_2O_2 + M \rightleftharpoons OH + OH + M$	2.000×10^{12}	0.90	48750	0.43
	Low-pressure limit	2.490×10^{24}	-2.30	48750	0.43
	$H_2O_2 + H_2O \rightleftharpoons OH + OH + H_2O$	2.000×10^{12}	0.90	48750	0.51
	Low-pressure limit	1.865×10^{25}	-2.30	48750	0.51
(16)	$H_2O_2 + H \rightleftharpoons H_2O + OH$	2.410×10^{13}	0.00	3970	—
(17)	$H_2O_2 + H \rightleftharpoons H_2 + HO_2$	2.150×10^{10}	1.00	6000	—
(18)	$H_2O_2 + O \rightleftharpoons OH + HO_2$	9.550×10^{6}	2.00	3970	—
(19)	$H_2O_2 + OH \rightleftharpoons H_2O + HO_2$	1.740×10^{12}	0.00	318	—
		7.590×10^{13}	0.00	7269	—
OH* Chemiluminescence reaction mechanism					
(20)[h]	$H + O + M \rightleftharpoons OH^* + M$	1.500×10^{13}	0.00	5975	—
(21)	$OH^* + O_2 \rightleftharpoons OH + O_2$	2.100×10^{12}	0.50	-482	—
(22)	$OH^* + H_2 \rightleftharpoons OH + H_2$	2.950×10^{12}	0.50	-444	—
(21)	$OH^* + N_2 \rightleftharpoons OH + N_2$	1.080×10^{11}	0.50	-1242	—
(22)	$OH^* + Ar \rightleftharpoons OH + O_2$	1.690×10^{12}	0.00	4135	—
(23)	$OH^* + H_2O \rightleftharpoons OH + H_2O$	5.930×10^{12}	0.50	-861	—
(24)	$OH^* + OH \rightleftharpoons OH + OH$	6.010×10^{12}	0.50	-764	—
(25)	$OH^* \longrightarrow OH + hv$	1.450×10^{6}	0.00	0.0	—

[a] $k = AT^{\beta}e^{-\frac{E_a}{\mathcal{R}T}}$; units are seconds, moles, cubic centimetres, calories, and Kelvin.
[b] ε_{H_2} = 2.5, ε_{H_2O} = 12, ε_{He} = 0.83.
[c] ε_{H_2} = 2.5, ε_{H_2O} = 12, ε_{Ar} = 0.83 and ε_{He} = 0.83.
[d] ε_{H_2} = 2.5, ε_{H_2O} = 12, ε_{Ar} = 0.75 and ε_{He} = 0.75.
[e] ε_{H_2} = 0.73, ε_{H_2O} = 3.65, ε_{Ar} = 0.38 and ε_{He} = 0.38.
[f] ε_{H_2} = 1.3, ε_{H_2O} = 10, ε_{Ar} = 0.0 and ε_{He} = 0.0.
[g] ε_{H_2} = 3.7, ε_{N_2} = 1.5, ε_{O_2} = 1.2, ε_{He} = 0.65, $\varepsilon_{H_2O_2}$ = 7.7 and ε_{H_2O} = 0.0.
[h] ε_{N_2} = 0.4, ε_{O_2} = 0.4, ε_{H_2O} = 6.5 and ε_{Ar} = 0.35.

A.10 Varga Hydrogen-Oxygen Kinetic Mechanism

Table A.10: Varga Hydrogen-Oxygen Kinetic Mechanism[a] [85].

j	Reaction	A	n	E_a	F_C
(1)	$H + O_2 \rightleftharpoons O + OH$	1.372×10^{13}	0.2434	60404.571	—
(2)	$O + H_2 \rightleftharpoons H + OH$	2.717×10^{04}	2.75	26672.796	—
(3)	$OH + H_2 \rightleftharpoons H + H_2O$	2.186×10^{7}	1.803	13402.914	—
(8)[b]	$H + OH + M \rightleftharpoons H_2O + M$	1.320×10^{24}	-2.60	-472.594	—
(9)[b, c]	$H + O_2 + M \rightleftharpoons HO_2 + M$	1.879×10^{19}	-1.239	0.00	0.67
	Low-pressure limit	1.737×10^{19}	-1.23	0.00	0.67
	$H + O_2 + Ar \rightleftharpoons HO_2 + Ar$	4.650×10^{12}	0.44	0.00	0.70
	Low-pressure limit	6.810×10^{18}	-1.20	0.00	0.70
	$H + O_2 + He \rightleftharpoons HO_2 + He$	4.650×10^{12}	0.44	0.00	0.59
	Low-pressure limit	9.190×10^{18}	-1.20	0.00	0.59
(10)	$H + HO_2 \rightleftharpoons H_2 + O_2$	$1.144 \times 10_{10}$	1.083	2317.241	—
(11)	$HO_2 + H \rightleftharpoons OH + OH$	6.401×10^{13}	0.00	991.915	—
(13)	$HO_2 + OH \rightleftharpoons H_2O + O_2$	2.913×10^{08}	1.441	-8979.620	—
(14)	$H_2O_2 + O_2 \rightleftharpoons HO_2 + HO_2$	1.238×10^{14}	0.00	43675.872	—
		3.658×10^{14}	0.00	12000	—
(15)[b]	$H_2O_2 + M \rightleftharpoons OH + OH + M$	1.957×10^{15}	-0.2033	-18083.956	0.43
(17)	$H_2O_2 + H \rightleftharpoons H_2 + HO_2$	1.372×10^{13}	-1.249	31079.461	—

[a] $k = AT^{\beta}e^{-\frac{E_a}{RT}}$; units are seconds, moles, cubic centimetres, and Kelvin.

[b] The optimised values correspond to the low-pressure limit.

[c] ε_{H_2} = 1.48 ± 1.0, ε_{H_2O} = 12.03 ± 0.53, and ε_{Ar} = 0.540 ± 0.011

A.11 Zettervall Hydrogen-Oxygen Kinetic Mechanism

Table A.11: Zettervall Hydrogen-Oxygen Kinetic Mechanism[a] [50].

j	Reaction	A	n	E_a
(1)	$H_2 + O_2 \longrightarrow H + HO_2$	7.40×10^{05}	2.43	53500
(2)[b]	$H_2 + M \longrightarrow H + H + M$	4.57×10^{19}	-1.4	105100
(3)	$HO_2 + H_2 \longrightarrow H_2O_2 + H$	3.00×10^{06}	2	21000
(4)	$H + O_2 \longrightarrow OH + O$	2.45×10^{14}	0	16800
(5)	$OH + O \longrightarrow H + O_2$	1.20×10^{13}	0	690
(6)	$O + H_2 \longrightarrow OH + H$	1.80×10^{10}	1	8826
(7)	$OH + H \longrightarrow O + H_2$	8.00×10^{09}	1	6760
(8)	$H_2 + OH \longrightarrow H_2O + H$	1.17×10^{09}	1.3	3626
(9)	$H_2O + H \longrightarrow H_2 + OH$	$5.09 \times 10_{09}$	1.3	18588
(10)	$OH + OH \longrightarrow O + H_2O$	6.00×10^{08}	1.3	0
(11)	$O + H_2O \longrightarrow OH + OH$	5.90×10^{09}	1.3	17029
(12)[c]	$H + O_2 + M \longrightarrow HO_2 + M$	1.80×10^{18}	-0.8	0
(13)	$H + HO_2 \longrightarrow OH + OH$	1.50×10^{14}	0	1004
(14)	$H + HO_2 \longrightarrow H_2 + O_2$	$2.50 \times 10_{13}$	0	700
(15)	$OH + HO_2 \longrightarrow H_2O + O_2$	2.00×10^{13}	0	1000
(16)	$HO_2 + HO_2 \longrightarrow H_2O_2 + O_2$	8.00×10^{13}	0	0
(17)	$H_2O_2 + M \longrightarrow OH + OH + M$	1.30×10^{17}	0	34500
(18)	$OH + OH + M \longrightarrow H_2O_2$	9.86×10^{17}	0	-5070
(19)	$H_2O_2 + OH \longrightarrow H_2O + HO_2$	1.00×10^{13}	0	1800
(20)	$H_2O + HO_2 \longrightarrow H_2O_2 + OH$	2.86×10^{13}	0	32790
(21)	$OH + H + M \longrightarrow H_2O + M$	2.20×10^{22}	-2	0
(22)	$H + H + M \longrightarrow H_2 + M$	$1.80 \times 10_{18}$	-1	0

[a] $k = AT^{\beta}e^{-\frac{E_a}{\mathcal{R}T}}$; units are seconds, moles, cubic centimetres, and Kelvin.
[b] ε_{H_2} = 2.5, ε_{H_2O} = 12.0, ε_{N_2} = 1.0 and ε_{O_2} = 1.0.
[c] ε_{H_2} = 1.0, ε_{H_2O} = 6.5, ε_{N_2} = 0.4 and ε_{O_2} = 0.4.